High Power Photodiodes and Applications in Microwave Photonic

A Dissertation

Presented to

the faculty of the School of Engineering and Applied Science

University of Virginia

in partial fulfillment

of the requirements for the degree

Doctor of Philosophy

by

Xiaojun Xie

December

2015

APPROVAL SHEET

The dissertation

is submitted in partial fulfillment of the requirements

for the degree of

Doctor of Philosophy

AUTHOR

The dissertation has been read and approved by the examining committee:

Dr. Joe C. Campbell

Advisor

Dr. Andrea Beling

Dr. Robert M. Weikle II

Dr. Mool C. Gupta

Dr. Archie L. Holmes Jr.

Dr. Patrick E. Hopkins

Accepted for the School of Engineering and Applied Science:

Craig H. Benson, Dean, School of Engineering and Applied Science

December

2015

Dedicated

To

my wife & my parents

Acknowledgements

I would like to thank my advisor, Dr. Joe C. Campbell with my deepest gratitude, for giving me the opportunity to join his group and providing me with his invaluable guidance. I could not have imagined completing my Ph.D so quickly without Dr. Campbell's wisdom. It is my fantastic fortune that Dr. Campbell is an experienced advisor who gives me the freedom to explore what I feel excited about and provides his insightful advice at the same time. I have learned a great deal from his life stories filled with wealthy life philosophies which will guide me in my future research and life.

I would like to thank my co-advisor, Dr. Andreas Beling. Ever since I joined the group in summer 2013, I have been impressed by his broad knowledge and insightful comments on my work. His guidance on both experiments and fabrication enabled my research to proceed smoothly.

I also would like to thank my committee of Professor Robert M. Weikle, Professor Mool C. Gupta, Professor Archie L. Holmes and Professor Patrick E. Hopkins. Since my proposal they have been very helpful in guiding my dissertation and offering constructive feedback.

During my Ph.D research, I found inter-disciplinary collaboration to be of great importance. Here I want to give my great thanks to Dr. Erik Norberg, Dr. Matt Jaco-Mitos, Dr. Anand Ramaswamy from Aurrion Inc. for their great help with wafer bonding. I also want to thank Dr. Arthur W. Lichtenberger, Dr. Jianzhong Zhang, Jie Wang and Dr. Michael Cyberey for their beneficial comments on my fabrication process flow.

I am so thankful to Qiugui Zhou for familiarizing me with the lab and his support of my research work. I learned a lot of basic but important knowledge of photodiodes from Qiugui. I also want to thank Yaojia Chen and Kejia Li for training me to do fabrication. Many thanks go to Yang Fu for his helpful comments. I would like to acknowledge our group members Jizhao Zang, Ye Wang, Yang Shen, Min Ren, Zhanyu Yang, and Qinglong Li as well for their valuable discussions.

Further, I would like to thank Joan M. Sipe, Brenda E. Crider, Dan R. Fetko, Beth Eastwood-Beatty, Yadira Weaver and David Durocher for their administrative help. Brenda and Joan have been incredibly helpful in keeping everything in order and making our group happy and warm. I would like to thank our cleanroom stuff including Joseph Beatrice, M. Alex Lobo, Michael Stogoski and Tim Pernell for maintaining all of the instruments and providing a great working environment.

Here I want to give my great gratitude to my master's thesis advisor, Dr. Yitang Dai and Dr. Kun Xu, for their patient guidance and strong support of my master's degree research. I learned basic experimental skills and a wide range of research topics from them. I would like to thank Hao Huang and Mingzhi Lu for providing me with important information during my application.

Last but not least, I would like to thank my father Rongde Xie and my mother Yuchun Wu, who raised me to value hard work and provided me with the best education possible. Thank my aunt Yulan Li, my uncle Jiguang Chen, my elder brother Xiaolin Xie for supporting me through these years. I want to express my deepest love to my wife Cong Hao. Without understanding and support from her, I definitely could not have finished my Ph.D research work so soon. She has been my constant companion for the last five years no matter where I am or what I am doing. Whenever I encounter difficulties in both research and life, she encourages me and supports me without waiver. The best blessing and gift to my graduation is that our little angel will come to this world. All of this is for you! I am proud of both of you!

Where there is love, there are always miracles.

Xiaojun Xie

University of Virginia

December 2015

Abstract

In recent years, analog photonic links have demonstrated the potential to improve the performance of broadband wireless access networks, cable television signal distribution networks, and remote microwave antenna systems owing to its large instantaneous bandwidth, the low attenuation of optical fibers, continuous spectral coverage, enhanced signal processing capabilities, as well as size, weight, and power consumption benefits. High-performance analog photonic links can also be achieved by using optoelectronic components whose characteristics are optimized for these applications, namely, high-power and low-noise lasers, highly linear modulators that operate at high input power with high conversion efficiency, and high-power, high-frequency and high-linearity photodiodes. For those links that employ a high power and low noise laser and a linearized modulator, power handling capability of the photodiodes sets an upper limit on the link performance.

In this dissertation, photodiodes with high power handling capability are demonstrated. One of the primary limitations on photodiode output power is thermal failure. Self-aligned flip-chip bonding to high-thermal-conductivity submounts has been used to improve heat dissipation. In this work, I have extended previous reports that utilized Si or AlN submounts to diamond heat sinks. These photodiodes have achieved record RF output power of 1.8 W at 10 GHz and saturation current of 300 mA. This is 80% higher than the previous “champion” result [1]. These CC-MUTC photodiodes also achieved record power

conversion efficiency of 50.7% to 60% at 6 to 10 GHz with ~ 27.8 dBm RF output power, which compares favorably with previously reported efficiencies of < 40 % for the same frequency range.

I have used these photodiodes to build an analog photonic link with record performance. This link achieved gain of 24.5 dB at 12 GHz, noise figure of 6.9 dB at 12 GHz, and SFDR with >120 dB·$Hz^{2/3}$ in the frequency range 6 -12 GHz. In addition, optical generation of high-power pulsed microwave signals has been demonstrated. The impulse response without RF modulation at -35 V bias voltage, yielded pulses with 33.5 V peak voltage and full width at half maximum (FWHM) of 50 ps. The peak power levels for gated modulation at 1 GHz and 10 GHz were 41.5 dBm (14.2 W) and 40 dBm (10 W), respectively.

Currently most microwave photonic systems that consist of discrete components suffer from large size, poor reliability and high cost. In order to address these limitations, microwave photonics systems integrated on SOI have been proposed and demonstrated [2, 3]. In this dissertation, a high-performance CC-MUTC photodiode has been integrated on SOI waveguides using a heterogeneous wafer-bonding technology. This is a key enabler for silicon-based on-chip microwave photonics systems. By optimizing the epitaxial layer structure, single CC-MUTC waveguide photodiodes with 210 μm^2 area have achieved 48 GHz bandwidth and 10×35 μm^2 photodiodes exhibited 0.95 A/W internal responsivity and output >12 dBm RF power at 40 GHz modulation frequency. A similar approach has been used to fabricate balanced detectors with 0.78 A/W internal responsivity, 14 GHz bandwidth, 17.2 dBm RF output power at 10 GHz, and 15.2 dBm RF output power at 20

GHz. These are the highest RF output power levels reported at for any waveguide photodiode technology including native InP, Ge/Si, and heterogeneous integration.

The power handling capability of the CC-MUTC waveguide photodiodes on SOI is limited by thermal failure. In order to improve thermal dissipation and increase the RF power of these photodiodes, a chemical-vapor-deposited (CVD) diamond with high thermal conductivity is used to replace the silicon dioxide in SOI. The dark current of photodiodes integrated with these SOD (silicon on diamond) waveguides is ~10 nA at -5 V bias and the bandwidth can reach up to 25 GHz bandwidth.

Table of Contents

List of Figures

Chapter 1 Introduction

1.1 Analog optical links

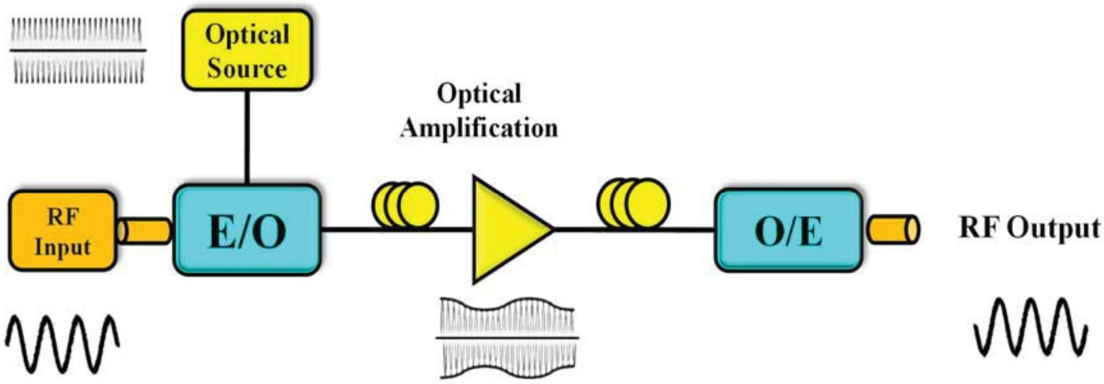

Figure 1.1 Schematic diagram of analog photonic link.

Optical communication has made substantial advances during the 40 years since the invention of optical fibers [4]. The ubiquitous deployment of optical fiber systems is due, in large part, to their ultra-low loss compared to coaxial cables. For example, the transmission loss of a typical commercial coaxial cable is 56 dB/km at 2.4 GHz while a typical optical fiber exhibits loss of < 0.2 dB/km at 1.55 μm wavelength [5]. In addition optical fiber exhibits ultrawide information bandwidth, immunity to electromagnetic interference, and small size and weight [5]. At present, most optical fiber systems, including multi gigabit long haul links [6] and access network [7] employ digital signal modulation. In recent years, analog photonic links have demonstrated the potential to improve the performance of broadband wireless access networks, cable television signal distribution networks, and remote microwave antenna systems [8]. The simplest configuration of an analog photonic link consists of an electrical-to-optical (E/O) transmitter (i.e. direct/external modulation of lasers) and an optical-to-electrical (O/E) receiver (i.e. photodiodes), connected with an optical fiber as illustrated in Figure 1.1. A high frequency RF signal is converted to an optical signal in the transmitter. After the transmission or distribution, the optical signal is converted back to the electrical format in receiver. The primary advantage of transmission in the optical format arises from the ultra-low loss for all RF frequencies in the optical fiber [5].

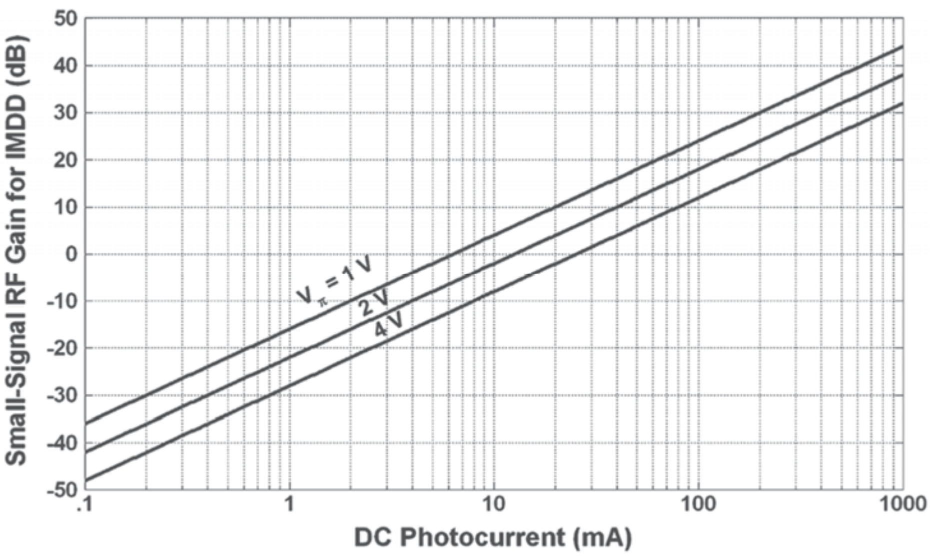

Figure 1.2 Calculated small-signal link gain for an analog link as a function of DC photocurrent for three values of V_π with 50-Ω load resistance.

The performance of an analog photonic link is typically characterized by a set of parameters defined for microwave components. The most important figures of merit are the link gain, the noise figure, and the spur-free dynamic range (SFDR). The link gain is used to describe the power transfer of the link. The noise figure describes the signal-to-noise ratio (SNR) degradation while SFDR characterizes the power range of the RF signal that can be accommodated by the link. For an analog photonic link, link gain is an important figure of merit since the noise figure and dynamic range depend on the link gain. Owing to its low loss, the optical fiber has little effect on the link gain. The link gain is primarily dependent on the characteristics of the laser, modulator and photodiode. In the transmitter, a high power and low noise laser is desired and a modulator with low half-voltage and high power handling capacity are beneficial. For the receiver, the power handing capability of the photodiode is essential to improve the link gain, reduce the noise figure and improve the SFDR. The higher input optical power received by the photodiode the higher will be the RF output power. Therefore the link gain can be improved by increasing the input optical power of photodiodes. The small-signal link gain, without considering the nonlinearity of modulators and photodiodes, is proportional to the square of the DC photocurrent and inversely proportional to the square of the half-wave voltage of the modulator.

The photodiode characteristics have broad impact on the analog link performance. For a fixed half-wave voltage, the link gain increases from -35 dB to 25 dB (60 dB improvement) when the DC photocurrent increases by 1000 times, from 0.1 mA to 100 mA. This is illustrated in Figure 1.2 [9]. High power handling capability of the photodiode is needed to achieve high link gain [9]. High-speed operation of the link is impossible without photodiodes that have correspondingly large bandwidth. Photodiodes with high linearity are also important for minimizing signal distortion and maintaining large SFDR in the link. If the RF output power from the photodiode is large enough, it may be possible to eliminate electronic amplifiers and their corresponding noise from the link. The photodiodes also need to have low distortion in order to avoid introducing additional phase noise during the photo-detection process [10].

1.2 High-power pulsed-RF generation

The advantages of optical fibers for as a transmission medium have led to their use in many military and civilian applications [11]. One of typical military applications is wideband microwave photonic link for shipboard RF antenna remoting. The performance attained by the broadband analog links makes them strong candidates to replace copper cable [12]. Figure 1.3 shows a schematic diagram of a typical photonic antenna remoting system. In the conventional antenna remoting system, the large number of heavy coaxial cables becomes a significant issue for avionic, submarine, and even shipboard applications. However, analog photonic links can significantly reduce the size and weight of the cable plant.

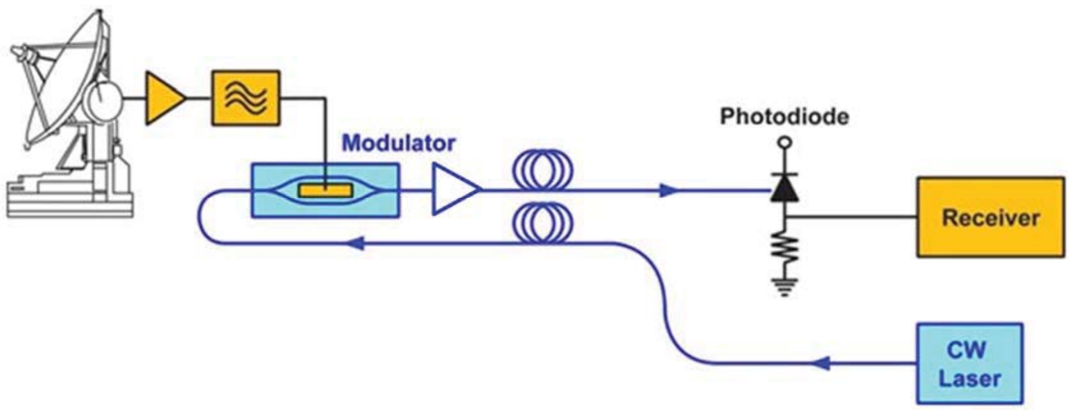

Figure 1.3 Schematic diagram of photonic antenna remote.

In addition, analog photonic links are attractive for the next generation of radar systems with higher carrier frequencies for smaller antennas and broadened bandwidth for increased resolution [13]. Since digital microwave components suffer from poor effective number of bits (ENOB) at high frequency [14], the operation bandwidth of fully digital radar systems reaches to only a few gigahertz. In contrast, photonics technology offers ultra-wide bandwidth and ultra-low loss. A fully photonics-based coherent radar system has been demonstrated [13]. In that work, a single pulsed laser was used to generate high-frequency tunable pulsed radar signals. The performance of that system exceeded state-of-the-art electronics at carrier frequencies above two gigahertz, and the detection of non-cooperating airplanes confirmed the effectiveness and expected precision of the system [13]. In the photonic transceiver module, the pulsed radar signal was generated by mode-locked lasers using intrinsic phase-locking [15]. The receivers were based on photonic analog-to-digital converters (ADC) that were able to process reflected pulse signals with bandwidths of several tens of gigahertz [16].

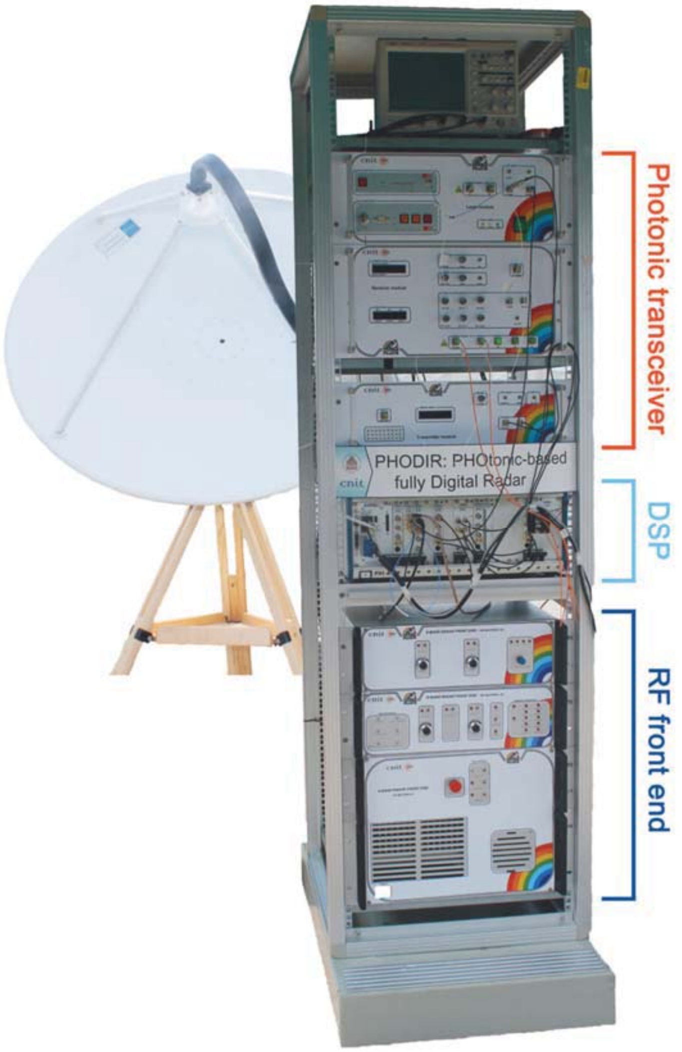

Figure 1.4 Photonics-based radar transceiver. A picture of the field-trial demonstrator. DSP, digital signal processor.

To perform these tasks in military platforms, the analog photonic link needs to be able to generate high-power pulse RF signals, especially for radar and wireless communication. The photodiode is the key component to achieve this since it sets the limitation of available peak power for the whole system. Developing high-power and high-linearity photodiodes enables high peak power for these applications.

1.3 Photonics integration circuit

Microwave photonics (including analog photonic links) offers a possibility to address the some of the challenges that microwave systems have yet to satisfactorily address. Microwave photonics has demonstrated the potential to significantly influence a wide range of applications including analog photonic links [9], distributed antenna arrays [17], and photonic microwave generation [10]. However, at this point, there are still several factors that limit the wide deployment of microwave photonics beyond the laboratory demonstrations. The first is dynamic range [18]. Even though microwave photonic systems exhibit excellent functionalities such as true time delay and pulse shaping over wide bandwidth, the gain, noise figure and dynamic range of these systems

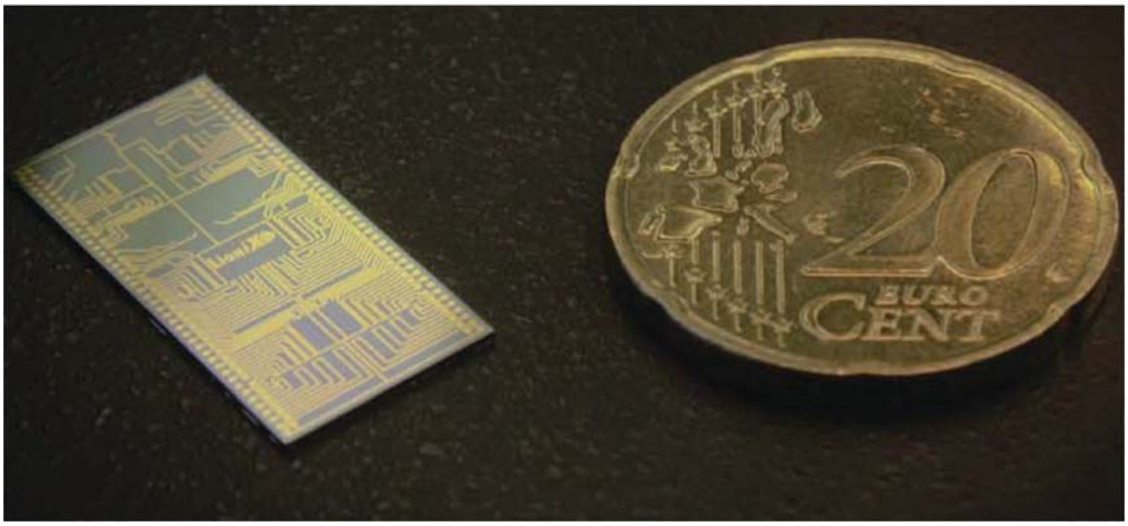

Figure 1.5 A microwave photonic chip pictured with a 20 Euro-Cent coin for size comparison.

has yet to outpace the performance of traditional microwave solutions. A second limitation is reliability, size and cost. Currently most microwave photonic systems consist of discrete components (i.e. laser, modulator, photodiodes and other passive optical components). Since discrete components occupy large space, it is impractical to employ microwave photonic systems for those applications that require small size or volume, such as avionic, submarine, or ship applications. At the same time, these discrete components tend to have poor reliability as well as high system cost since each component has packaging cost. If microwave photonics systems can be more viable in terms of cost, power consumptions and reliability, they will be able to replace microwave solutions for processing beyond only replacing the coaxial cables. In order to address these limitations, integrated microwave photonics has been proposed and demonstrated [2, 3]. With photonic integration, one can achieve a reduction in footprint, inter-element coupling losses, packaging cost as well as power dissipation [18]. Figure 1.5 shows a microwave photonic chip pictured with a 20 Euro-Cent coin for size comparison.

Silicon photonics has been studied as a a technology with a considerable potential for integrated microwave photonics since high refractive index contrast can be achieved and it is compatible with CMOS fabrication technology. Photonic integrated circuits for communication and military applications require the integration of light sources and photodiodes. Given the indirect bandgap of silicon and its transparency at telecommunication wavelengths, it is challenging to achieve active components (i.e. laser and photodiode) on a silicon platform. To date III-V compound optoelectronic components have achieved the best microwave photonic performance, since they enable complex bandgap engineering. Photodetectors fabricated from III-V compounds have demonstrated low dark current, high output RF power, and high linearity [19]. In order to enable high-performance active components on silicon platform and achieve heterogeneous integration, wafer bonding techniques have been demonstrated [20]. By integrating active components and passive components on one chip, an on-chip high-performance microwave photonic system could be achieved which would provide a path to large-scale industrial and military employment.

1.4 Preview of dissertation

The primary focus of this dissertation has been investigation and demonstration of high power photodiodes (including normal-illuminated photodiodes and waveguide photodiodes) and their application in microwave photonics. The charge-compensated modified uni-traveling carrier (CC-MUTC) photodiodes described in this Ph.D dissertation have achieved better performance than other types of photodetectors with respect to the figures of merit that are important for analog optical links. To the best of my knowledge, this Ph.D work has achieved the following records:

- InP-based photodiodes heterogeneously integrated on SOI with the highest reported output power for any waveguide photodiode technology
- Flip-chip-bonded-on-diamond InP/InGaAs CC-MUTC photodiode with record RF output power of 1.8 W at 10 GHz
- First InP photodiode heterogeneously integrated on silicon-on-diamond
- First demonstration of photodiodes with record power conversion efficiency that approaches the class AB power conversion efficiency limit

- First demonstration of photonic generation of high power pulsed RF signal with > 10 W peak power level
- CC-MUTC photodiode with record peak voltage and bandwidth product among.

As mentioned in the acknowledgements, it is important to point out that the work on high power photodiodes is based on the collaboration between Aurrion Inc., Dr. Qiugui Zhou, and me. My contributions are in fabrication, photonic device characterization, and system testing. Dr. Qiugui Zhou designed the wafer structure and wafer bonding was done by Aurrion Inc.

In Chapter 2, high-power photodiodes are reviewed, including the factors that limit output power, approaches to circumvent these limitations, and the fabrication process flow.

Chapter 3 will discuss high power photodiodes flip-chip bonded on diamond submounts including device structure, thermal simulation, modulation depth enhancement, and experimental results. In Chapter 3, flip-chip-bonded-on-diamond InP/InGaAs CC-MUTC photodiodes with record power of 1.8 W output RF power at 10 GHz are described. Compared with previously reported RF power, the devices on diamond submount achieve >80% higher RF output power. These photodiodes have also demonstrated record power conversion efficiency of 50.7% to 60% at 6 to 10 GHz with ~ 27.8 dBm RF output power.

In Chapter 4, a high-gain, low-noise-figure, and high-linearity analog photonic link based on the CC-MUTC high-power photodiodes will be discussed and experimental results will be shown. In Chapter 5, these photodiodes are used to demonstrate photonic generation of high-power pulsed microwave signals. The impulse response without RF modulation achieved unsaturated peak voltage of 33.5 V and full width at half maximum (FWHM) of 50 ps. The peak power levels for gated modulation at 1 GHz and 10 GHz were 41.5 dBm (14.2 W) and 40 dBm (10 W), respectively.

In Chapter 6, InP-based high-power and high-speed modified uni-traveling carrier photodiodes heterogeneously integrated on silicon-on-insulator (SOI) waveguides are demonstrated. Single devices can exhibit either an internal responsivity up to 0.95 A/W or a bandwidth up to 48 GHz. The maximum output RF power of a 10×35 μm^2 photodiode was 12 dBm at 40 GHz. Using the same integration technology balanced waveguide photodiodes with 0.78 A/W internal responsivity, 14 GHz bandwidth, and >20 dB common-mode rejection ratio (CMRR) have been demonstrated. In differential mode the unsaturated RF output power was 17.2 dBm at 10 GHz and 15.2 dBm at 20 GHz.

The last chapter concludes my Ph.D. work and proposes future research directions.

Chapter 2 Review of High-Power Photodiode

2.1 Introduction

As discussed in Chapter 1, one of the most important figures of merit for photodiodes in analog links is power handling capability, which impacts the link gain, noise figure, and dynamic range. In this chapter, some of the factors that limit output power are discussed, including the space charge effect, thermal failure, and non-uniform absorption profile. Approaches to moderate these limitations are also discussed. The saturation mechanisms in conventional PIN photodiodes, uni-traveling-carrier (UTC) photodiodes, and modified uni-traveling-carrier (MUTC) photodiodes are illustrated. Finally the fabrication process flow will be described, including metal deposition, mesa etch, contact formation, pad metal deposition, Au electro-plating, polishing, and dicing.

2.2 Limitations of high power photodiodes

PIN photodiodes are the most common type of photodiodes utilized in optical communication systems owing to their simple structure, high quantum efficiency, and high bandwidth. Communication PIN photodiodes consist of a narrow bandgap depleted absorption region (typically InGaAs) sandwiched between highly n-doped and p-doped InP layers as shown in Figure 2.1. The built-in potential and applied bias voltage establishes the electric field in the absorption region. Light can be input from the top or the bottom of the photodiode. Carriers generated in the absorption layer drift toward the InP cladding layers. Compared with a traditional PN photodiode, a PIN photodiode contains a thicker depletion region, which increases the absorption volume, which results in higher quantum efficiency. In addition, the lower capacitance of the thick depletion region enables higher bandwidth.

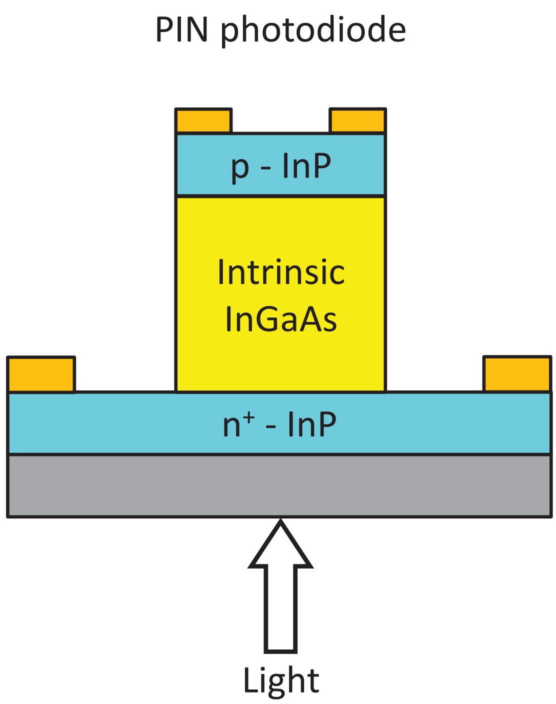

Figure 2.1 Schematic cross section of a PIN photodiode.

PIN photodiodes can be vertically illuminated, side-illuminated, and evanescently-coupled as shown in Figure 2.2 [21]. Vertically illuminated PIN photodiodes (Figure 2.2(a)) have the advantages of high alignment tolerance and simple structures. However, the bandwidth-efficiency-product of vertically illuminated PIN photodiodes is limited to approximately 20 GHz [22]. The side-illuminated PIN waveguide photodiodes and evanescently-coupled PIN waveguide photodiodes shown in Figure 2.2 (b) and (c) overcome the inherent bandwidth-efficiency limitation as high efficiency and short carrier transit times can be achieved simultaneously [23].

High photocurrent levels are determined by three factors: the space charge effect, thermal failure, and non-uniform absorption profile. In the following sections, these three factors will be described in detail.

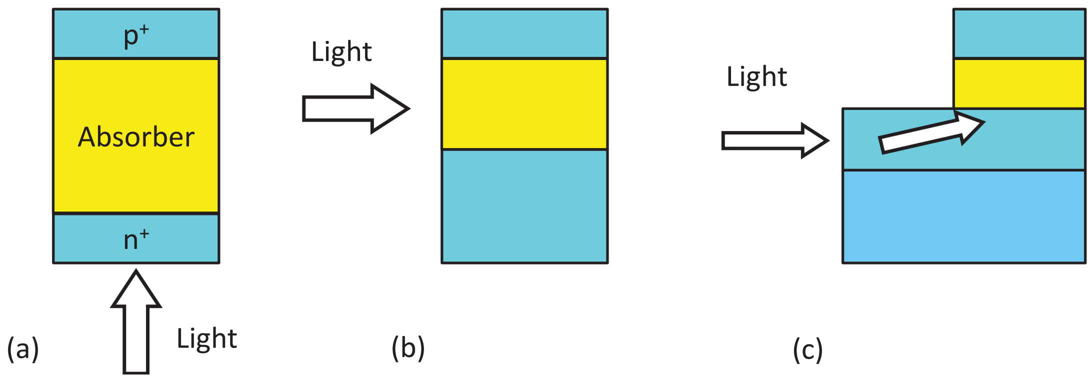

Figure 2.2 (a) Vertically illuminated PIN photodiodes, (b) side-illuminated waveguide PIN photodiode and (c) evanescently-coupled waveguide PIN photodiodes.

2.2.1 Space charge effect

One of the most important factors to achieve high photocurrent levels the space charge effect [24]. As shown in Figure 2.3 (a), photons with energy larger than the InGaAs bandgap in the intrinsic region can be absorbed and electrons and holes will be generated. The electrons drift toward the n-doped region and holes toward the p-doped region. As the optical power increases, the excess carrier densities near the n and p regions create an electric field that opposes bias field. Therefore, the electric field in this depleted region is screened by these charges and due to the unbalanced carrier density distribution, the electric field collapses within the depletion region, as shown in Figure 2.3 (b). As a result, at low fields the carriers no longer maintain saturation velocity. This is especially pronounced for holes as can be seen by the plots of carrier velocity versus electric field in Figure 2.3 (c). Note that at low electric field electrons may exhibit a higher velocity due to overshoot. However in PIN photodiodes, holes are the primary limitation since holes have a much slower velocity. The field collapse causes the bandwidth to decrease and the RF output power saturates. This is referred to as the space charge effect.

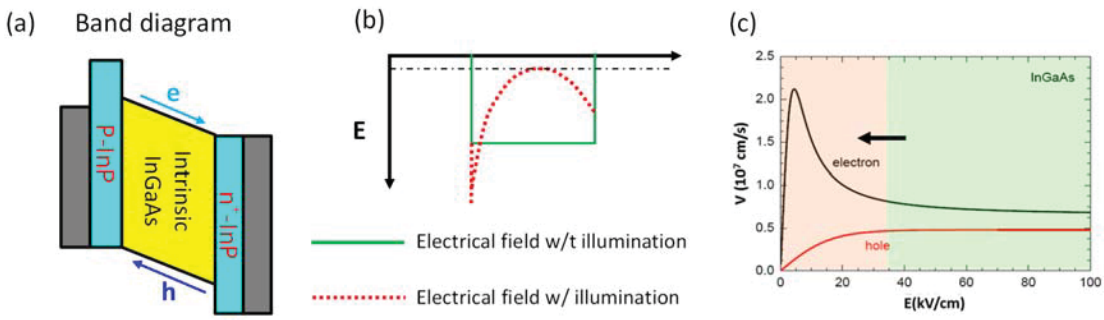

Figure 2.3 (a) Band diagram, (b) electric field of PIN photodiodes, and (c) velocity of electrons and holes in InGaAs.

2.2.2 Thermal failure

Another limitation for PIN photodiodes is thermal failure. PIN photodiodes are susceptible to thermal failure due to the poor thermal conductivity of InGaAs. As discussed above, photogenerated electrons and holes in the intrinsic/depletion region are

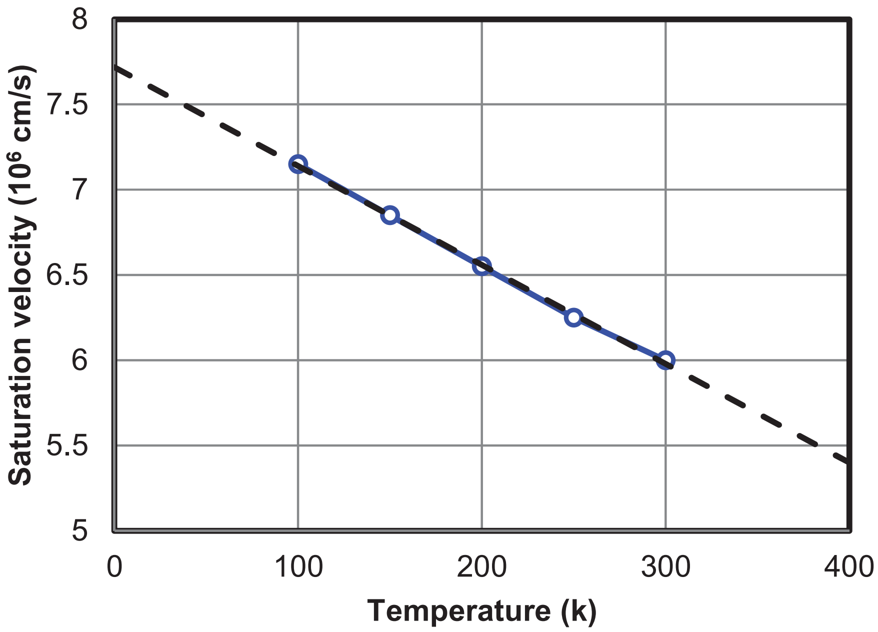

Figure 2.4 Electron saturation velocity versus temperature for InGaAs.

able to drift with the saturation velocity through the intrinsic region only if the electric field is high enough. Therefore the simplest method to mitigate space charge effect is to increase bias voltage applied on photodiode and thus increase the electric field across depletion region. However, the high electric field in the intrinsic InGaAs absorber is responsible for most of the heat generation in a PIN photodiode. Most of the power dissipation in the photodiode occurs in the InGaAs depletion region [25]. Heat propagation through the device is mostly in the vertical direction toward the substrate. Since InGaAs has a relative low thermal conductivity of 0.05 $W \cdot cm^{-1} \cdot °C^{-1}$, heat generated in the InGaAs region cannot be efficiently dissipated to the InP contact layer and substrate. As a result, the junction temperature increases dramatically at high bias. Figure 2.4 shows electron saturation velocity versus temperature for InGaAs. It can be observed that the saturation velocity decreases as temperature increases. Therefore under high power level, the space charge effect will be enhanced due to the lower saturation velocity at high junction temperature.

In addition to slower saturation velocity, heat generated in the InGaAs depletion region eventually leads to thermal failure. An increase in junction temperature reduces the engergy band gap of InGaAs, as shown in Figure 2.5, and thus results in higher dark current, which in turn increases the junction temperature. Since InGaAs is a narrow-bandgap semiconductor, its critical temperature for thermal runaway is relatively low. At high temperatures, this process becomes unstable and the current increases until the device fails.

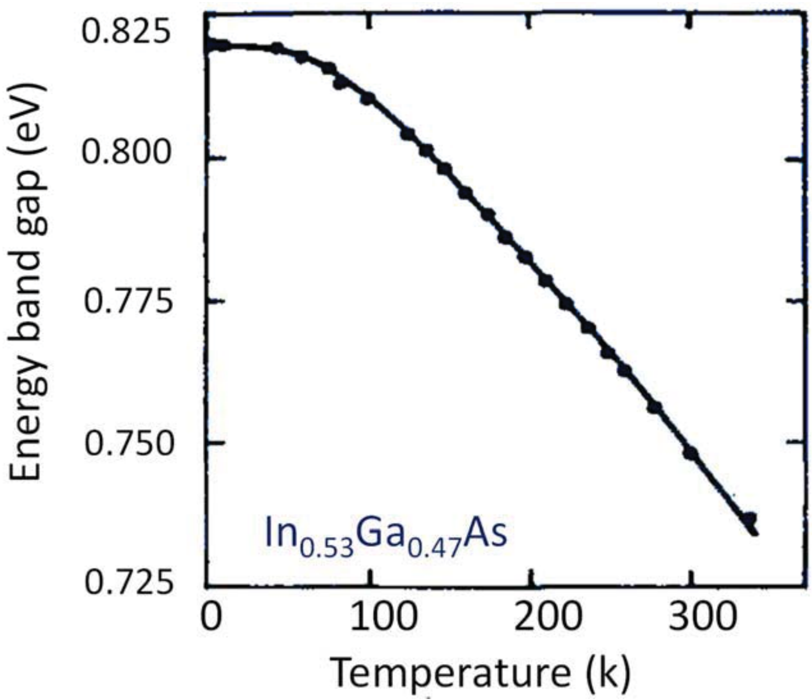

Figure 2.5 Energy band gap versus temperature for InGaAs.

2.2.3 Nonuniform absorption profile

In addition to the space charge effect and thermal failure, a nonuniform absorption profile adversely affects the performance of waveguide photodiodes. For side-illuminated PIN waveguide photodiodes, the absorption layer is designed as a thin layer to reduce the transit time across the depletion region. In order to input an optical signal into the thin absorption layer, a lensed fiber is frequently used to improve the coupling efficiency. Therefore, the optical intensity at the input facet is high and most of light is absorbed near the input facet. This is referred to as a nonuniform absorption profile, which exacerbates saturation and thermal failure. For evanescently-coupled PIN waveguide photodiodes, the light that propagates in a waveguide adjacent to the absorption layer couples evanescently. Compared with side-illuminated PIN waveguide photodiodes, this coupling provides a more uniform absorption profile [26]. This waveguide photodiode structure is well suited for monolithic integration with other components, such as waveguide networks and power splitters, which is beneficial for advanced detector structures with increased functionality. However, at high power levels, the residual nonuniformity still poses a limitation. Commercial beam propagation software can be used to tailor the evanescently-coupled absorption profile. In [27], modified uni-traveling carrier photodiodes on silicon-on-insulator were demonstrated. Figure 2.6 (a) shows the cross-section of the MUTC photodiode on SOI and Figure 2.6 (b) shows the simulated relative optical intensity profile in the absorption layer of the devices reported in [27]. The simulation shows that the optical intensity peaks in the first 10 μm and remains considerably lower beyond 40 μm. Assuming that the carrier generation is proportional to

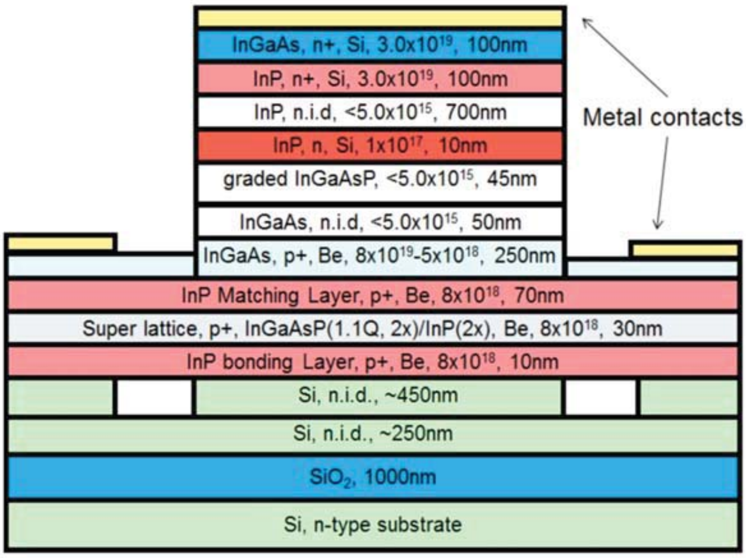

(a)

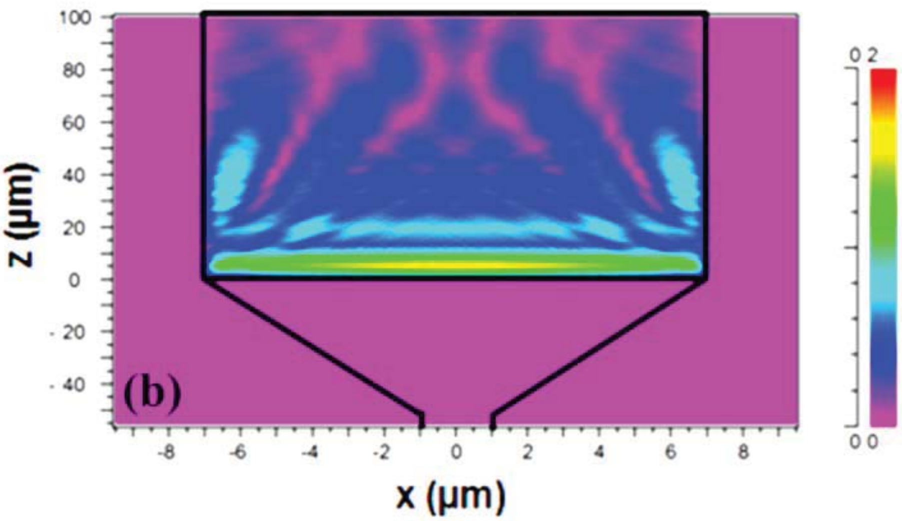

(b)

Figure 2.6 (a) Layer stack design of MUTC PD on SOI. Doping concentrations in cm^{-3}. (b) simulated relative optical intensity profile in the plane of the absorber layer of the structure in [27]. The tapered silicon waveguide extends from z=-50 to 0 μm. The active PD area extends from x=-7 to 7 μm and z = 0 to 100 μm.

the optical intensity, a non-uniform photocurrent distribution follows and that can lead to localized areas of strong saturation at high optical input powers [27]. By optimizing the structure of waveguide photodiode, an uniform absorption profile can be obtained [28]. More details will be presented in Chapter 6.

2.3 Approach to achieve high output power

As discussed above, the conventional PIN photodiodes is vulnerable to effects that limit the output power. In this section, approaches to overcoming these factors are discussed, including CC-MUTC photodiodes and flip-chip bond technique.

2.3.1 MUTC structure

Several photodiode structures have been proposed and demonstrated to achieve high power operation, including the partially depleted absorber (PDA) photodiode [24], the dual depletion region (DDR) photodiode [29], uni-traveling carrier (UTC) photodiode [30, 31], and the near-ballistic UTC (NB-UTC) photodiode [32, 33]. The photodiode that has achieved the best overall performance is the uni-traveling carrier (UTC) photodiode that was first demonstrated by T. Ishibashi et al. [30, 31]. Figure 2.7 shows the energy band diagram and electric field distribution of PIN photodiode and the UTC photodiode. As shown in Figure 2.7 (b), the structure of UTC photodiode consists of a p-doped InGaAs undepleted absorption layer and a transparent InP drift layer. Light entering the photodiode is absorbed in the InGaAs region. Since InGaAs absorption is undepleted p-doped, the excess hole density quickly decays at the dielectric relaxation time. The photo-

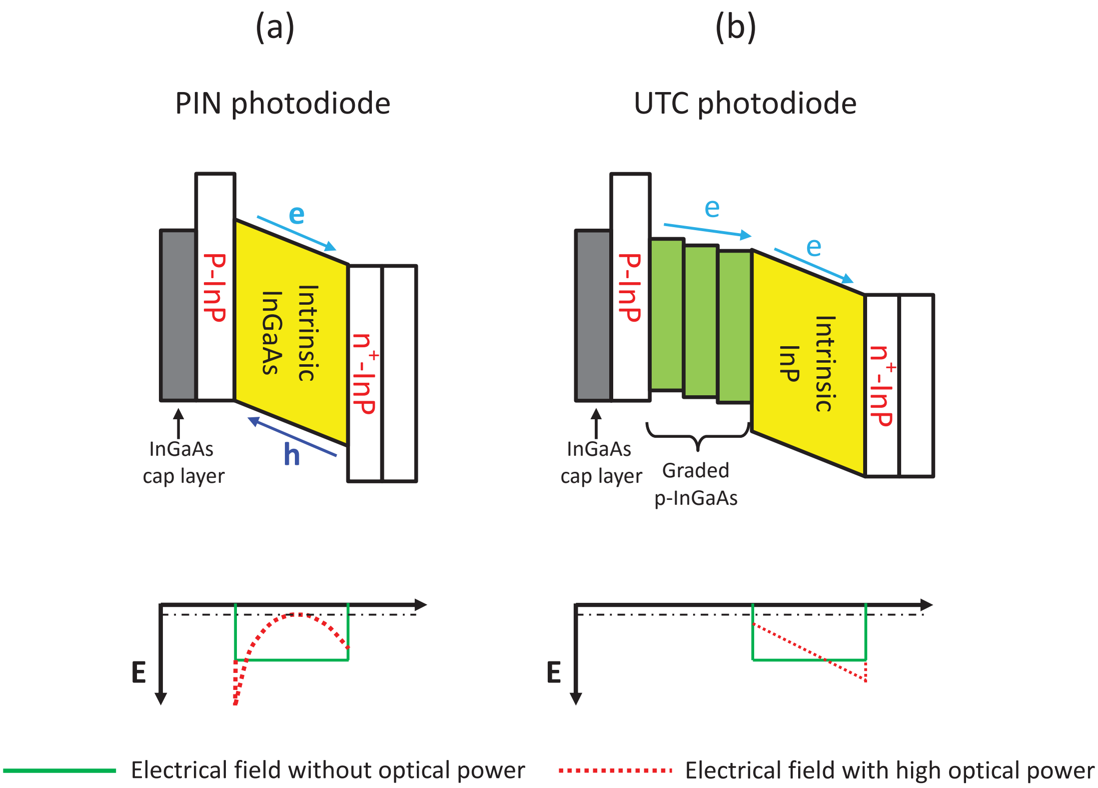

Figure 2.7 Energy band diagram and electric field distribution of (a) conventional PIN, (b) UTC photodiodes.

generated electrons diffuse across the InGaAs absorption layer and then drift in InP collection layer. The UTC structure has three advantages. First, the space charge effect can be mitigated significantly since only electrons transit the depleted drift region. Second, benefiting from the higher saturation velocity of electrons in InP collection layer, the bandwidth of the photodiode can be enhanced. Third, a wide band absorber is used as the drift region, which lowers the dark current and makes the photodiode less susceptible to thermal run away. Even though UTC photodiodes can reduce the space charge effect to some extent, space charge remains at high power level owing to single carrier injection. At high power level, the electric field collapses at the edge of depleted region, which limits the output RF power. Another issue for the UTC photodiode is that the energy barrier between the narrow bandgap material (InGaAs) and the wide bandgap material (InP) impedes the injection of electrons from the undepleted absorption layer into the collector region, especially at high power levels.

Based on conventional UTC photodiodes, three changes have been made to further mitigate the space charge effect. Figure 2.8 shows the band diagram and electric field distribution of the photodiode with these changes. The first change is that the InP collector layer is slightly n-doped [34]. This predistorts the electric filed so that a flat field profile can be achieved at high photocurrent level as illustrated in Figure 2.8 (a).

The second change is to partially deplete the absorption layer (Figure 2.8 (b)). This is accomplished by adding a lightly n-doped layer to the absorption region. This helps to prevent field collapse at the heterojunction interfaces and aids injection from the absorber to the drift layer at high current levels. This also improves the responsivity without sacrificing bandwidth.

The third change is to incorporate "cliff layer" which is a thin, moderately-doped n-type InP layer between the depleted InGaAs layer and the InP collector cf. Figure 2.8 (c). The electric field in the depleted InGaAs absorption layer is enhanced by the cliff layer, which helps maintain a high electric field across the heterojunction interfaces. By inserting the cliff layer, the photodiode is less susceptible to the space charge effect.

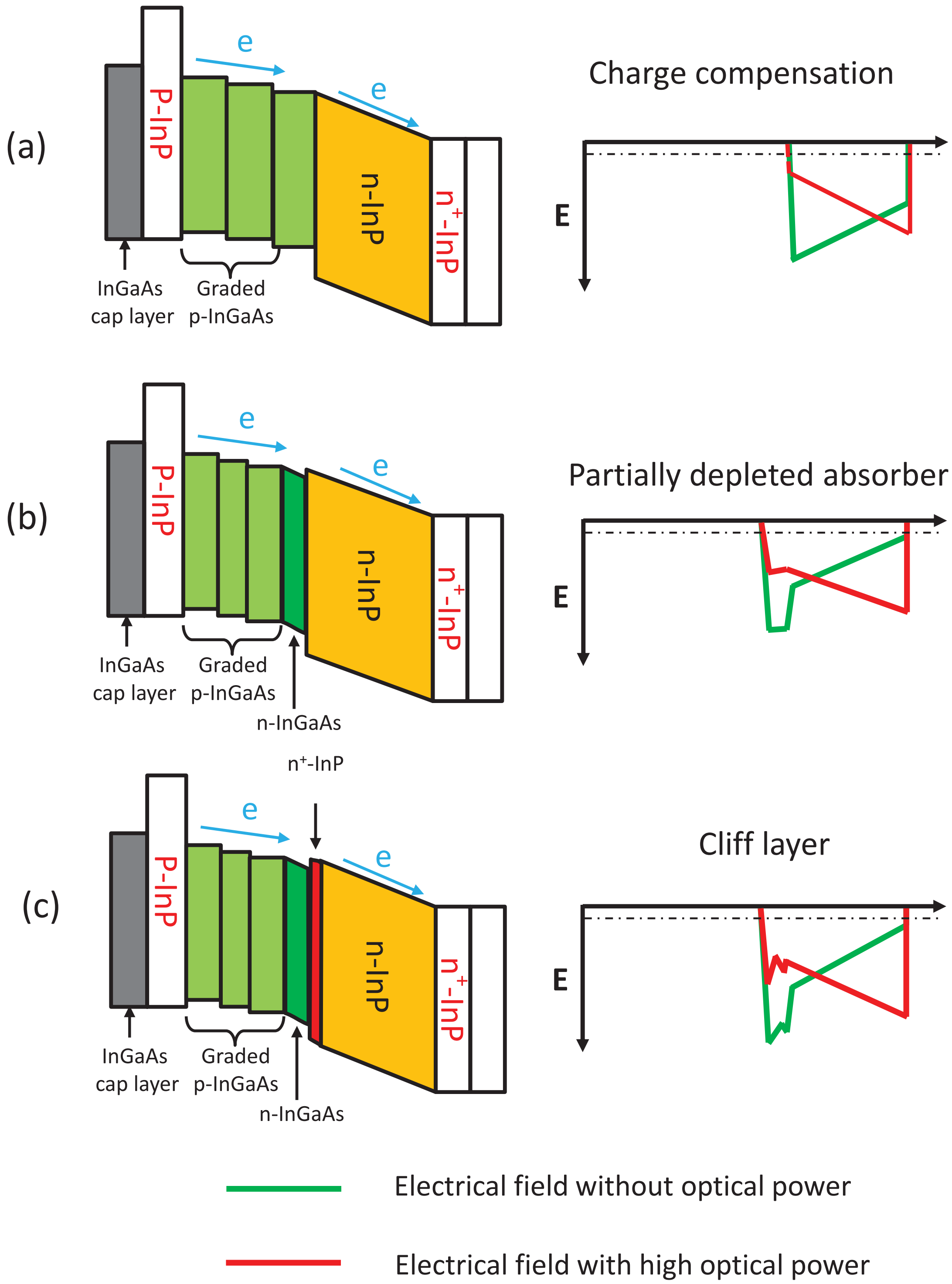

Figure 2.8 Band diagram and electric field distribution of CC-MUTC photodiodes.

2.3.2 Flip-chip bonding

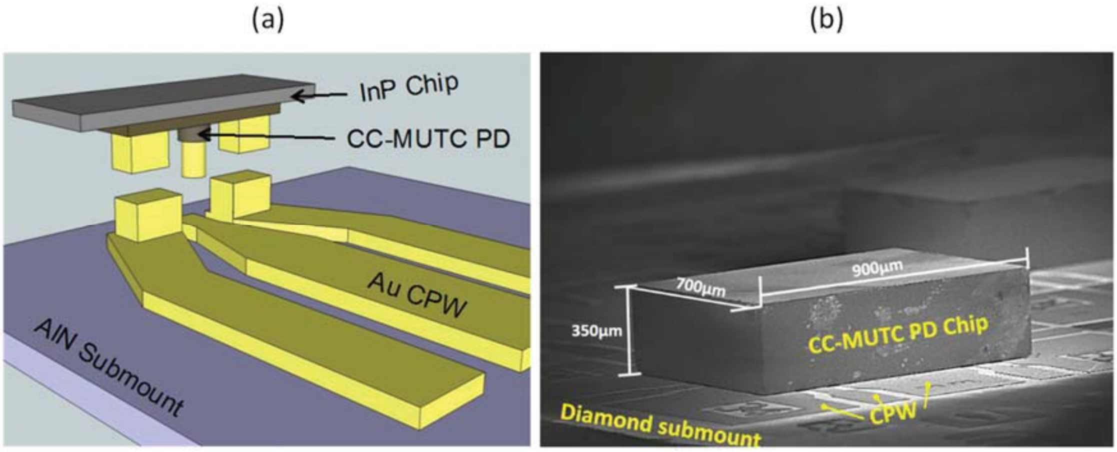

Figure 2.9 (a) Schematic plot of flip-chip bonding process and (b) microscope image of a flip-chip bonded device.

As discussed in the previous section, the space charge effect can be greatly reduced by structure design. Thermal management then becomes the most important issue to be addressed. In order to achieve higher output RF power, higher bias voltage has to be applied on photodiode. In order to improve thermal dissipation, a flip-chip bonding technique has been employed. A 3-D schematic plot of a flip-chip bond photodiode is illustrated in Figure 2.9 (a). Short gold contacts are plated on the mesas and the coplanar waveguide contact (CPW) pad on a high-thermal-conductivity submount such at AlN. By thermal bonding, the gold contacts on the mesa act as both an electrical path and heat dissipation channels. Figure 2.9 (b) shows a microscope image of a flip-chip bonded device. A bonding machine from FINETECH was used to flip-chip bond the chips onto the submount. In order to determine the positional precision of the machine, I flip-chip bonded tens of chips on AlN submounts and then de-bonded the chips from the submount. Figure 2.10 shows the bonding point after de-bonding. It can be seen that there is a 10-μm offset from the desired bonding points. This is an acceptable offset for high power photodiode with diameter of > 20 μm.

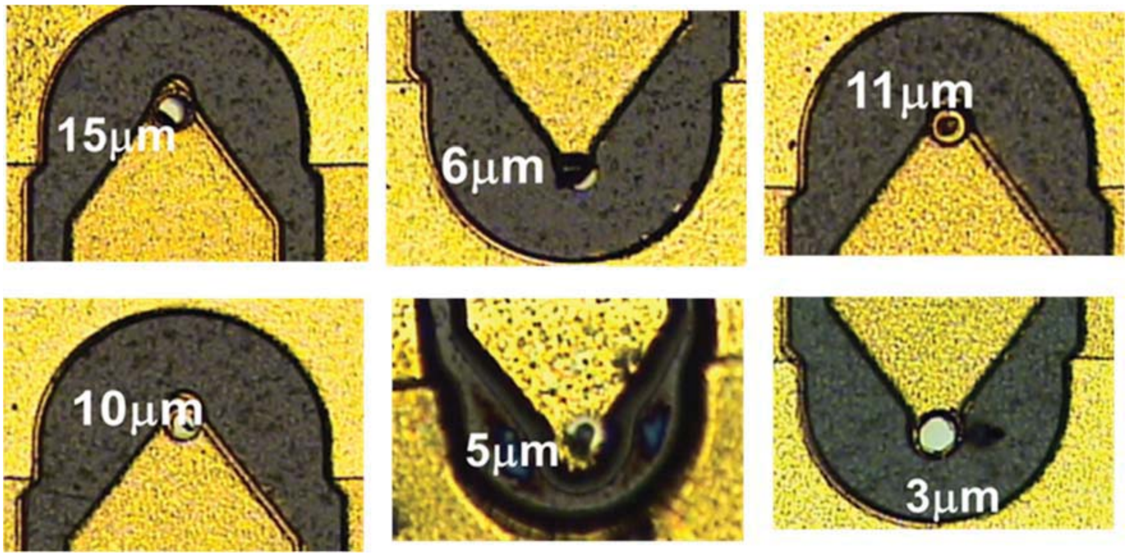

Figure 2.10 Bonding positions of the chips on the submount after de-bonding.

2.4 Fabrication process flow

The fabrication process for the MUTC photodiodes used in this work is described in this section. Figure 2.11 shows a cross section of a back-illuminated photodiode, a top-view photograph of a fabricated device, and the fabrication process flow. As shown in Figure 2.11 (a), the photodiode has double mesas with deposited metal on top of each mesa. An air bridge is formed to connect the p contact to the CPW pad on semi-insulating substrate. SiO_2 is deposited on the sidewall of the mesa as a passivation layer to reduce surface leakage current. The backside of the photodiode is coated with 250-nm SiO_2 as an anti-reflection coating. Figure 2.11 (c) describes the fabrication process flow, which can be cataloged as four major steps, including metal deposition, mesa etching, oxide deposition, and gold electro-plating.

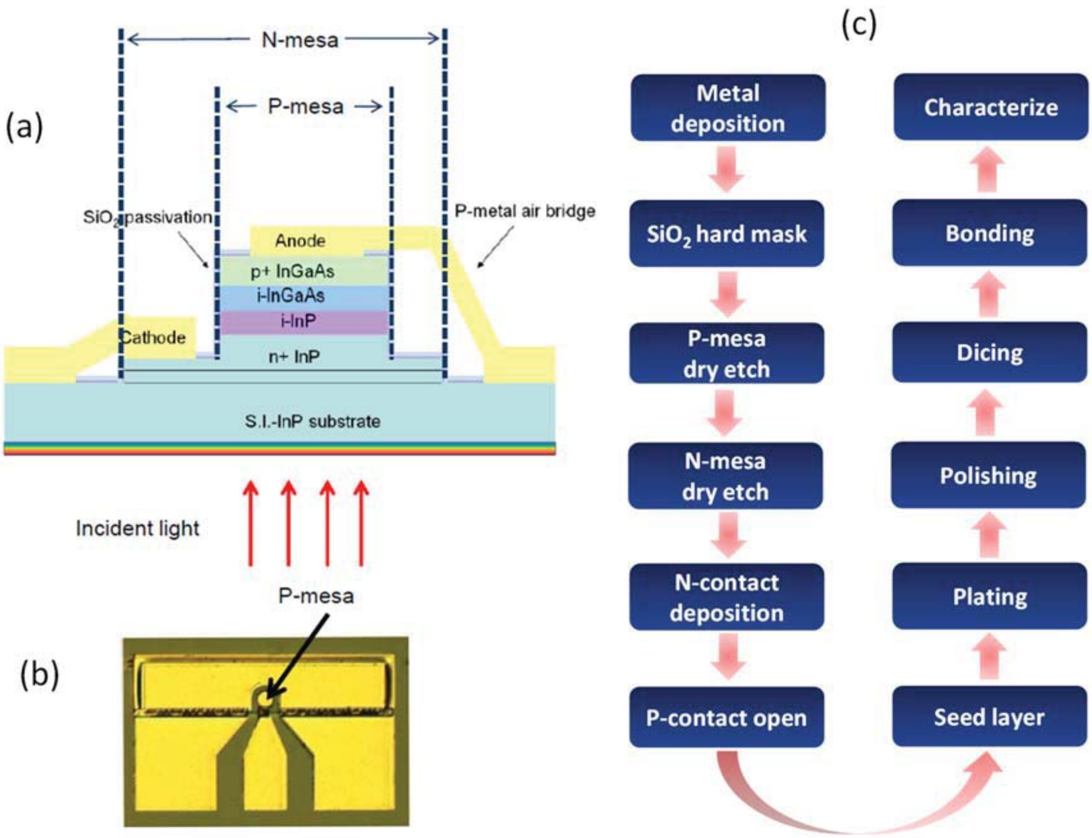

Figure 2.11 (a) Cross section of back-illuminated photodiode, (b) top view of a photodiode, (c) fabrication process flow.

2.4.1 Metal deposition

Metal deposition includes p-contact and n-contact deposition, and seed layer formation for electro-plating. The metal deposition is finished by an electron beam (E-beam) evaporator. The metal pattern is defined by lithography before metal deposition. Oxygen plasma is used before E-beam evaporation to remove any possible photoresist residues in the open windows. For p-contact formation, Ti (20 nm)/Pt (20 nm)/Au (80 nm) are deposited sequentially. For n-contact formation, AuGe (30 nm)/Ni (20 nm)/Au (80 nm) are deposited. The Ti and AuGe are used as adhesion to the InGaAs top layer. The Pt and Ni prevent gold spiking into the semiconductor. The Au provides a good electrical conductance and the following gold plating is deposited on the evaporated Au layer. Au is deposited on the whole surface of the wafer with patterned photoresist in the E-beam evaporator. The n-contact and p-contact are formed by a lift-off procedure. During the lift-off process, the wafer is immersed in a solvent solution (e.g. acetone or a mixture of N-Methyl-2-pyrrolidone (NMP) and polyethylene glycol (PEG)) to remove the metal on the photoresist, leaving only the metal that adheres to n mesa and p mesa surfaces.

2.4.2 Mesa etching

Since the photodiode has the double mesas shown in Figure 2.11 (a), two mesa etching steps are required. The first step is p-mesa etching that defines the active area of the photodiodes. This etching step stops at the n-contact layer that is highly-doped in order to reduce the contact resistance. The n-mesa is formed by dry etching. Its function is to isolate different devices and reduce leakage current and parasitic capacitance. Before the two mesa etching steps, a SiO2 layer is deposited by PECVD to serve as a hard mask and passivation layer.

The mesa pattern is defined by photolithography and transferred from a hard mask to InP/InGaAs layers by either wet chemical etching (H_3PO_4:H_2O_2:H_2O or bromine: methanol) or dry etching (inductively coupled plasma (ICP) etching). H_3PO_4:H_2O_2:H_2O

(volume 1:1:10, etch rate 0.5~0.6 μm/min) is used to selectively etch InGaAs since H_3PO_4:H_2O_2:H_2O does not attach InP. Bromine: methanol (volume 1:200~250, etch rate 0.2~0.3 μm/min) etches both InGaAs and InP but it tends to leave deep trenches around the edge of the mesa.

ICP etching is carried out using the Oxford RIE-ICP system. The recipe is Cl_2 (20 sccm):N_2 (8 sccm) gas mixture at 40 °C and 4 mTorr pressure. The IPC power is set as 150 W and forward power is set at 50 W. Dry etching attacks both InGaAs and InP with an etch rate of 10 nm/min. The selectivity between InP/InGaAs and SiO_2 is ~ 2.5:1. Laser-interferometry end point detection is used to monitor the etching progress. After dry etching, the wafers are dipped into bromine: methanol for 5~10 seconds to remove sidewall damage.

2.4.3 Oxide deposition

SiO_2 serves as the etch mask, passivation layer, and anti-reflection (AR) coating in the fabrication process. It is grown in the plasma enhance chemical vapor deposition (PECVD) system using SiH_4 (400 sccm) and NO_2 (105 sccm) gas mixture at 285 °C. A conditional run without the wafer in the chamber is carried out to remove any un-related chemical residue in the chamber and to ensure the SiO_2 quality. The SiO_2 film thickness is measured using the Filmetrics spectral reflectance machine on a Si dummy wafer. The growth rate of SiO_2 is 10 ~ 12 nm/min. The SiO_2 hard mask is patterned by ICP dry etching. The recipe is forward power of 150 W and CHF_3 (25 sccm) at 20 °C and 10 mTorr pressure. The selectivity between SiO_2 and photoresist AZ 5214 is ~ 1:1.

2.4.4 Gold electro-plating

Electro-plating is used to form air-bridge channels to connect the mesa contact and CPW pad on the substrate. It is a double-mask procedure that needs two steps of lithography to pattern the plating area. First the mesa contact and CPW pad are defined by photolithography. The photoresist in these areas is removed during the developing process. A long hard-bake process is applied before the second photolithography to prevent a bubbling effect during baking in the second photolithography. A metal stack of Ti (20 nm)/Au (80 nm) is deposited as the seed layer for plating. After the metal deposition, a second photolithography is carried out directly without lifting off the first layer of photoresist and metal. The mesa contact, air bridge, and CPW pad areas are all exposed after this photolithography. Oxygen plasma ashing (150W, 5 min) is used to remove any possible photoresist residue in the open areas. The wafer with seed layer is placed in a gold plating solution at 60 °C during the plating process. The plating current is 1 mA and the voltage is ~ 0.5 V. Finally the whole wafer is immersed into acetone solution with ultrasonic agitation to remove the plated gold on the hard baked photoresists.

2.4.5 Additional Processing

Additional processing steps usually include wafer polishing and wafer dicing. The purpose of polishing is to remove any residues attached to the backside of the wafer and improve responsivity. This is accomplished using the Logitech polishing machine. A SiO_2 anti-reflection layer is deposited after polishing. Finally the wafer is diced into small chips for flip-chip bonding. A layer of photoresist is spun onto the top surface of an InGaAs/InP wafer in order to protect the devices from accidental damage during the dicing process. The InGaAs/InP wafer is glued onto a silicon carrier wafer by black wax for support.

Chapter 3 High-Power Photodiodes Flip-Chip Bonded on Diamond

3.1 Introduction

As stated in the second chapter, for normal-incidence high-power photodiodes, the space charge effect and thermal failure are the two primary factors that limit the RF output power. Optimizing the design of the epitaxial layer structure can effectively reduce the space charge effect. In 1997, Ishibashi et al. demonstrated the Uni-Traveling-Carrier (UTC) photodiode [30]. The UTC photodiode consists of a p-doped InGaAs absorption layer and a transparent InP drift layer. Light entering the photodiode is absorbed in the undepleted p-type InGaAs. Since the p-type InGaAs absorption region is undepleted, the excess hole density quickly decays at the dielectric relaxation time. The photogenerated electrons diffuse across the absorption region and then drift in the InP collection layer. This configuration reduces the space charge effect and results in high RF output power while maintaining high-speed and high-linearity.

However, at high power level, the electric field collapses at the edge of depleted region, which limits the output RF power of UTC photodiodes. The CC-MUTC structure has been developed to mitigate the space charge effect, which has been discussed in Chapter 2. A back-illuminated modified uni-traveling carrier (MUTC) photodiode exhibited a responsivity of 0.75 A/W, bandwidth of 14 GHz and 25-dBm RF output power at 14 GHz [35, 36]. In order to increase the output power, photodiodes have to be operated at high reverse bias, which gives rise to a dramatic increase heat. Therefore the photodiodes in [35] experienced thermal failure at 6 V bias voltage.

In order to improve heat dissipation, a flip-chip bonding technique has been employed. Initially, photodiodes were flip-chip-bonded on high-impedance silicon submounts. This resulted in an increase in output RF power up to 27.4 dBm at 9 V bias voltage [37], which is more than twice the maximum output power of the backside-illuminated photodiodes [35]. The thermal conductivity of Si is 142 W/mK. Aluminum nitride (AlN) has a higher thermal conductivity of 285 W/mK, which is twice that of Si. Using AlN submounts at 15 GHz the output power was increased to 28.8 dBm and the saturation photocurrent was > 180 mA at 11 V reverse bias [38] . Diamond has even higher thermal conductivity, 1000 ~ 1800 W/mK [39]. In this work, chemical-vapor-deposition (CVD) diamond was used as the submount.

3.2 Device structure

Table 3.1 shows the epitaxial structure of the InP/InGaAs wafer, which is the same as the previously reported photodiodes in [38]. The epitaxial layer structure was grown by Metal-Organic Chemical Vapor Deposition (MOCVD) on semi-insulating InP substrate. Figures 3.1 shows the schematic cross-sectional view. In the MUTC photodiode, the N-contact layer is highly n-doped (1×10^{19}). The 900 nm lightly n-doped drift layer acts as a space-charge compensation layer where the electric field is predistorted to achieve a flat electric field profile at high photocurrent. In addition, a cliff

Table 3.1 Epitaxial layer structure of InP/InGaAs wafer used to fabricate MUTC photodiodes

Layer	Material	Doping (cm^{-3})	Thickness (nm)
P-contact	$InGa_{0.47}As_{0.53}$	p+ doping, 2×10^{19}	50
Block layer	InP	p+ doping, 1.5×10^{18}	100
Quaternary layer	InGaAsP, Q 1.1	p+ doping, 2×10^{18}	15
Quaternary layer	InGaAsP, Q 1.4	p+ doping, 2×10^{18}	15
Graded doped absorber	InGa0.47As0.53	p+ doping, $5\times10^{17}\sim2\times10^{18}$	700
Depleted absorber	$InGa_{0.47}As_{0.53}$	n- doping, 1×10^{16}	150
Quaternary layer	InGaAsP, Q 1.4	n- doping, 1×10^{16}	15
Quaternary layer	InGaAsP, Q 1.1	n- doping, 1×10^{16}	15
Cliff layer	InP	n doping, 1.4×10^{17}	50
Drift layer	InP	n- doping, 1×10^{16}	900
N-contact	InP	n+ doping, 1×10^{19}	1000
Substrate	InP, semi-insulating, double side polished		

layer with doping level of 1.4×10^{17} and thickness of 50 nm is used to enhance the electric field in the depleted portion of the absorption layer in order to assist electron transport across the heterojunction interface at high photocurrent. Two 15 nm quaternary layers are used to “smooth” the abrupt conduction band barrier at the InGaAs-InP heterojunction interface between InP and InGaAs. This can prevent electrons from accumulating at the heterojunction interface. The doping in the p-type absorber was “graded” in three steps (5

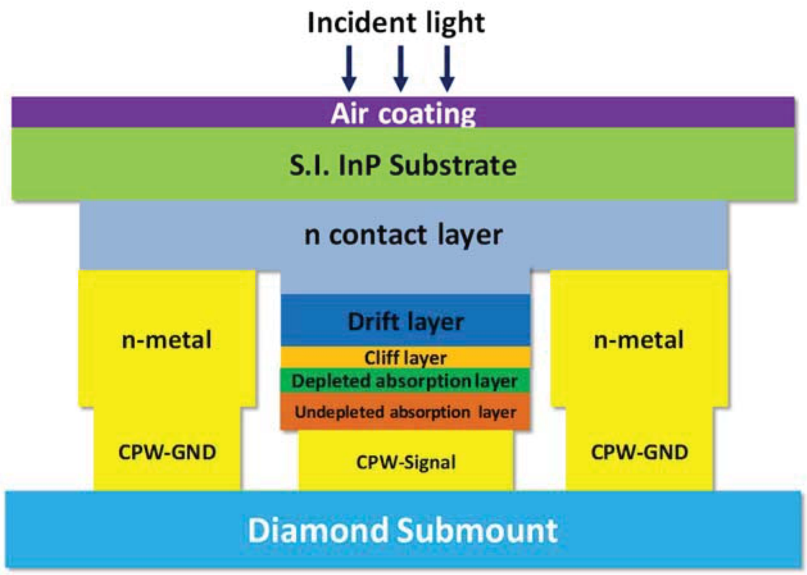

Figure 3.1 Schematic cross section of CC-MUTC photodiodes flip-chip bonded on diamond submount.

$\times 10^{17}$ cm^{-3}, 1×10^{18} cm^{-3}, and 2×10^{18} cm^{-3}) to form a quasi-electric field to aid carrier transport in the absorbing layer. The effect of this grading is to enhance diffusion transport and, thus, enhance the bandwidth.

Figure 3.2 shows the band diagram and electric field distribution of a PIN photodiode, UTC photodiode, and MUTC photodiode. Compared with a typical PIN photodiode and conventional UTC photodiode, the MUTC photodiode is designed to mitigate saturation, which occurs when the electric field drops below that required to maintain saturation velocity, which results from space charge. These modifications to the conventional UTC structure have resulted in high saturation current and high RF output

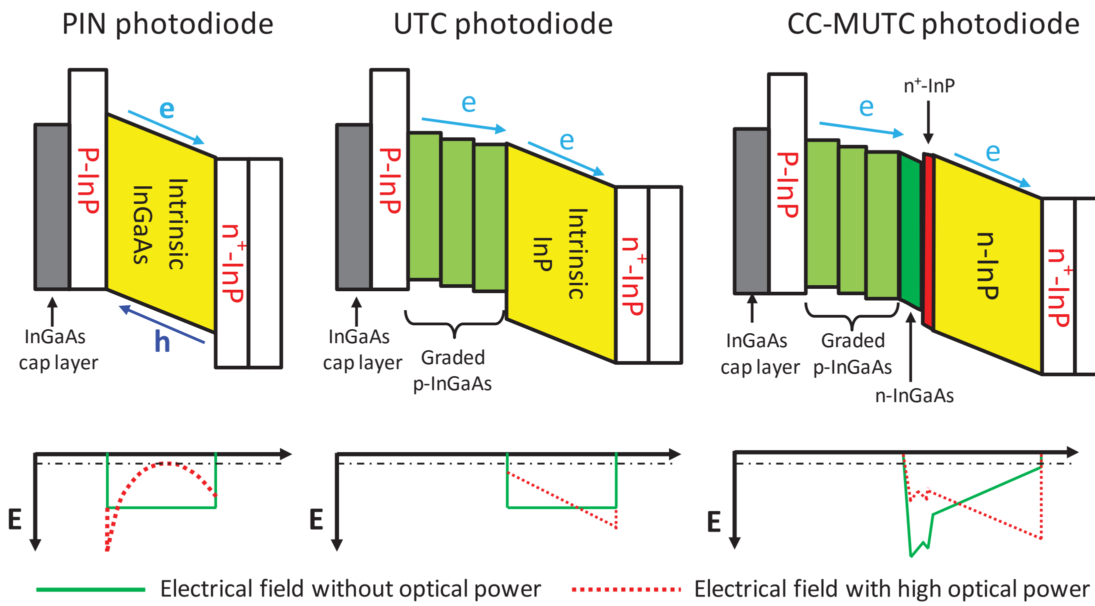

Figure 3.2 Band diagrams and electrical filed distributions of PIN, UTC and CC-MUTC photodiodes.

power [35]. The active area of the device was defined by a dry-etched double-mesa procedure. A Ti/Pt/Au metal stack was deposited as both p- and n-type contacts. In order to flip-chip bond chips on diamond submount, Au bonding bumps with a diameter of 6 µm and a height of 2 µm were plated on the p and n contacts. A 250-µm-thick SiO_2 layer was deposited on the back of the wafer as an anti-reflective (AR) coating by using PECVD, and then the wafer was diced into 0.7 × 0.9 mm^2 chips using a Disco Blade Saw. The diced chips were flip-chip bonded onto a high-thermal-conductivity diamond submount with coplanar waveguide (CPW) pads using a FINEPLACER® pico ma system. Figure 3.3 shows a scanning electron microscope (SEM) image of the flip-chip bonded photodiodes. Through the Au bonding bumps and CPW pads, the Joule heat generated in the junction can be dissipated to the diamond submount.

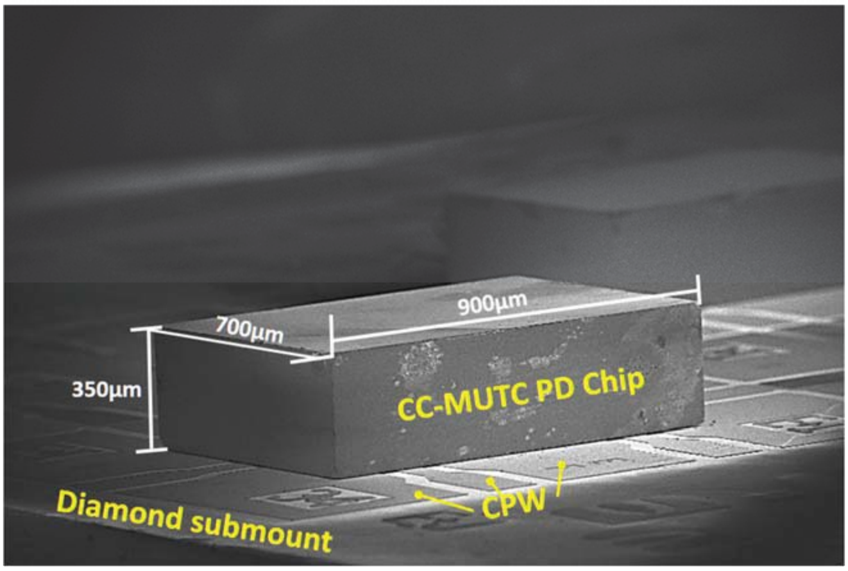

Figure 3.3 Scanning electron microscope (SEM) image of the CC-MUTC photodiodes flip-chip bonded on diamond submount.

3.3 Thermal Simulation

In order to illustrate how the submount reduces the device temperature, a 3-D thermal model based on the finite-element simulator COMSOL Multiphysics was created. The total power applied to the photodiode and load is the sum of the input optical power and the product of the applied bias and the operating average photocurrent. The power dissipated in the photodiode is estimated by subtracting the power on the load from the total power. Most of power dissipation in the photodiode occurs in the 1.1-µm thick depletion region including the 900-nm InP drift layer and the 150-nm InGaAs depleted absorption layer [25]. Most of the heat propagates through the device toward to diamond submount. In this model, convection and radiation from device to ambient are ignored

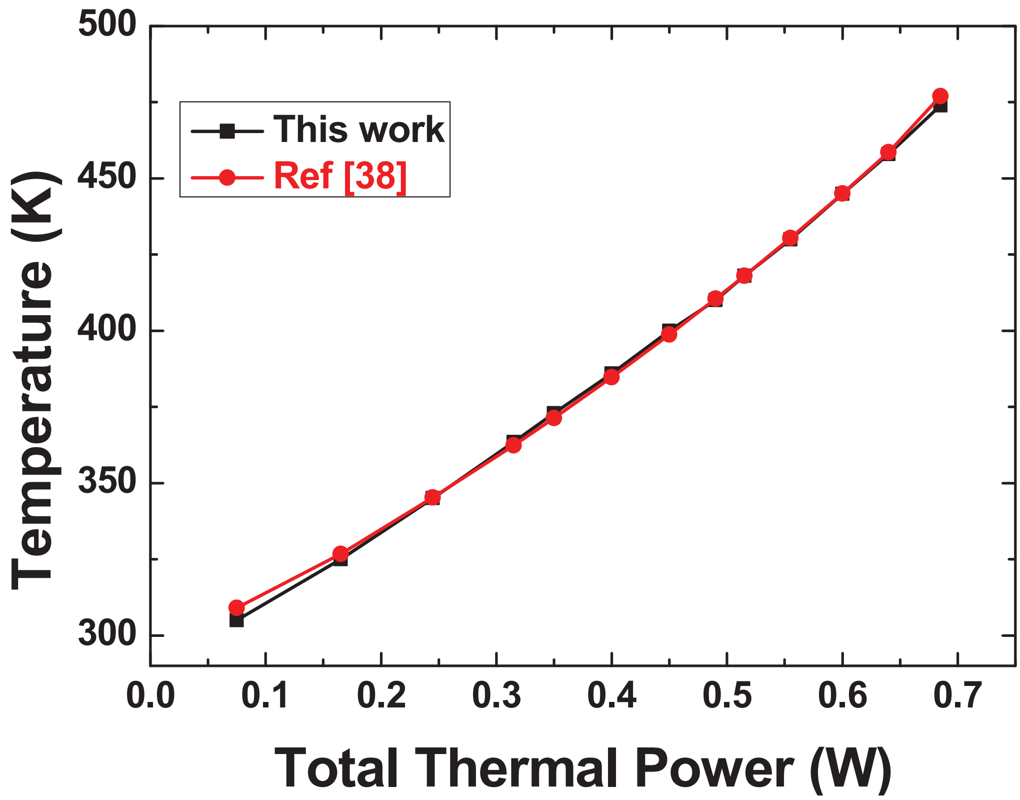

Figure 3.4 Comparison of simualted temperature between this work and the work of Zhi et al. [38].

[40]. In [38], the surface temperatures of the MUTC photodiodes were measured using a thermal-reflectance imaging method. Since the device structure in this work is the same as that in [38], the simulation parameters are based on the imaging results in [38]. Figure 3.4 shows the simulated temperature at different total thermal power in this work and [38]. We can see that the two simulation results are in good agreement.

In my work, the 50-µm devices on diamond submount failed at dissipated power of 2.5 W and the corresponding calculated failure temperature is 438 K. This point is illustrated in Figure 3.5, which shows the dissipated power versus junction temperature.

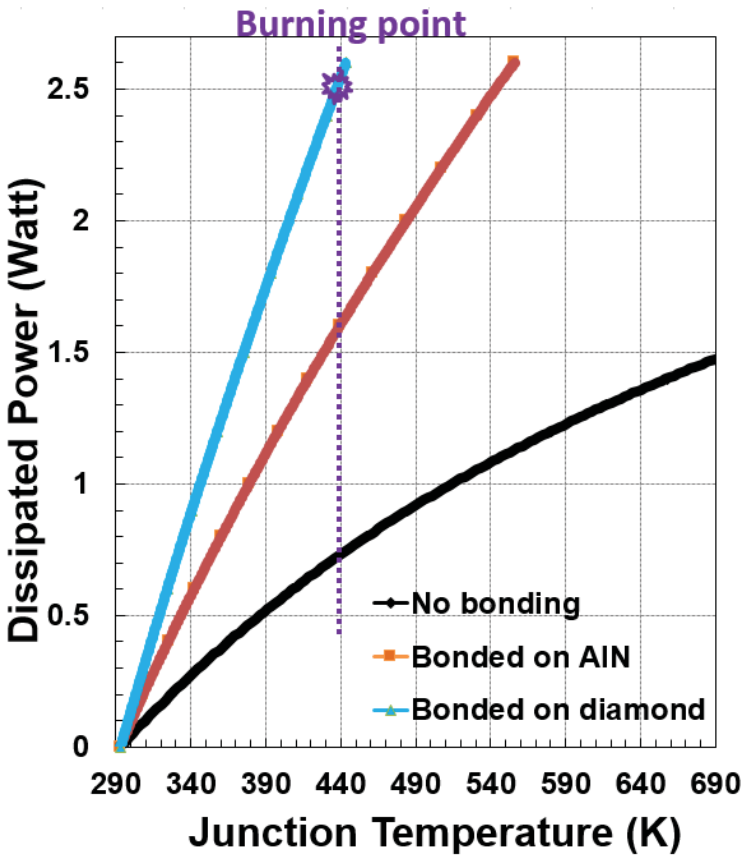

Figure 3.5 Junction temperature of the device at different dissipated powers.

For devices without a submount or with an AlN submount at the same failure temperature, the dissipated power is estimated to be 0.7 W and 1.6 W, respectively. Compared with a device without a submount and a device bonded on AlN the device flip-chip bonded to diamond is projected to dissipate power enhancement of ~250% and ~50 %, respectively, which agrees with experimental results. Figure 3.6 shows the simulated thermal profiles of these three device configurations at the same dissipated power of 1.5 W. The core temperatures of devices without a submount, with an AlN submount, and with a diamond submount are 701 K, 428 K and 375 K, respectively. It is clear that diamond effectively reduces the junction temperature.

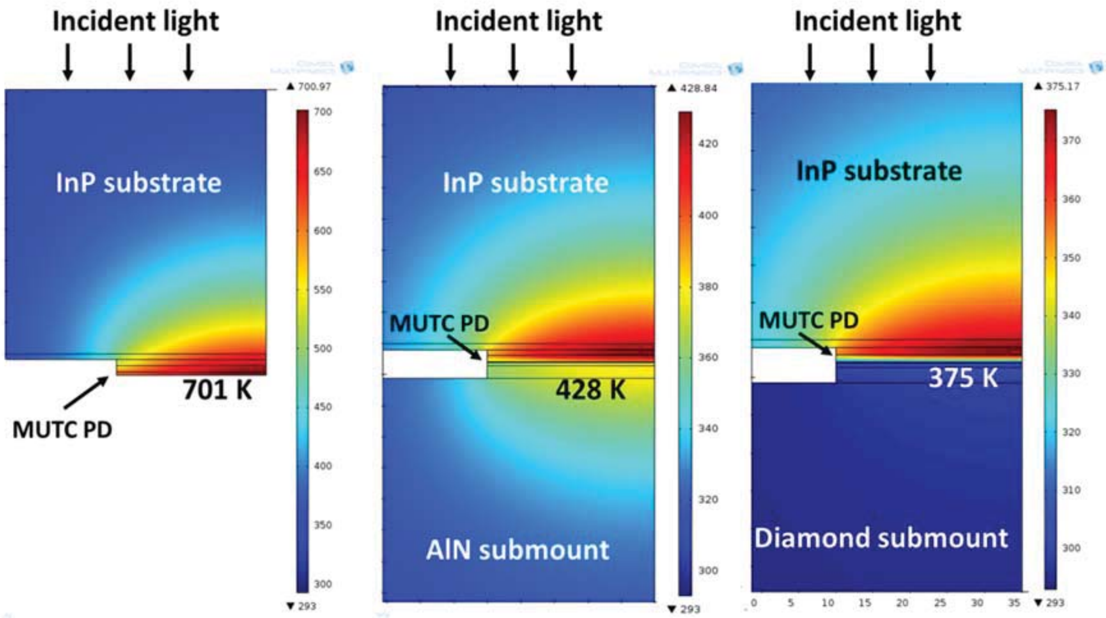

Figure 3.6 Junction temperature of the device at a fixed dissipated power of 1.5 W.

3.4 Experimental Results

As one of the most important figures of merit for photodiodes, the bandwidth characterizes the operational speed of a photodiode in terms of its frequency response. The 3-dB bandwidth is defined as the frequency at which the output RF power drops from its low-frequency value by 3 dB. This is illustrated in Figure 3.7 (a). Another two important figures of merit are saturation current and output power. Saturation current is defined as the average photocurrent at which the RF power falls below the peak output power by 1 dB. The corresponding RF power is the output power at 1 dB compression

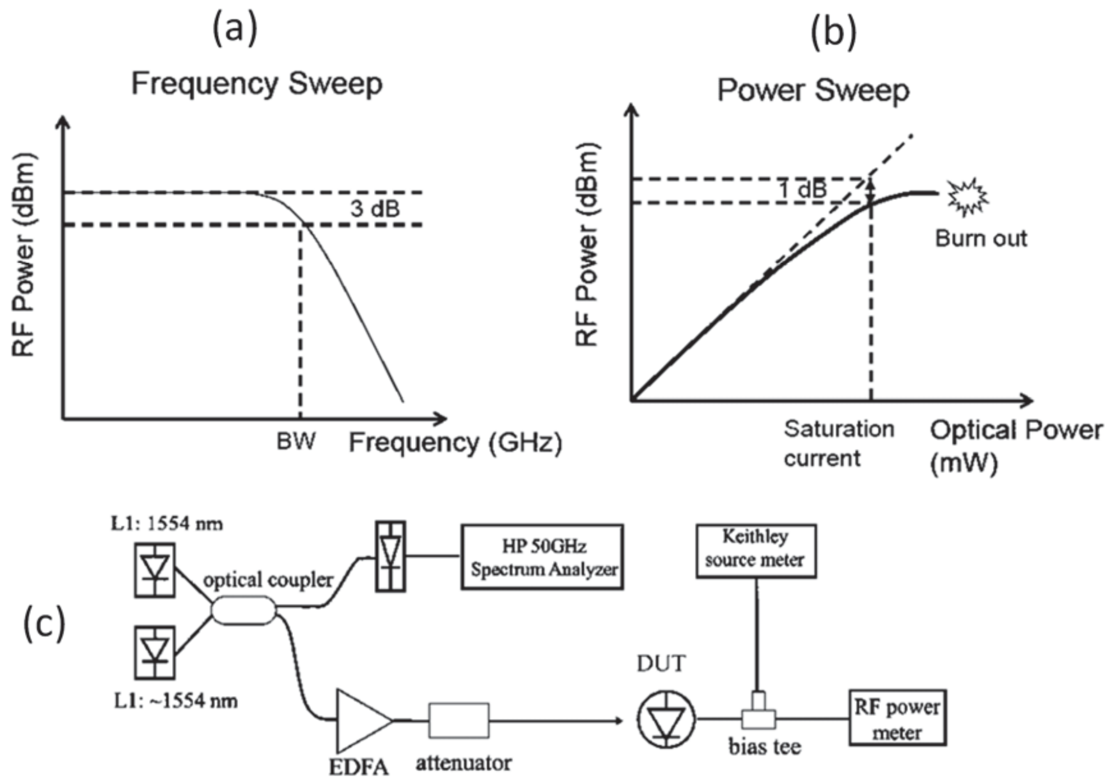

Figure 3.7 Schematic plots of (a) 3-dB bandwidth, (b) 1-dB power compression and (c) heterodyne measurement system.

point shown in Figure 3.7 (b). As illustrated in Figure 3.7 (c), an optical heterodyne setup was used to measure responsivity, bandwidth, and saturation characteristics. The modulation depth was close to 100%. The heterodyne measurement setup consists of one laser with fixed wavelength and another whose wavelength is tuned thermally. The frequency of the beat signal of two lasers is monitored by a commercial photodiode and an HP 50 GHz spectrum analyzer. Another branch of the optical coupler is connected to an EDFA in order to amplify the optical signal and then an optical attenuator is used to tune to input optical power on the devices. The bias voltage of the device is supplied by a Keithley source meter through a bias tee. The output RF power of the device is measured by a RF power meter. Figure 3.8 is a photograph of the device test platform. The devices

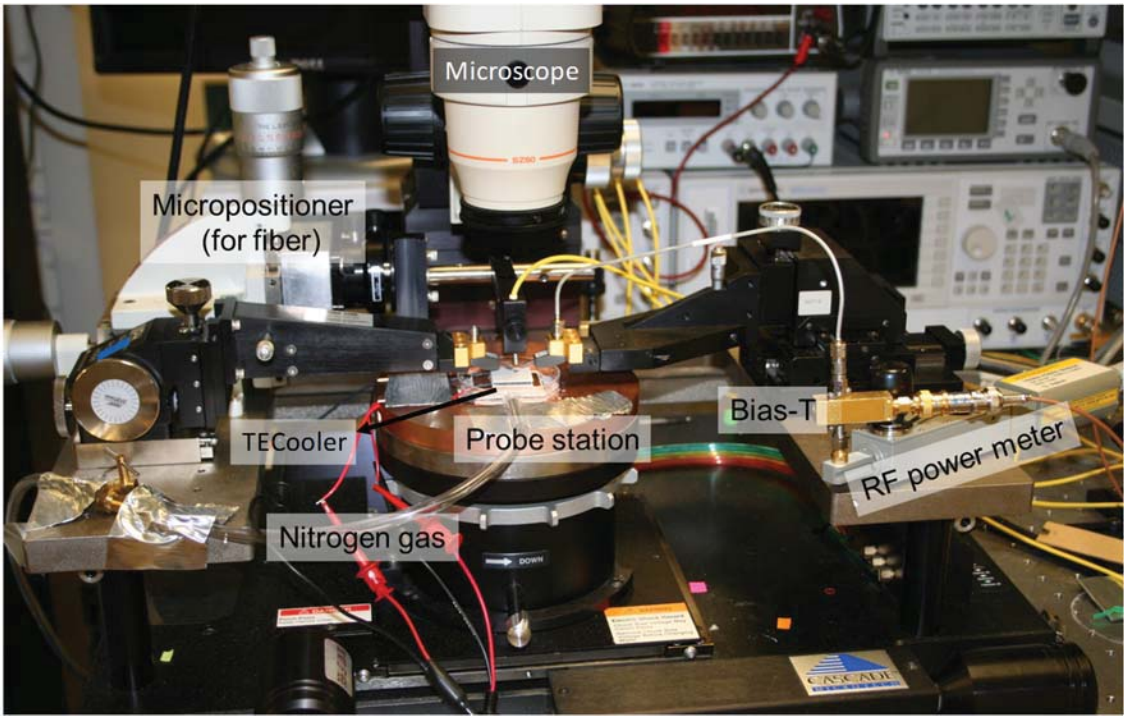

Figure 3.8 Device test platform including TECooler.

under test are placed on a thermo-electric cooler located on probe station. The photodiode output is monitored with an RF probe that is connected to a bias-tee. The thermo-electric cooler is used to control the device temperature. As the temperature of photodiode drops below zero degrees, water vapor freezes on the top surface of the photodiode. As a consequence, the input optical power is scattered by the ice crystals and responsivity degrades. In order to avoid this, nitrogen gas is used to remove the water vapor.

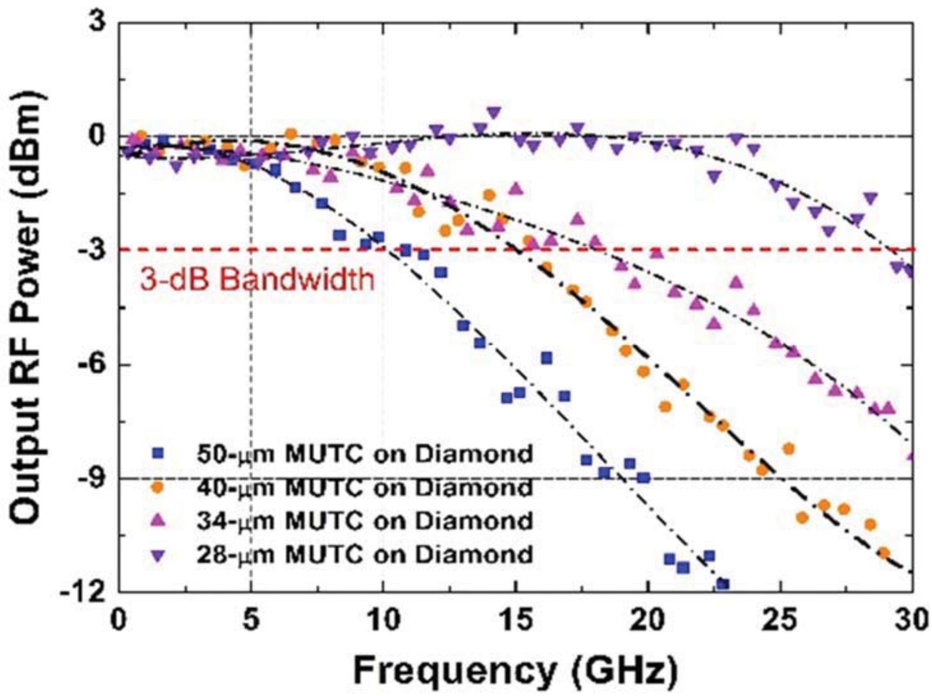

Figure 3.9 Frequency response for different PD diameters.

The measured responsivity and dark current at 10 V were 0.75 A/W and 500 nA, respectively. In the saturation measurement, the lensed fiber that illuminated the devices was pulled back to the position where the photocurrent dropped to half the peak photocurrent in order to maintain spatially uniform illumination. All devices under test were placed on a copper heat sink and the temperature was maintained at ~20 ºC. As shown in Figure 3.9, the 28-μm, 34-μm, 40-μm and 50-μm diameter photodiodes exhibit bandwidths of 28 GHz, 19 GHz, 15 GHz and 10 GHz with saturation currents of 128 mA, 167 mA, 234 mA and 300 mA, respectively. In Figure 3.10, I plot the output power versus photocurrent for different device diameters. The corresponding maximum RF output powers at 25 GHz, 20 GHz, 15 GHz, and 10 GHz are 26.2 dBm, 28.2 dBm, 29.6 dBm and

32. 7 dBm (1.86 W), respectively. The corresponding dissipated powers are 28.3 dBm, 30.4 dBm, 32.3 dBm and 34 dBm (2.5 W), respectively. As the photocurrent

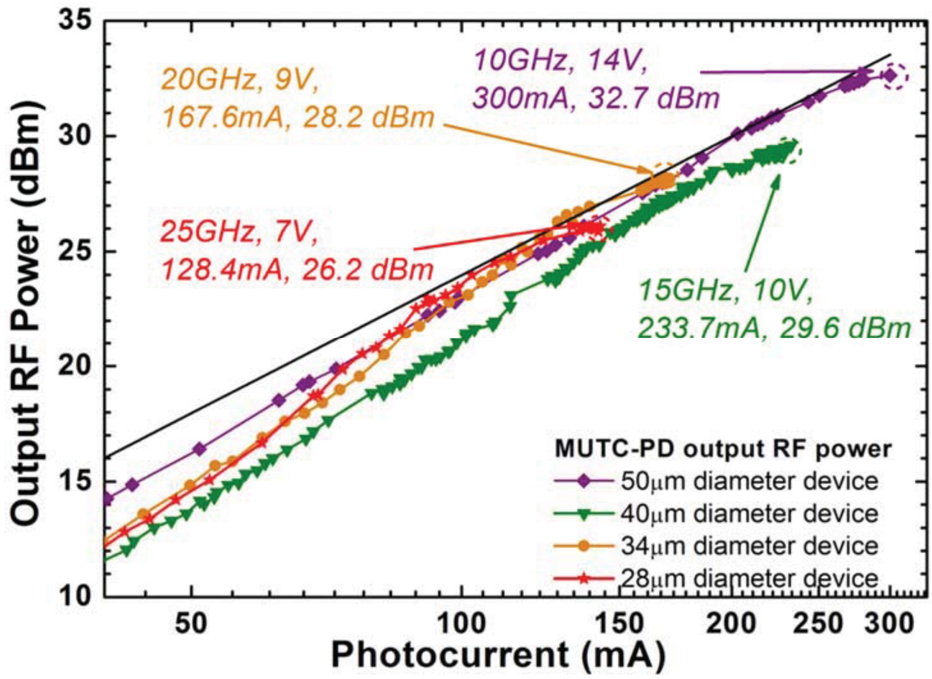

Figure 3.10 Output power versus photocurrent for different sizes devices. 26

increases, the output RF power approaches the ideal RF power. This is the well-known bandwidth enhancement that originates from the current-induced electric field in the graded absorption layer [30, 35]. A summary of RF output power versus frequency is plotted in Figure 3.11 [1, 34-36, 38, 40-57]. The output power of a 50 μm-diameter device on diamond submount at 10 GHz is 1.86 W (without active cooling) and that for a similar device on AlN at ~ -10 ºC is 1.0 W [1]. Relative to devices on AlN submounts, the diamond submount devices with diameters of 40 μm, 34 μm and 28 μm on diamond, the output RF powers improve 22.7 % at 15 GHz, 78.4% at 20 GHz and 35.5% at 25 GHz, respectively.

It should be noted that 1.5 W RF output power at 8 GHz was achieved by balanced photodiodes and active cooling [57]. In addition, these flip-chip bonded photodiodes exhibit larger failure power density. The failure power density, as defined by the product of the reverse bias and the DC current at thermal failure, of a 50-μm diameter photodiode on diamond submount increased by 300% and 50% compared with that of a photodiode without a submount and a photodiode flip-chip bonded to AlN, respectively.

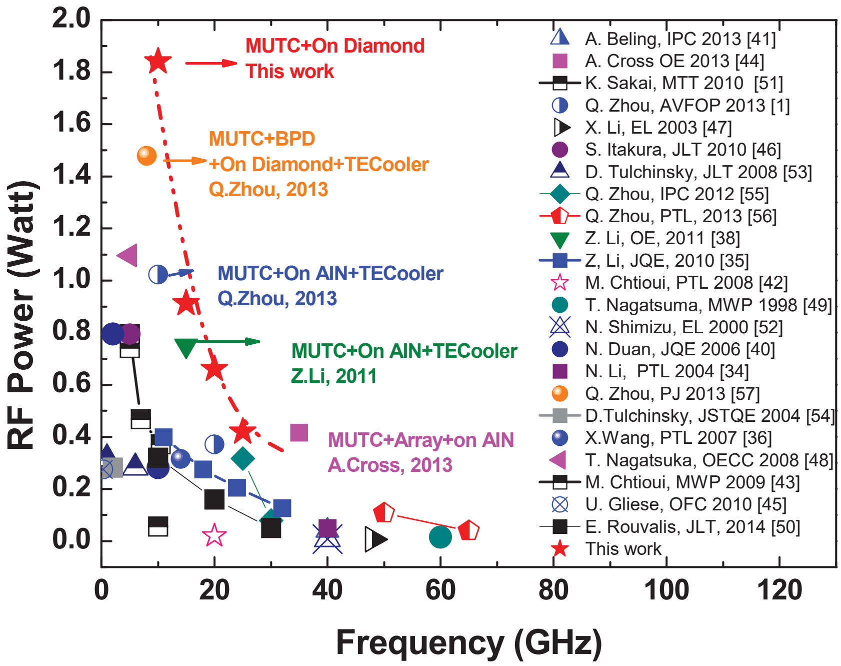

Figure 3.11 Summary of RF output power versus frequency.

3.5 Modulation-Depth Enhancement

Some of the design aspects of the CC-MUTC structure promote high power conversion efficiency. The combination of drift layer, cliff layer, and partially depleted absorption layer, help to maintain high electric field across the heterojunction interfaces,

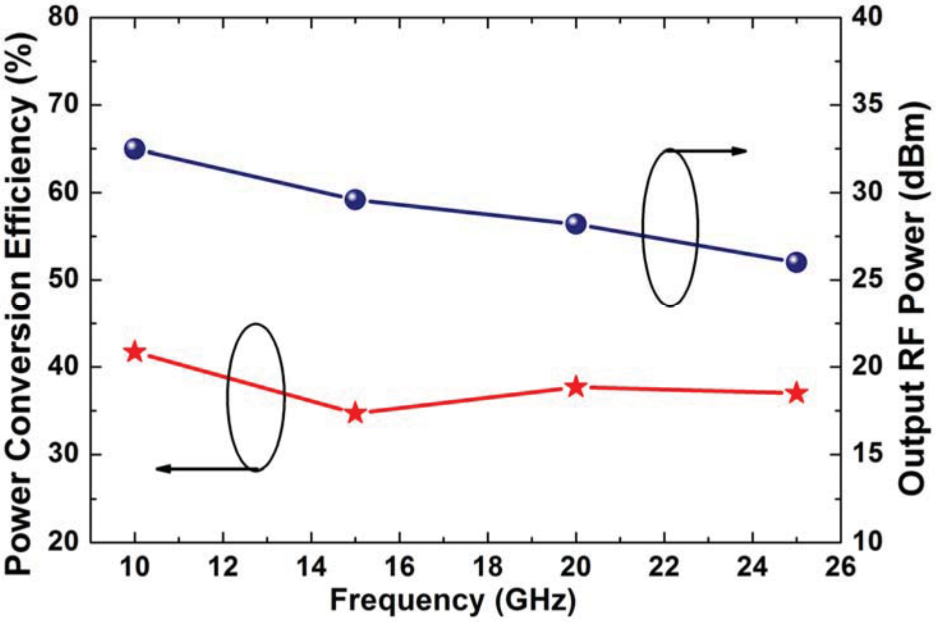

Figure 3.12 Power conversion efficiency of the photodiode driven by heterodyne setup.

which ultimately allows more of the electric power and input optical power to be converted to RF output power. The power conversion efficiency (PCE) of an ideal photodiode can be expressed as [45]

$$\eta_{\omega} = \frac{P_{rf,\omega}}{P_{PD,bias} + \left\langle P_{opt}(t) \right\rangle} = \frac{(m_{\omega} \cdot I_{ph})^2 R_{load} / 2}{m_{\omega} \cdot I_{ph}^2 R_{load} + I_{ph} / r} \tag{3.1}$$

where $P_{rf,\omega}$ is the average power of the fundamental RF signal at the load, $P_{PD,bias}$ is the electrical power delivered to the photodiode, $<P_{opt}(t)>$ is the input average optical power, m_{ω} is the modulation depth of the fundamental RF signal, and R_{load} is the load resistance. I_{ph}, V_{bias}, and r are the average photocurrent, bias voltage and responsivity of the photodiode, respectively. Eq. (3.1) illustrates the dependence of PCE on modulation depth. The maximum PCE is $m_{\omega}/2$ when I_{ph}

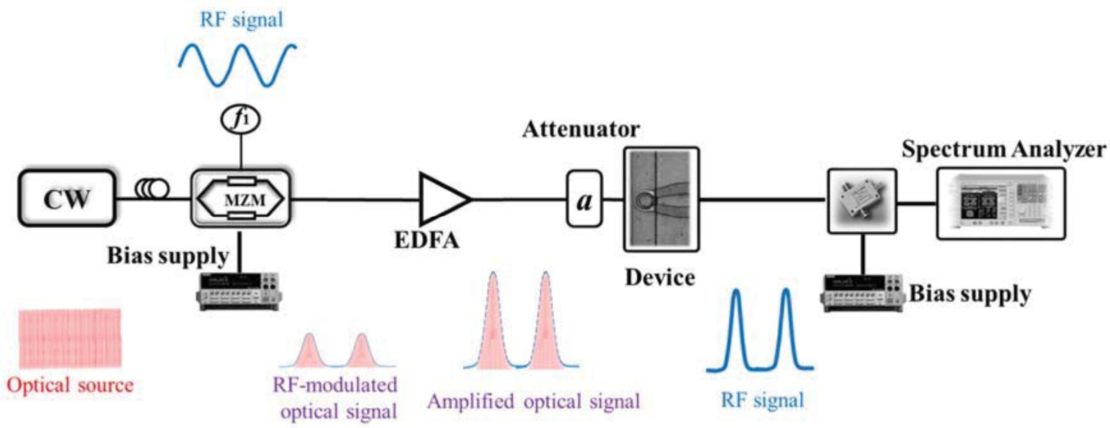

Figure 3.13 Experimental setup for the modulation-depth-enhancement technique.

approaches infinity. For the optical heterodyne setup used in this work, the photodiode was driven by a sinusoidal optical intensity-envelope with maximum modulation depth of 100%, which would indicate that PCE should approach 50 % at high photocurrent [45, 58]. This agrees with classic class A operation of electronic transistor amplifiers. In our experiment, the PCE for the sinusoidal optical intensity envelope was determined from the saturation characteristics. Figure 3.12 show the PCE versus frequency for heterodyne modulation. The PCE is 42 %, 37.7% and 37 % at 10 GHz, 20 GHz, 25 GHz, respectively, which compares favorably with the published results at the corresponding frequencies.

However, the effective modulation depth of the input optical signal of the photodiode can be enhanced using a Mach–Zehnder modulator by adjusting the bias point of the modulator and the power of the input RF signal delivered to the modulator. Figure 3.13 shows a block diagram of the setup. The signals are plotted in time domain. The modulation depth of the input optical signal can be expressed as

$$m_{\omega} = 2\sin(\beta V_{dc})J_1(\beta V_{ac})\big/\left[1+\cos(\beta V_{dc})J_0(\beta V_{ac})\right] \tag{3.2}$$

where $\beta=\pi/V_\pi$, and V_π, V_{dc} and V_{ac} are the halfwave voltage, bias voltage, and RF signal voltage of the modulator, respectively. As the modulator is biased away from the quadrature point toward its null point (βV_{dc}: $\pi/2 \rightarrow \pi$), the modulation depth will initially increase, peak at a specific bias point, and finally decrease rapidly. This is illustrated in the inset of Figure 3.14. The maximum m_ω is 1.414 when βV_{dc} = 3.12 (close to the null bias point) and βV_{ac} = 0.0314 (small input RF signal). The maximum theoretical PCE for the modulation-depth-enhancement technique is ~ 70%. Note that we can also explain the modulation-depth-enhancement and high PCE based on changes in the output waveform. When the modulator is biased at the quadrature point, the input RF signal to the modulator can go through the modulator and the photodiode, where the photodiode works at class A condition. When the modulator is biased toward its null point, a part of the optical envelope (corresponding with the input RF signal of the modulator) will be cut-off and, at this point, the photodiode works in the class AB mode. When the operation condition of a transistor changes from class A to class AB, the PCE will increase correspondingly. The amplitude of the fundamental signal will initially increase and then drop after a specific point. The DC component will decrease faster than the fundamental signal [58]. In other words, the modulation depth is enhanced when the operating condition changes from class A to class AB. PCE versus average photocurrent is plotted in Figure 3.15. Class A operation is denoted by the orange dashed line. The blue dashed line in Figure 3.15 illustrates the relationship between class AB PCE and average photocurrent. By optimizing the bias voltage of the modulator ($\beta V_{dc} \approx 3.1$) and the RF

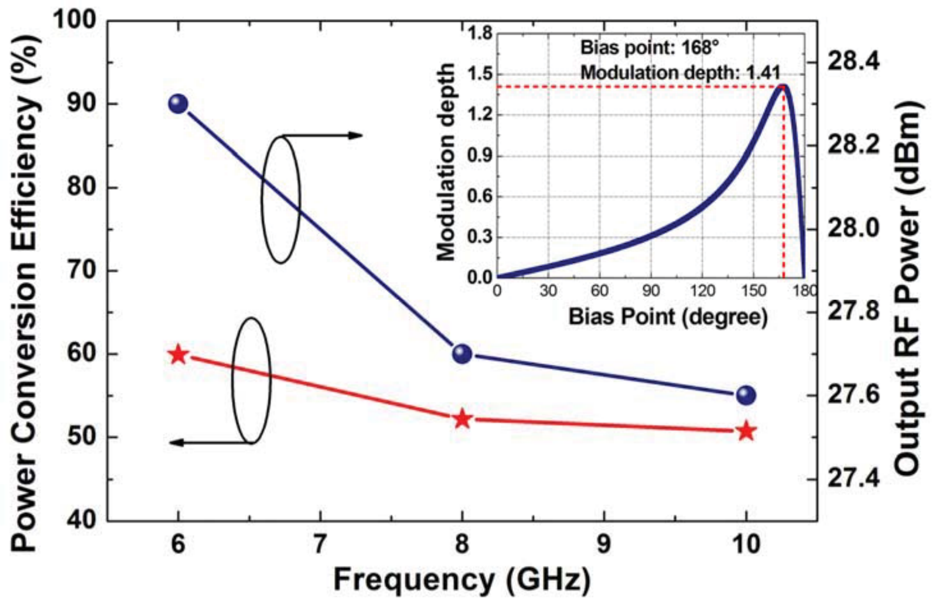

Figure 3.14 Power conversion efficiency of the photodiode driven by modulator setup.

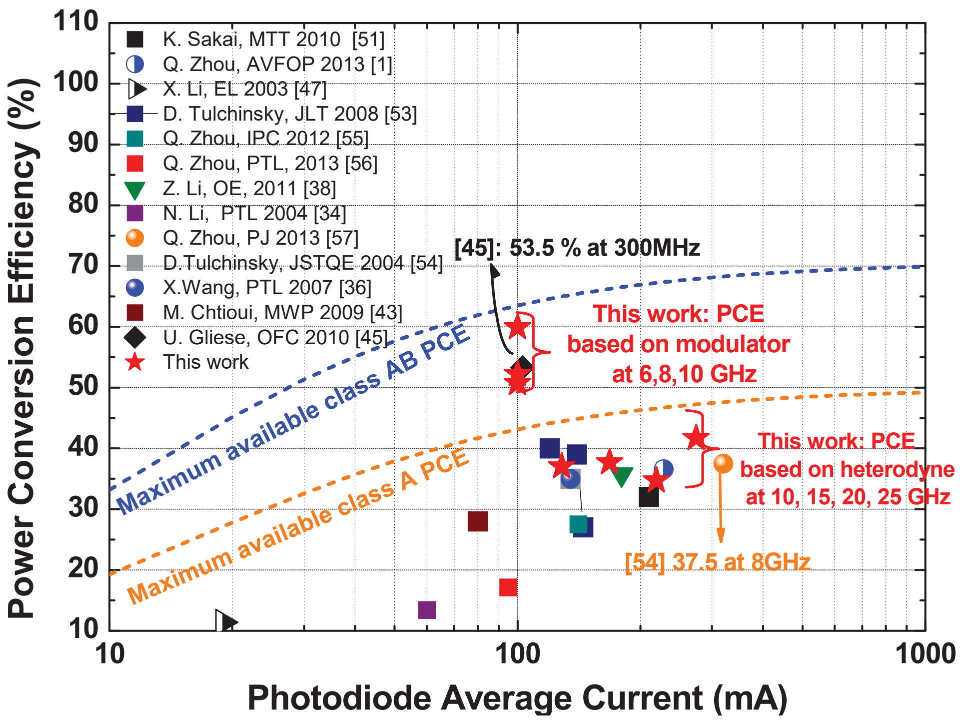

Figure 3.15 Summary of power conversion efficiency versus average photocurrent.

signal voltage (βV_{ac} = 0.0314), 60 %, 52 % and 51 % power conversion efficiency with 28.3 dBm, 27.7 dBm and 27.6 dBm RF output power at 6 GHz, 8 GHz, and 10 GHz, respectively, has been achieved (Figure 3.14). This approaches the class AB PCE limit based on the optoelectronic modulator (63.5 % at 100 mA), which is plotted as the blue dashed line Figure 3.15.

3.6 Summary

In this chapter, 1.8 W output power at 10 GHz and 60 % power conversion efficiency at 6 GHz with a flip-chip-bonded-on-diamond photodiode chip without active cooling has been achieved. These CC-MUTC photodiodes achieved RF output powers of 29.6 dBm, 28.2 dBm and 26.2 dBm at 15 GHz, 20 GHz and 25 GHz, respectively. The failure power density on diamond submount was 300 % and 50% higher than that of photodiodes without flip-chip bonding and bonded to an AlN submount, respectively. Based on the high power and high frequency MUTC photodiode on diamond submount and modulation-depth-enhancement technique, power conversion efficiencies of 51% ~ 60% at 6 ~ 10 GHz with ~ 27.8 dBm RF output power was achieved.

Chapter 4 High-performance analog photonic link

4.1 Introduction

In recent years, analog photonic links have demonstrated the potential to improve the performance of broadband wireless access networks, cable television signal distribution networks, and remote microwave antenna systems owing to their large instantaneous bandwidth, the low attenuation of optical fibers, continuous spectral coverage, enhanced signal processing capabilities, as well as size, weight, and power consumption benefits [8].

To date, four approaches have been successfully employed to achieve high performance analog optical links: resonant impedance matching, noise reduction, linearization techniques, and development of high-performance components. By using a resonant impedance matching technique, low noise figure can be achieved. However, this is restricted to narrow bands at low frequency [59]. For the noise reduction method, low bias modulation [60-62] and balance detection [60, 63-65] are used to reduce the relative intensity noise (RIN) from the laser in order to improve the noise figure and dynamic range of the link. In [60], this approach achieved record noise figure and gain in the 6 – 12 GHz band by using low bias modulation and high-optical-power modulator. However, in practice, the high-optical-power modulator tends to exhibit brief duration (less than one minute), significant bias drift and insertion loss. Balanced detection can reduce the common-mode noise effective but it relies on precise matching of the photodiodes and the bandwidth is limited by the higher effective capacitance of diodes in parallel. Another approach is to suppress the nonlinearity of the modulator and photodiode by different linearization schemes, which include electrical pre-distortion [66], cascaded or parallel Mach-Zehnder modulators (MZM) [67, 68], and post digital signal compensation [69, 70]. Although this method can effectively improve the dynamic range of the link, the gain and noise figure may be degraded due to the larger loss from additional components or operations. Finally, high-performance links can be achieved using components whose characteristics are optimized for this application, namely, high-power and low-noise lasers [71, 72], highly linear modulators that operate at high input power with high conversion efficiency [60, 73, 74], and high-power and high-linearity photodiodes [42, 50, 72, 75]. In order to design an analog photonic link with low noise figure, high gain, and high dynamic range without electronic amplification, we focused our effort on external intensity modulation, which exhibits higher modulation efficiency and greater SNR than direct modulation [60].

4.2 Characterization of analog photonic link

In this section we describe characterization of three link figures of merit: 1) gain; 2) noise figure; and 3) spur-free dynamic range (SFDR).

4.2.1 Gain

Gain is a key parameter in the design of an analog photonic link in that it is strongly linked to the other performance figures-of-merit. We define gain as the ratio of output RF signal power from the photodiode to input RF signal power to the modulator. The small-signal RF gain g_l can be expressed as [76]

$$
\begin{aligned}
g_l &= s_m^2 \cdot g_{EDFA}^2 \cdot r_p^2 \\
s_m &= \pi P_i T_{ff} R_{load} \sin(\beta V_{dc}) \big/ (2V_\pi)
\end{aligned}
\tag{4.1}
$$

where s_m is the modulation sensitivity and P_i, T_{ff}, V_π and V_{dc} are the input optical power, transmission, halfwave voltage, and bias voltage of the modulator, respectively. β is the modulation index ($\beta=\pi/V_\pi$) and R_{load} is the terminating resistance of the modulator. g_{EDFA} is the optical gain of the EDFA and r_p is the responsivity of the photodiode. Equation (4.1) illustrates the dependence of the gain on the output optical power of the laser, the optical power capacity and halfwave voltage of the modulator, the bias point of the modulator, the gain and maximum output optical power of the EDFA, and the responsivity and RF power characteristics of the photodiode.

4.2.2 Noise Figure

Noise figure is defined as the signal-to-noise ratio relative to input thermal noise at 290 K [76] and it can be expressed as

$$
NF = 10\log\left[N_{out} \big/ \left(g_l N_{th}\right)\right] \tag{4.2}
$$

where $N_{th}=kT_0B$ is the input thermal noise, k is Boltzmann's constant, T_0 = 290 K and B is the resolution bandwidth. g_l is the gain of the link. N_{out} is the total noise at the output of the photodiode, which includes the amplified thermal noise, thermal noise from the photodiode, photodiode shot noise, relative intensity noise (RIN) from optical source and excess noise from EDFA (N_{EDFA}). After evaluating these noise components and substituting Eq. (4.1) into Eq. (4.2), the noise figure of the link can be expressed as [9]:

$$NF = 10\log\left\{\begin{array}{l} 1+\dfrac{1}{g_l}+\dfrac{4qV_\pi^2\left[1+\cos\left(\beta V_{dc}\right)\right]}{kT_0\pi^2 P_i T_{ff} r_p g_{EDFA} R_{load}\sin^2\left(\beta V_{dc}\right)} \\ +\dfrac{V_\pi^2\left[1+\cos\left(\beta V_{dc}\right)\right]^2 10^{RIN/10}}{kT_0\pi^2\sin^2\left(\beta V_{dc}\right)R_{load}} \\ +\dfrac{N_{EDFA}}{kT_0 s_m^2 r_d^2 g_{EDFA}^2} \end{array}\right\} \tag{4.3}$$

The first and the second terms in the bracket represent the total thermal noise including amplified input thermal noise and the thermal noise generated in the photodiode. The third term is the contribution of shot noise to the noise figure. It can be seen that the optical gain of an EDFA can effectively reduce the shot noise component of the noise figure. The laser relative intensity noise (RIN) is the fourth contributor to the noise figure. The optical gain of an EDFA has no effect on this term. Note that both the shot-noise-induced and RIN-induced noise figure components can be reduced by the low-bias technique [76]. The last term is the contribution of excess noise from the EDFA. In our experiment, the output power of the EDFA was dominated by optically amplified input power. A narrow bandwidth optical filter was applied to suppress the spontaneous emission noise of the EDFA. Therefore the primary excess noise from the EDFA was the signal-spontaneous noise [9].

4.2.3 Dynamic Range

Another important performance parameter is the third-order two-tone SFDR, which is defined as the SNR of the fundamental signal with frequencies f_1 and f_2 at the output of the photodiode when the power of the third intermodulation distortion (IMD3) signal with frequencies of $2f_1$-f_2 and $2f_2$-f_1 is equal to the output noise. The IMD3 signal is important because it occurs within the bandwidth of the narrow electrical filter in a suboctave system. Note that the low-bias modulation scheme will lead to large second-order distortion. Therefore, we only consider a suboctave link.

The SFDR depends on the nonlinearity of the optoelectronic components, the output noise, and the gain. The relation between SFDR and the other parameters is illustrated by the following equation:

$$SFDR = \left(\frac{OIP3}{N_{out}} \right)^{2/3} \tag{4.4}$$

where $OIP3$ is the third–order intercept point and N_{out} is the output noise. By calculating the input RF signal power at which the output power of the fundamental signal is equal to the IMD3 signal, $OIP3$ is given by the following expression [9]:

$$OIP3 = g_l \cdot IIP3 = \frac{4 g_l V_\pi^2}{\pi^2 R_{load}} . \tag{4.5}$$

where g_l is the gain, $IIP3$ is the input third-order intercept point. From Eq. 4.5 and Eq. 4.1, it can be seen that $OIP3$ depends on the bias point of the modulator and the gain of the EDFA. Note Eq. (4.5) ignores the nonlinearity of the photodiode.

4.3 Devices Performance

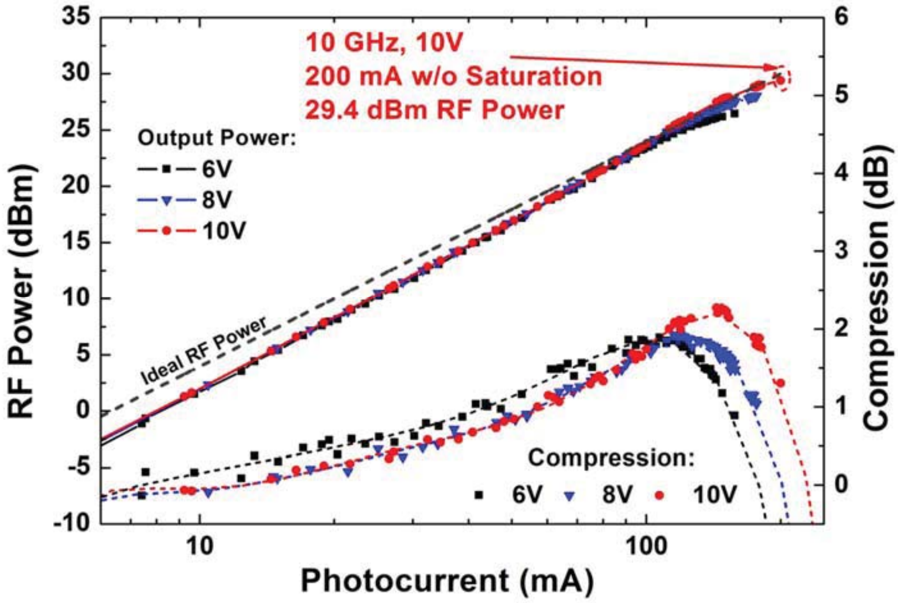

Figure 4.1 Saturation current of CC-MUTC PDs measured at different bias voltages.

As stated above, the analog link reported here utilizes a CC-MUTC photodiode. A cross-section of the photodiode is shown in Table 3.1 and a more detailed description can be found in [35]. When the photodiode operates at high current and high bias voltage, Joule heating will result in thermal failure. Some thermal management schemes have been proposed and good results have been reported [38, 40, 55, 56, 77]. For this work, the photodiode chips are flip-chip-bonded by thermo-compression Au-Au bonds to an aluminum nitride (AlN) submount with tapered 50 Ω coplanar waveguides (CPWs).

An optical heterodyne setup with an optical modulation depth close to 100% was used to characterize the saturation current and the bandwidth. A 40-µm device exhibits a saturation current of 157 mA, 177 mA and 200 mA, and RF output power of 26.4 dBm, 28 dBm and 29.4 dBm at -6, -8 and -10 V bias, respectively. The corresponding optical input powers were 26.7 dBm, 27.2 dBm and 27.1 dBm. In Figure 4.1 the RF output power and compression are plotted versus photocurrent. The RF power approaches the ideal output power as the photocurrent increases. This is due to current-induced bandwidth enhancement [30, 35] that can be observed clearly in Figure 4.2, which shows the RF response for different photocurrent.

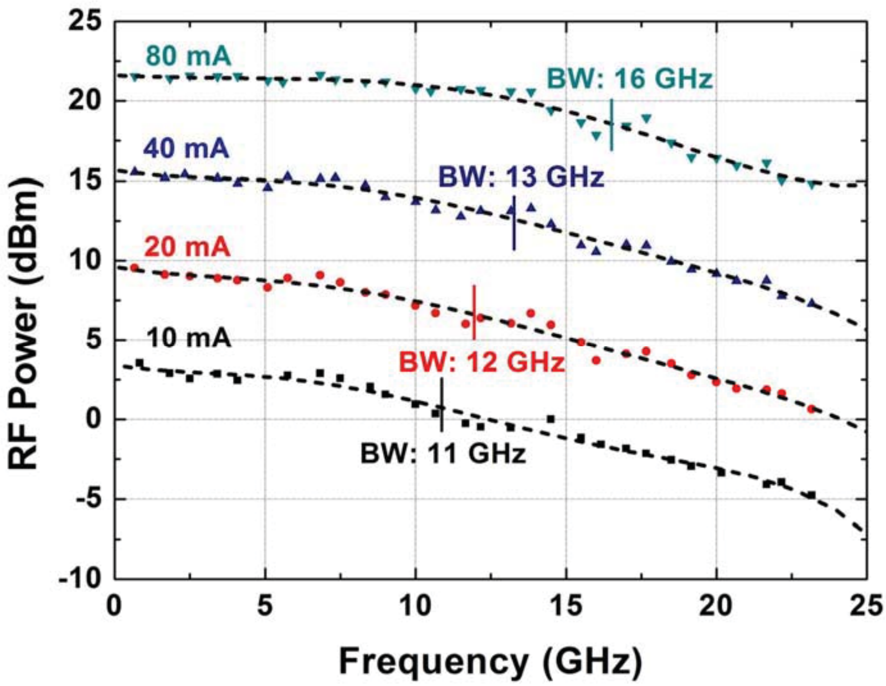

Figure 4.2 Frequency responses of the flip-chip-bond PD at different photocurrent.

In addition to high saturation current and high RF output power, high responsivity and high bandwidth are important for an analog link. However, it is well known that there is a tradeoff between responsivity and bandwidth. Since this is an X-band link, the optimum thickness of the undepleted absorber layer is ~700 µm. As shown in Figure 4.2 a 40-µm device exhibits 11 GHz bandwidth at 10 mA and 16 GHz bandwidth at 80 mA.

*OIP*3 was measured using a three-tone measurement technique, which is immune to the nonlinearity of the modulator [78]. The *OIP*3 at 10 GHz was measured as a function of photocurrent at -6 V and -10 V and 80% modulation depth. Figure 4.3 shows *OIP*3 versus photocurrent. At -6 V *OIP*3 is above 35 dBm and at -10 V *OIP*3 is > 40 dBm. The variation of *OIP*3 with photocurrent and bias voltage originates from the dependence of responsivity and capacitance on bias voltage and current [79].

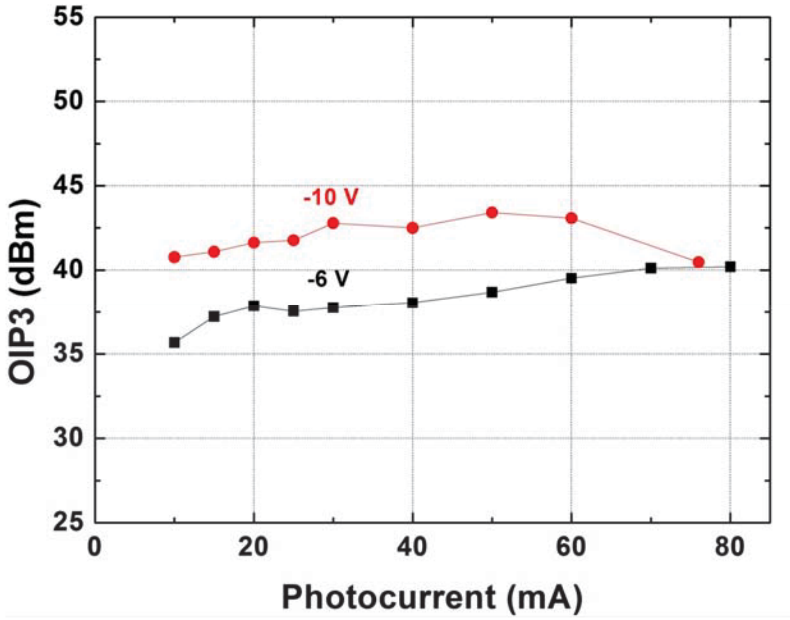

Figure 4.3 Photodiode *OIP*3 at 10 GHz at -6 V and -10V bias voltage.

4.4 Link configuration and experimental results

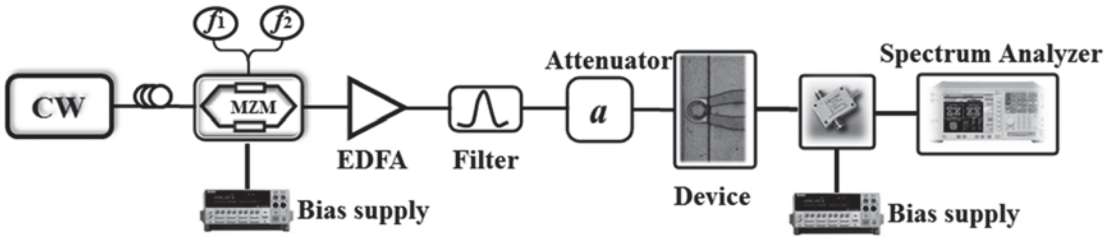

Figure 4.4 Experimental setup for analog photonic link.

A block *diagram* of the analog optic link is shown in Figure 4.4. The optical source is an Orbits Lightwave OEM High Power SlowLight™ Laser. The maximum output power of the laser is 23 dBm and its RIN is -165 dBc/Hz. Continuous wave (CW) light is coupled into an intensity modulator (JDSU APE™ Microwave Analog Modulator) with V_π of 9 V, 20 GHz bandwidth, and ~3 dB insertion loss Two RF signal sources are combined into a two-tone signal by a 3-dB RF coupler. The modulator is operated at low bias since the link achieves maximum signal-to-noise ratio (SNR) as the bias point moves from quadrature toward the null point [60]. The output optical power of the modulator can be expressed as:

$$P_{out} \propto \underbrace{\left[1+\cos(\beta V_{dc})\right]}_{dc} - \underbrace{\sin(\beta V_{dc})\sin(\beta V_{ac})}_{ac}. \tag{4.6}$$

The dc optical power and ac optical power decrease as the modulator is biased away from quadrature toward its null point (βV_{dc}: $\pi/2 \rightarrow \pi$) but the dc optical power decreases faster than the ac optical power. As a result, the shot noise generated in the photodiode, which is proportional to the average optical power [1 + cos (βV_{dc})], will decrease faster than the RF power of the photodiode. Further, the noise from the laser RIN is proportional to the square of average optical power $[1 + \cos(\beta V_{dc})]^2$. Therefore the RIN will decrease even faster than the decrease of shot noise. As a result, the SNR will increase as the bias moves toward the null point. However, at some bias point, the magnitude of the shot noise and RIN noise will be smaller than the thermal noise from the photodetector load resistor, which means that further increasing the bias point will degrade the SNR.

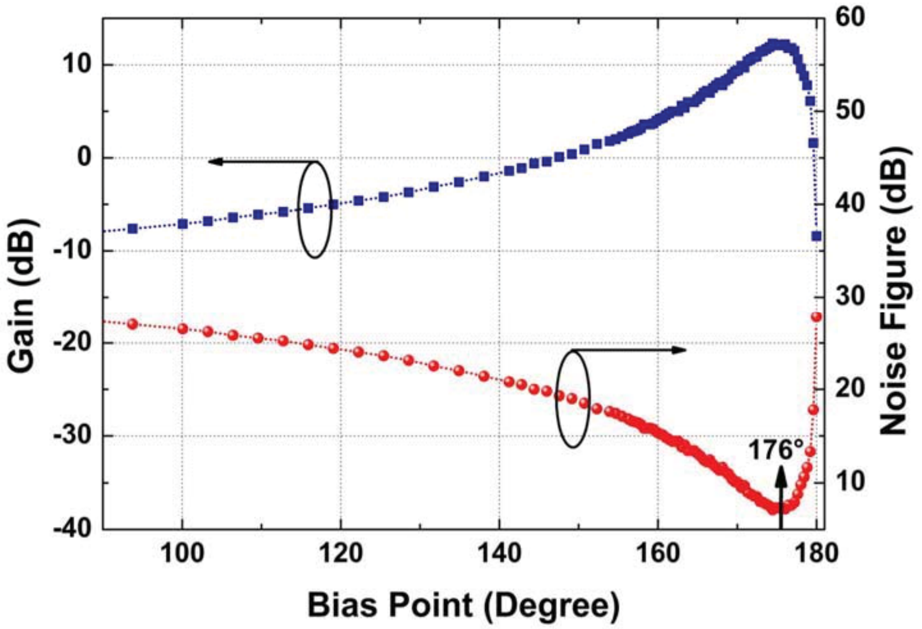

Figure 4.5 Gain and noise figure at 1 GHz and 10 mA photocurrent.

In order to demonstrate this, the gain and noise figure were measured at different bias points using a Mini-MBC-3 bias controller from YY Labs Inc. The results are plotted in Figure 4.5. The power and frequency of the input RF signal are -5 dBm and 1 GHz, respectively. The photocurrent at different modulator bias points was fixed at 10 mA. For these conditions the shot noise and RIN noise dominate. Therefore, for every modulator bias point, the noise powers are almost the same. From Figure 4.5, we note that the gain increases and noise figure decreases as the modulator bias point moves toward 176º. When the bias point is set closer to the null point, the gain and noise figure degrade quickly, i.e., the SNR increases at the beginning, peaks, and then degrades rapidly, which is consistent with the discussion above.

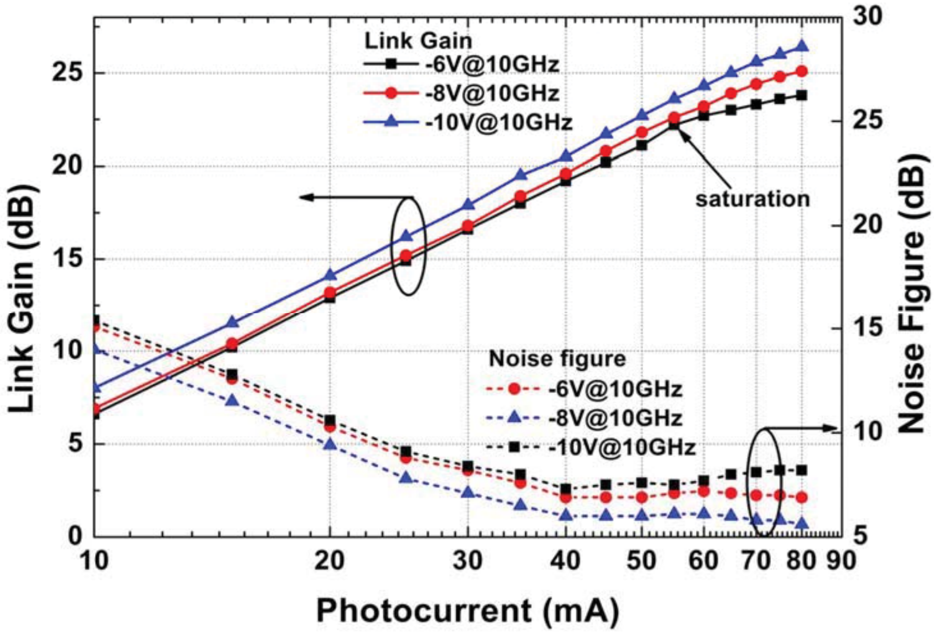

Figure 4.6 Gain and noise figure at 10 GHz for different PD's bias voltages and different photocurrents.

The low-bias modulation technique improves the SNR at the cost of low input optical power. In order to compensate the optical loss from the modulator, an EDFA with maximum output power of 33 dBm and noise figure of 4.8 dB is used to provide >26 dBm optical power to the photodiode in order to achieve high RF output power. A narrow bandwidth optical filter (3-dB bandwidth: 1 nm) is used to minimize the excess noise of the EDFA. The calculated RIN for the laser-EDFA combination is -164 dB/Hz (the laser RIN is -165 dB/Hz). Following the EDFA, an optical attenuator regulates the optical power input to the photodiode. The output noise power spectral density is measured with a spectrum analyzer (Agilent E4440A PSA). By measuring the gain and the link noise, the link NF is determined by the direct noise measurement method described in [80].

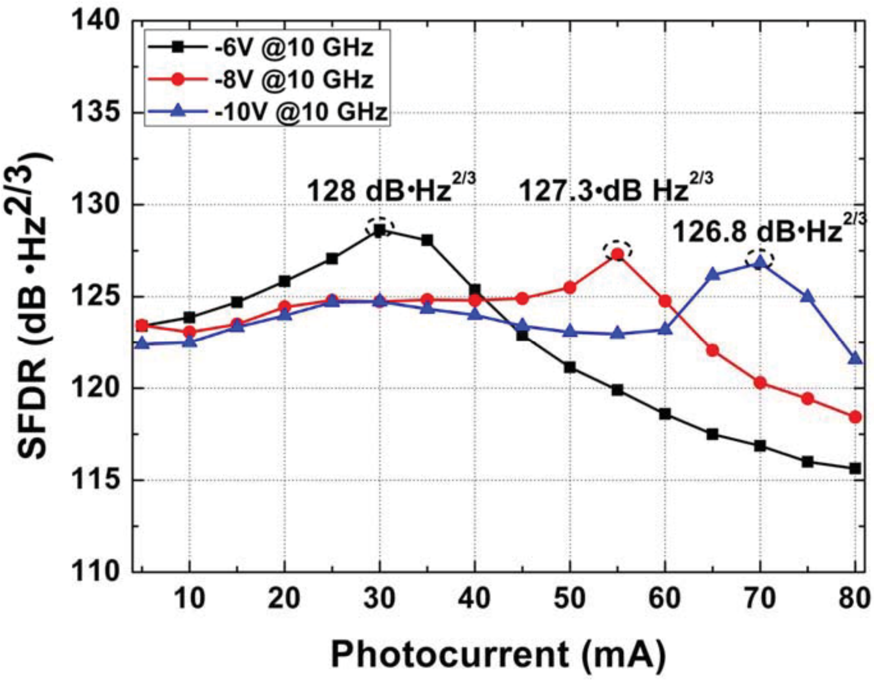

Figure 4.7 Link SFDR at 10 GHz for different PD's bias voltages and different photocurrents.

The link performance was characterized in the frequency range 6-12 GHz by changing the optical power input to the photodiode. The modulator bias point was adjusted to optimize the gain and noise figure. The gain and noise figure at 10 GHz are shown in

Figure 4.6. For –6 V bias, the gain increases with increasing photocurrent, and then saturates (~ 55 mA). Higher saturation current (70 mA) is observed at -8 V bias. The gain at -10 V bias increases linearly with photocurrent. The higher gain at larger bias voltage is consistent with the photodiode characteristics in Figure 4.1. The photodiode with larger bias voltage can operate at larger optical power and output more RF power. Note the photocurrent where the gain begins to saturate is lower than the saturation currents in Figure 4.1 since the modulation depth in the link measurement is larger than that used for the photodiode saturation/bandwidth measurement. At -6 V bias the noise figure decreases as the photocurrent increases from 10 mA to 40 mA. For photocurrent greater than 40 mA the increase in the noise figure is incremental owing to saturation at high photocurrent. When the bias voltage is -10 V, at 10 GHz and 80 mA the noise figure is 5.6 dB, the gain is 26.4 dB and the SFDR is 122 dB·Hz$^{2/3}$. Note that the input RF signal power is 0 dBm and the output RF power reaches 26.4 dBm at 80 mA photocurrent. For the 10-GHz link, the maximum SFDRs are 128 dB·Hz$^{2/3}$, 127.3 dB·Hz$^{2/3}$ and 126.8 dB·Hz$^{2/3}$ at -6 V, -8 V and -10 V bias, respectively. The SFDR changes with photocurrent (Figure 4.7) and bias voltage, which results from the photocurrent-dependent gain and noise figure. In addition, both bias voltage and photocurrent influence the nonlinearity of the photodiode [81].

4.5 Summary

In this chaprter an analog fiber optic link that uses a high-power and high-linearity CC-MUTC photodiode is discussed. The applied photodiode had 16 GHz bandwidth, high photocurrent (200 mA), and high output RF power (29.4 dBm). The *OIP*3 of the device was above 35 dBm. The analog fiber optic link achieved >24.5 dB gain, < 6.9 dB noise figure and >120 dB·Hz$^{2/3}$ across 6-12 GHz. At 6 GHz, of the gain was 27.8 dB. The SFDR of the link at 6 GHz was 120 dB·Hz$^{2/3}$.

Chapter 5 Photonic generation of high-power pulsed RF signals

5.1 Introduction

Photonic generation of microwave signals has demonstrated the potential for improved performance in applications such as satellite communications, wireless communications and optically controlled phased array antennas [82]. Previous approaches to generate continuous-wave microwave signals include heterodyned lasers [83-87], external modulation [88, 89], and optical frequency division [10]. It is also desirable to generate pulsed RF signals for radar and wireless applications. Various photonic techniques to generate pulsed RF signals have been reported including a photonic microwave filter [90], phase modulation [91], polarization modulation [92] and a mode-locked laser with an optical filter [93]. For these applications, the generation of high-power CW RF signals and high-power pulsed RF signals is important. Previously, we have shown that high-power MUTC photodiodes enabled photonic generation of high-power CW RF signals; in [77], a 10 GHz microwave signal with power up to 1.8 W was achieved [Chapter 3 of this dissertation] and in [10] the generation of a low-phase-noise microwave signal was demonstrated. In this chapter, we describe optical generation of high-power pulsed microwave signals using the CC-MUTC photodiodes described in the preceding chapters.

5.2 Devices Performance

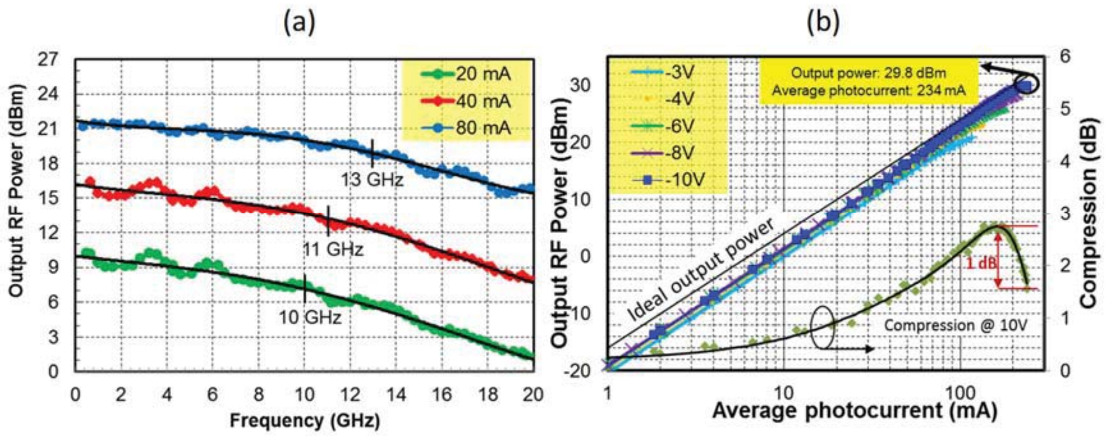

Figure 5.1. (a) Frequency response of a 40 µm-diameter photodiode at -6 V bias voltage. (b) RF output power for 15 GHz CW RF input signal versus average photocurrent at different reverse bias voltages.

The following describes the cw characteristics of the photodiodes used in this study. The structure is the same as that of the photodiodes described in Chapter 3. Typically the dark current and responsivity were 50 nA at -6 V bias voltage and 0.7 A/W, respectively. As shown in Figure 5.1 (a), 40-µm diameter photodiodes exhibited 13 GHz bandwidth at -6 V bias and 80 mA photocurrent. Figure 5.1 (b) shows the saturation and compression characteristics at 15 GHz. The output RF power exhibited a super-linear increase with photocurrent before saturation. This is the well-known bandwidth enhancement that originates from the current-induced electric field in graded absorption layer. The compression at -10 V bias was measured versus photocurrent. The marked “1 dB” in Figure 5.1 (b) illustrates the definition of the 1 dB saturation point, at which the compression decreases by 1 dB from its peak value. A 40-μm device exhibited saturation

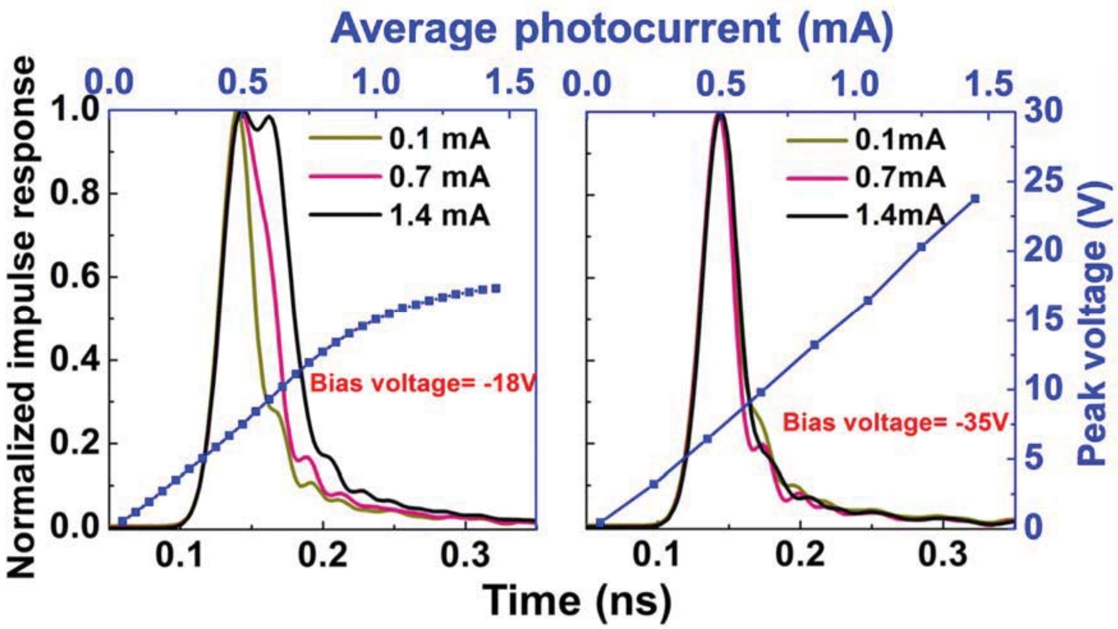

Figure 5.2 Normalized impulse response and peak voltage for different average photocurrents.

current at 1 dB compression point of 117 mA, 134 mA, 176 mA, 210 mA and 234 mA, and RF output power of 20.8 dBm, 23 dBm, 26.3 dBm, 29.8 dBm and 29.8 dBm at -3 V, -4 V, -6 V -8 V and -10 V bias, respectively. The device failed at -10 V bias and 234 mA average photocurrent. Note that Joule heating can create a runaway situation; an increase in junction temperature results in higher dark current, which in turn increases the junction temperature. At high temperatures, this process becomes unstable and the current increases until the device fails [25, 40].

For pulsed-illumination, the photodiodes can handle higher bias voltage, which enables higher output peak voltage pulses compared with CW operation since the generated heat does not have enough time to build up.

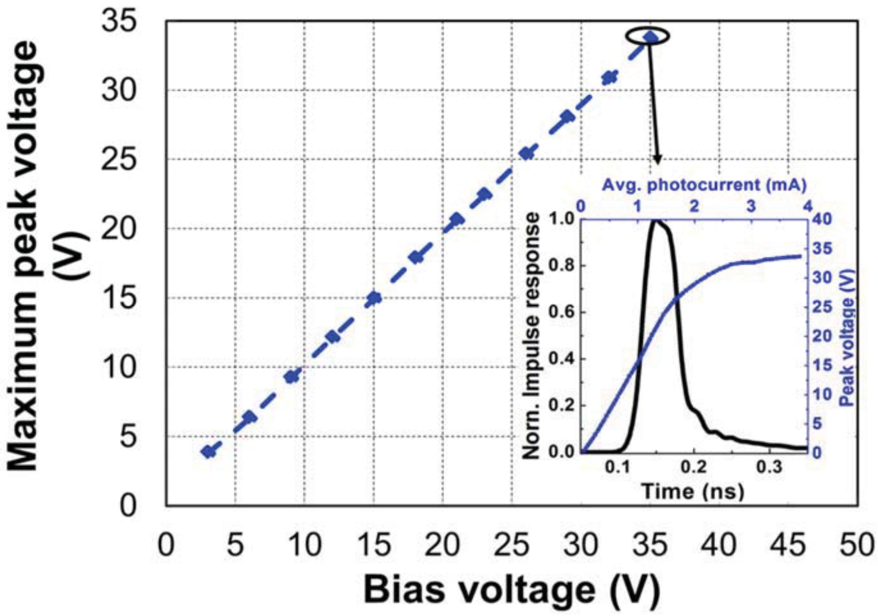

Figure 5.3 Maximum peak voltage output versus bias voltage.

For initial characterization of the impulse response, an Erbium doped fiber laser with pulse width of < 80 fs and 100 MHz repetition rate was used as the optical pulse source. Figure 5.2 shows the normalized impulse responses and peak voltage at different average photocurrents when the bias voltage is -18 V and -35 V. As average photocurrent increases, initially the peak voltage increases linearly and then begins to saturate with obvious pulse shape distortion. For -18 V bias voltage the peak voltage begins to saturate and exhibit pulse broadening at 0.7 mA average photocurrent. With increasing average photocurrent up to 1.4 mA, the peak voltage saturates completely and large pulse shape distortion, resulting from the space charge effect, can be observed. By applying higher bias voltage, the space charge effect can be mitigated with concomitant reduction in pulse shape distortion. When -35 V bias voltage is applied, the pulse shape remains unchanged

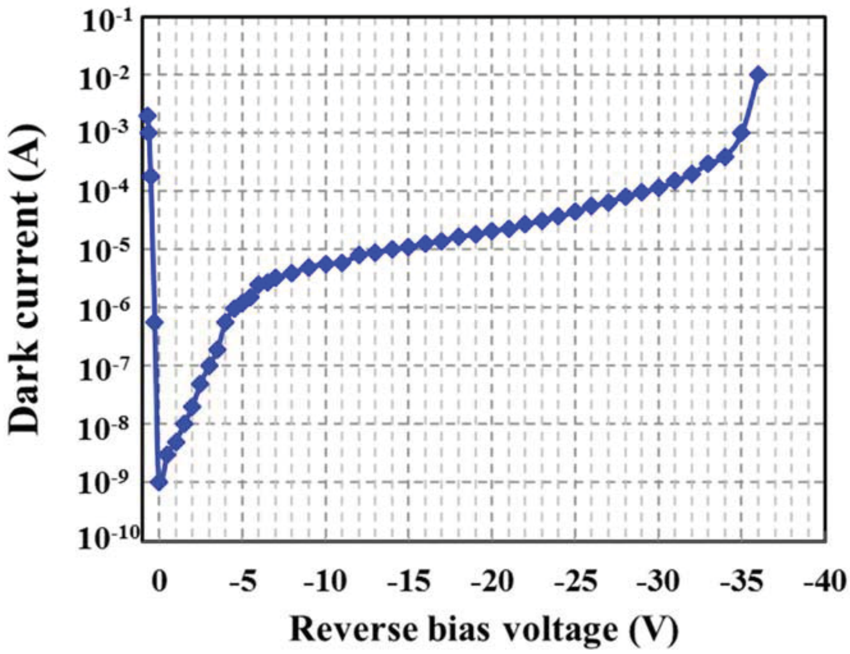

Figure 5.4 Current-voltage characteristic of a 40-μm diameter device.

up to 1.4 mA average photocurrent. In order to determine the maximum peak voltage at different bias voltages, the average photocurrent was increased until the pulse completely saturated. Figure 5.3 shows the maximum peak voltage versus bias voltage. The inset plot is the normalized impulse response for 3.8 mA average photocurrent and -35 V bias voltages and the pulse saturation verse average photocurrent at -35 V bias. The slope is ~1; the termination point coincides with junction breakdown as shown in Figure 5.4, which shows the dark current versus bias voltage; avalanche breakdown occurs for bias > 35V. For -35 V bias, the peak voltage and FWHM are 33.5 V and 50 ps, respectively. The peak voltage (33.5 V) and bandwidth (13 GHz) product is the highest reported for operation at 1.55 μm, including InGaAs PIN photodiodes [94] and uni-traveling carrier photodiodes [95].

5.3 Photonic generation of high-power pulsed RF signals

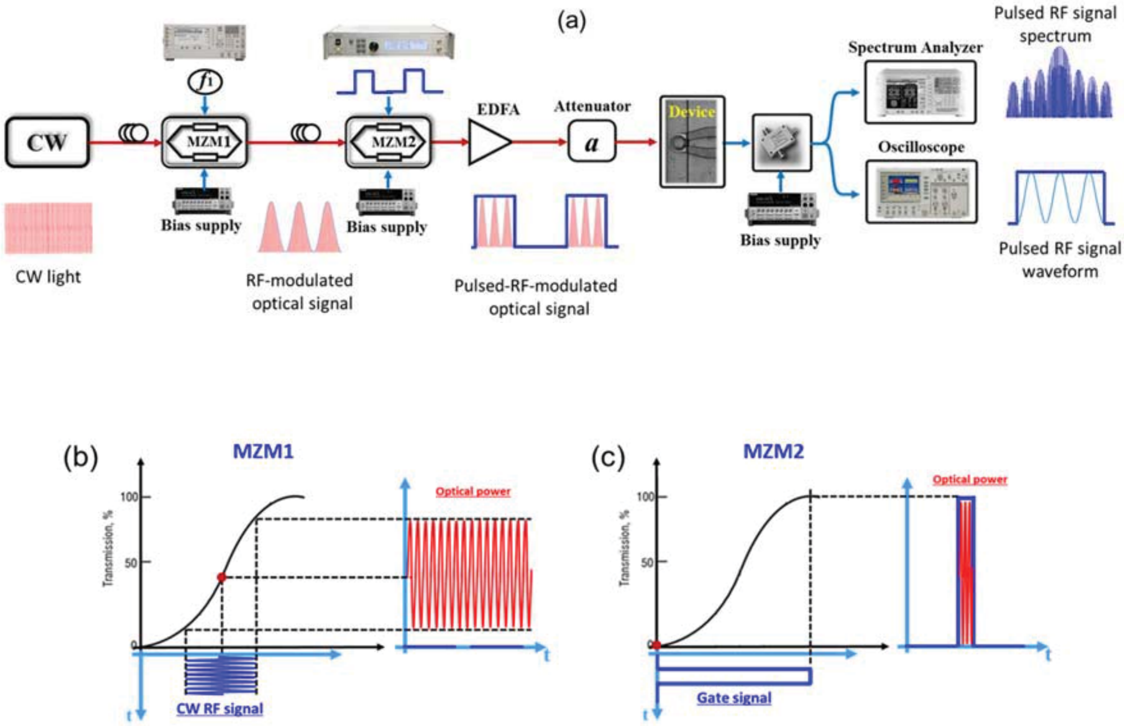

Figure 5.5 (a) Experimental setup for generation of high-power optical pulsed microwave signals. (b) and (c) show the modulation signals and output signals of the first and second modulators, respectively.

Figure 5.5 (a) is a block diagram of the high-power pulsed apparatus. A narrow linewidth fiber laser with 17 dBm optical output power and 1550 nm wavelength was used as a continuous wave (CW) optical source. Light from the laser was coupled into the first Mach-Zehnder modulator, which has V_π of 9 V and 20 GHz bandwidth. The modulator was driven by a CW RF signal with frequency of 1 GHz or 10 GHz and power of 14 dBm. The modulator was biased at the quadrature bias point as shown in Figure 5.5 (b). Here the CW RF signal was the carrier signal of the pulsed microwave signal. The gated RF signal was impressed on the optical signal by the second modulator. A 100 ns electrical pulse signal with variable duty cycle was applied to the second modulator, which operates at a low bias point. The offset voltage of the electrical pulse was set as 0 V to ensure that the entire RF carrier signal was confined in the pulse as shown in Figure 5.5 (c). Note that the measured optical extinction ratio of the second modulator is > 30 dB. The peak voltage of the electrical pulse was ~ 9 V (V_{pi} of the second modulator) in order to obtain the maximum pulsed RF modulated optical signal. An Erbium-doped fiber amplifier with maximum output power of 33 dBm was used to increase the power level of the pulsed RF modulated optical signal. Following the EDFA, a 1-nm optical bandpass filter was employed to suppress the noise from the EDFA. An optical attenuator was used to adjust the input optical power to the photodiodes. The pulsed-RF-modulated optical signal was converted to a pulsed RF signal by the high-power CC-MUTC photodiodes. A bias tee with low frequency cut-off of 20 kHz was used to bias the photodiodes. The frequency spectrum was characterized with an electrical spectrum analyzer and a 50 Ω-sampling oscilloscope was used to acquire the waveform. The microwave signal generator, gate signal, and oscilloscope were synchronized. Due to the power limitations of the oscilloscope and the spectrum analyzer, a microwave attenuator (56 dB) was used in the experiment.

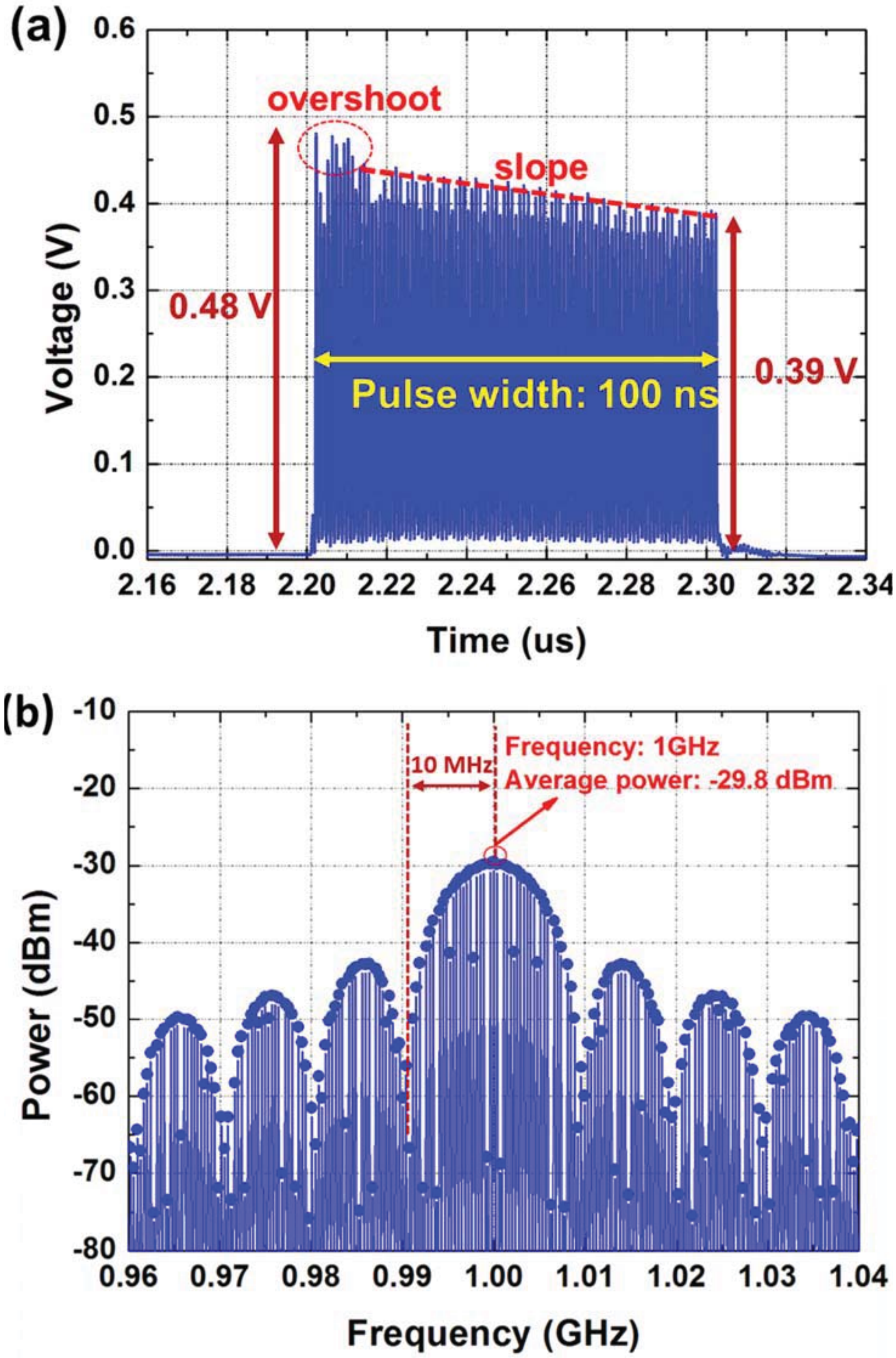

Figure 5.6 (a) Waveform of the pulsed RF signal and (b) spectrum of the pulsed RF signal measured at 0.2 mA average photocurrent.

Figure 5.6 (a) shows the waveform of the pulsed RF signal with 1 GHz carrier RF signal for ~ 0.2 mA average photocurrent. The pulse width of the pulsed RF signal is 100 ns and the duty cycle is 5%. There is no apparent power leakage outside the pulse. The maximum and minimum peak voltages (V_p) of the pulse are ~ 0.48 V and ~0.39 V, respectively. As shown in Figure 5.6 (a) overshoot and pulse slope are observed. The pulse overshoot depends on the bias point and the ratio of the input electrical gate signal voltage to the half-wave voltage of the modulator. When the input electrical gate signal voltage is larger than the half-wave voltage by 5%, an 8 % bias point shift from the low bias point resulted in 3 % overshoot. Note that a bias point controller can be used to remove the bias point shift and mitigate pulse overshoot. Figure 5.7 shows the normalized pulse shape at the output of the EDFA after optimization of the bias point of the second modulator. Three pulse repetition rates were used: 500 kHz, 750 kHz, and 1 MHz with a 5% fixed duty cycle. The corresponding pulse widths were 100 ns, 67 ns, and 50 ns, respectively. The reverse bias applied to the photodiode was -7 V and the average photocurrent was 1 mA. The input average optical power to the EDFA was -26 dBm and the corresponding input peak optical power was -13 dBm. In order to verify that the pulse slope arises from the gain dynamics of the EDFA [22] rather than in the photodiode or another point in the experimental setup, the pulse shape was measured without the EDFA. That response is shown in the inset of Figure 5.7. The bias voltage and average photocurrent were -7 V and 1 mA, respectively. The pulse repetition rate was 500 kHz and the duty cycle was 5 %. Under these conditions, the slope is not observed. In addition, the overshoot is not observed after optimizing the bias point of the second

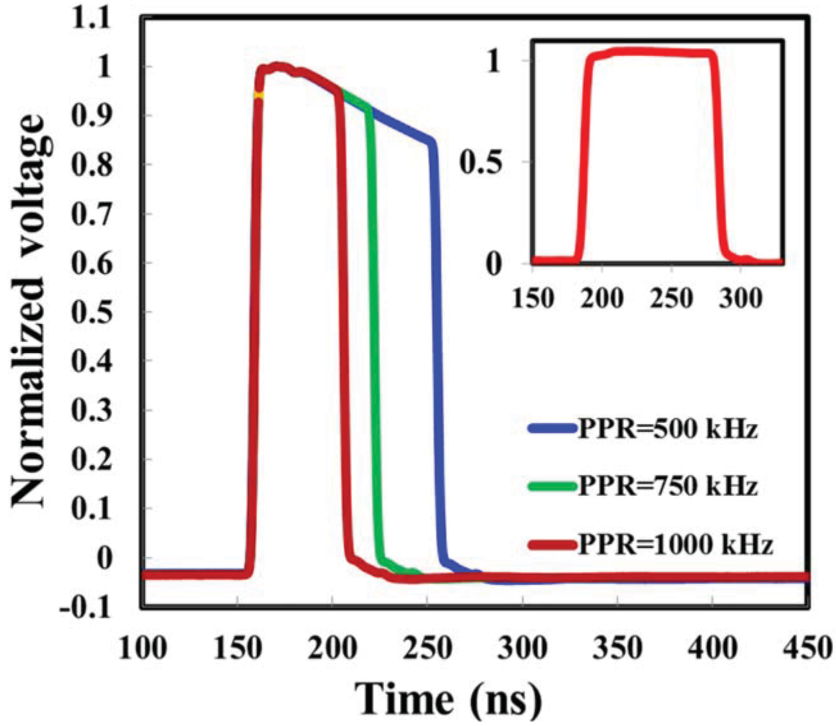

Figure 5.7 Normalized pulse shape with different pulse repetition rates after EDFA. Inset: normalized pulse shape without EDFA.

modulator. Figure 5.6 (b) shows the spectrum of the pulse signal. The spectrum analyzer was set to line spectrum mode in order to get the individual spectral components of the pulsed RF signal [96]. From the spectrum shown in Figure 5.6 (b), the power of every individual spectral component can be measured by using the band power marker function of the analyzer; the frequency interval between two adjacent spectral components is equal to the pulse repetition rate. The peak power (P_{peak}) can be calculated based on the following equation [96].

$$P_{peak}\ (\text{dBm}) = P_m\ (\text{dBm}) - 20\log(\tau/T) \tag{5.1}$$

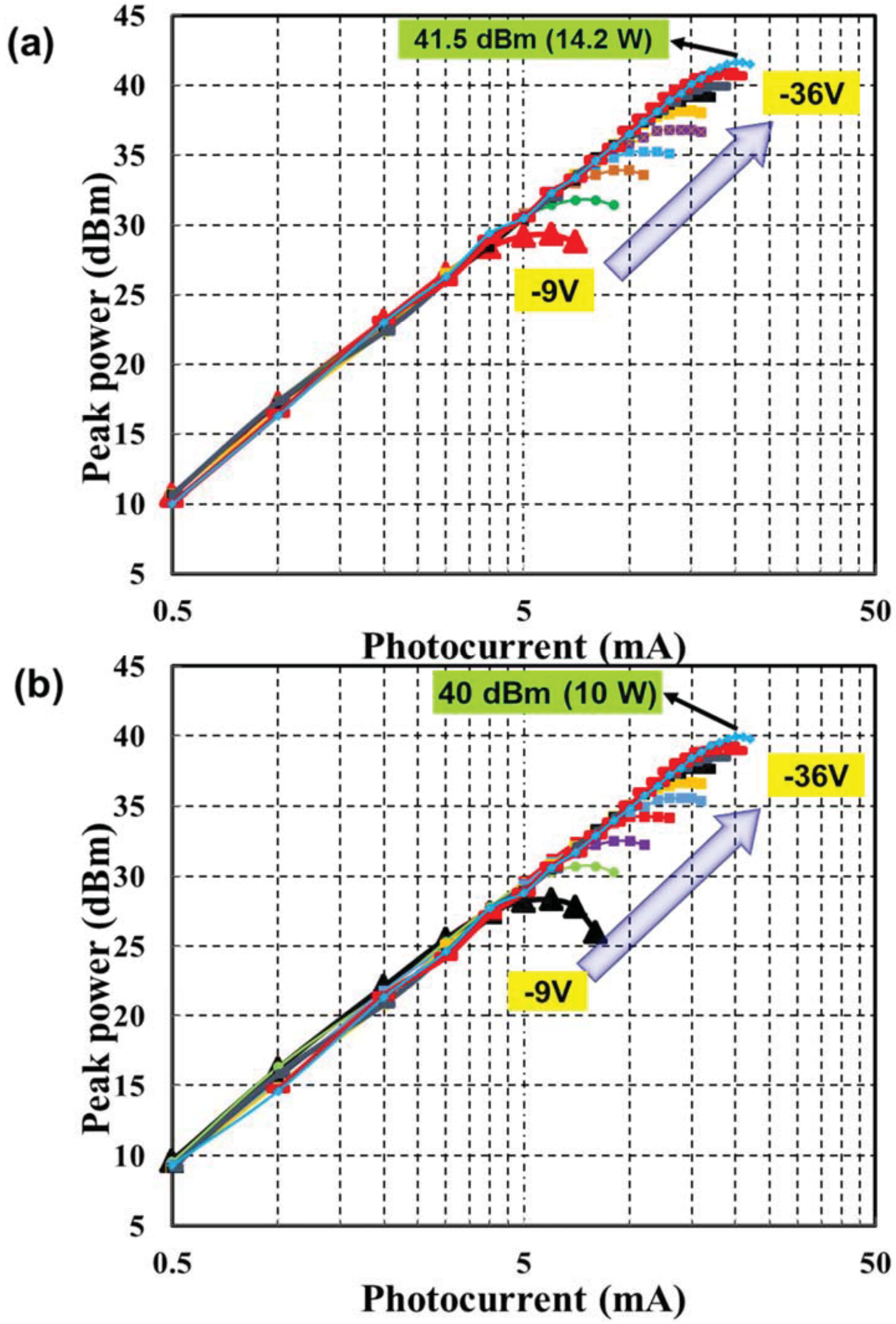

Figure 5.8 (a) Peak power of 1 GHz pulse signal and (b) 10 GHz pulse signal at different photocurrents and bias voltages.

where τ is the pulse width, T is the pulse period, and P_m is the measured power of the central line of the main lobe in the spectrum. Based on Eq. (5.1), the peak power is -3.5 dBm and the corresponding $V_{p\text{-}p}$ of the pulse is ~ 0.42 V, which agrees with the measured waveform shown in Figure 5.6 (a). The average power (P_{avg}) can be calculated based on the following equation [96]:

$$P_{avg}\,(\text{dBm}) = P_{peak}\,(\text{dBm}) + 10\log(\tau/T) \tag{5.2}$$

Figure 5.8 (a) shows the peak power of the pulsed 1 GHz RF signal versus average photocurrent at bias voltages in the range -9 V to -36 V with -3 V step when the pulse repetition rate was fixed at 20 MHz and the duty cycle was 5%. The peak power increases linearly as the average photocurrent increases and then saturates due to the space-charge effect. When the bias voltage was -9 V, the photodiode began to saturate at 4 mA average photocurrent and 28.4 dBm peak power as shown in Figure 5.8 (a). When the bias was increased to -36 V, the maximum output peak power reached 41.5 dBm (14.2 W) and the corresponding average photocurrent was 21 mA. The peak power of the pulsed 10 GHz RF signal versus photocurrent at different bias voltage is plotted in Figure 5.8 (b). The maximum peak power was 40 dBm (10 W) when the bias voltage was -36 V and the average photocurrent was 20 mA. Compared with 1 GHz RF carrier signal, the lower peak power for the 10 GHz is due to limited bandwidth of the first modulator and bandwidth of photodiode. When the bias voltage of the photodiode was increased to -37 V, the photodiode failed. Based on Figure 5.4, we conclude that the devices are limited by the breakdown voltage rather than thermal failure at 5% duty cycle.

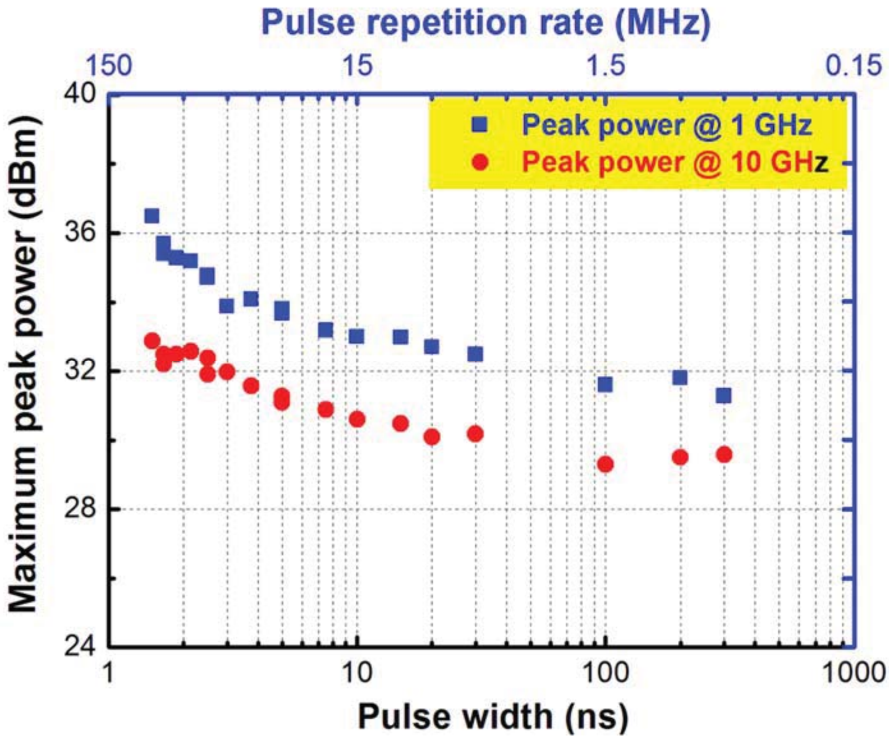

Figure 5.9 Maximum peak power of the pulsed RF signal at different pulse widths.

The relationship between maximum peak power and pulse width/repletion rate was also studied. The bias voltage and duty cycle were -18 V and 15%, respectively. By increasing the average photocurrent, we obtain the peak power verse average photocurrent, which shows the saturation of the photodiode shown in Figure 5.8. The maximum peak power at different pulse width/repletion rate was obtained by increasing the average photocurrent. As shown in Figure 5.9, as the pulse width decreased from 300 ns to 1.5 ns, the maximum peak power at 1 GHz (10 GHz) increased from 31.3 dBm (29.6 dBm) to 36.6 dBm (32.9 dBm). Since shorter optical pulses experience less saturation in the EDFA [97], the short pulses maintained a rectangular waveform as well as high peak

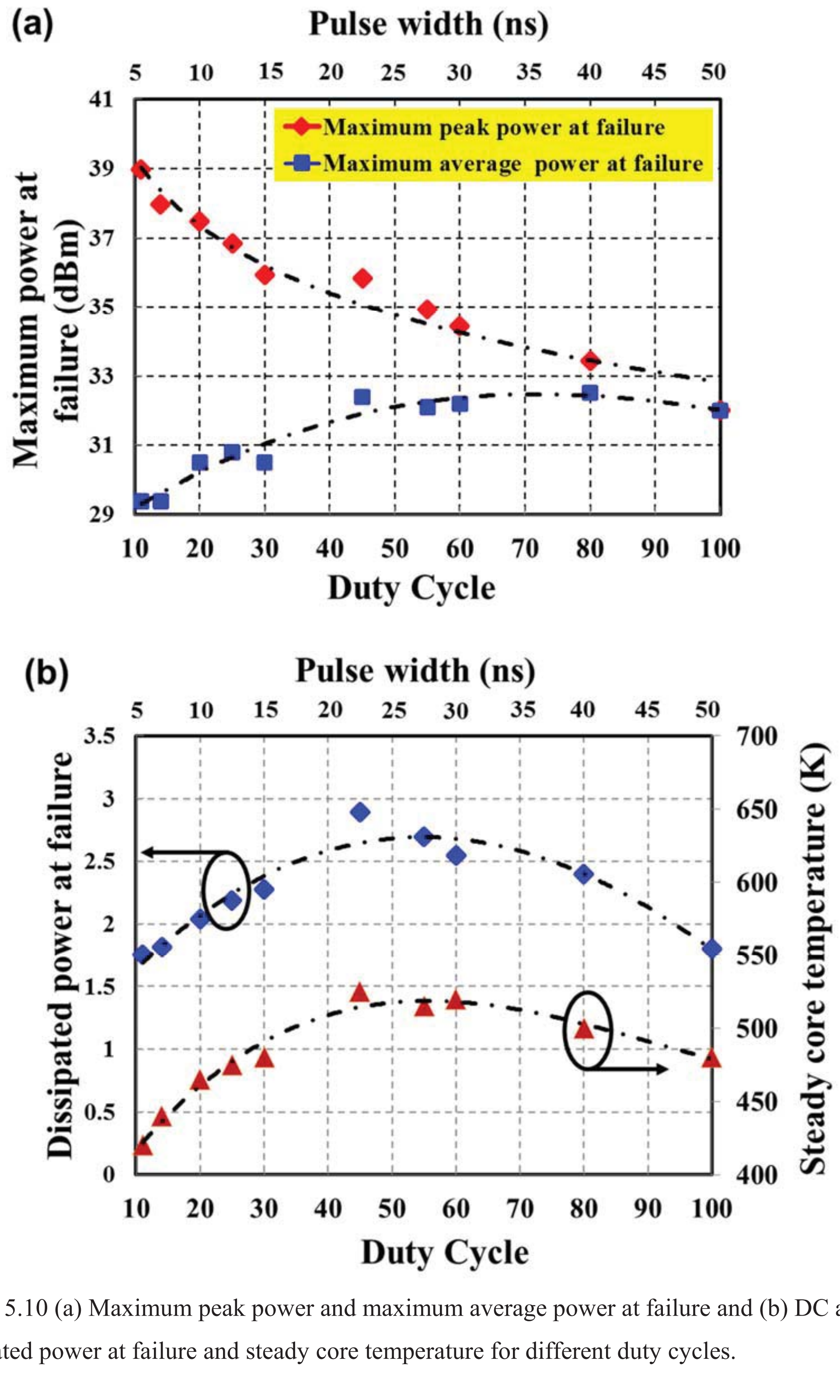

Figure 5.10 (a) Maximum peak power and maximum average power at failure and (b) DC average dissipated power at failure and steady core temperature for different duty cycles.

power. Therefore, in addition to increasing the bias voltage, reducing the pulse width can benefit high-power pulsed RF signal generation. The 10 GHz pulse signal has lower peak power compared with the 1 GHz pulse signal by 1.5 dB due to the limited bandwidths of the first modulator and the photodiode. The pulse width of the electrical gate signal, the saturation of the EDFA, and the breakdown voltage of the photodiode limit the maximum peak power. By incorporating a high bandwidth modulator or a pulsed mode EDFA, the peak power of the pulse signal with higher frequency RF carrier signal could be further improved.

Figure 5.10 (a) shows the maximum peak power and maximum average power at failure for different duty cycles/pulse widths. The pulse repetition rate was set as 20 MHz. For every duty cycle, the maximum peak power at failure was determined by increasing the photocurrent and the bias voltage until the device failed. The lower the duty cycle the higher is the bias voltage at failure. When the duty cycle was 11 %, the failure voltage was -36 V. The breakdown voltage of these photodiodes is ~ 37 V as shown in Figure 5. Therefore we were unable to obtain the failure power at < 11 % duty cycle. The maximum average power at failure increases by ~ 3 dB as the duty cycle increases from 10 % to 45 %. As the duty cycle increases from 50 % to 100 %, the maximum average power decreases by ~ 0.5 dB. Note that the average power at failure is proportional to the dissipated power at failure assuming that the power conversion efficiency of the photodiode is unchanged. Therefore the maximum average power at failure peaks where the dissipated power at failure peaks as shown in Figure 5.10 (b). The maximum peak power at failure drops from 39 dBm to 32 dBm as the duty cycle increases from 10 % to 100 %, which agrees with Eq.

(2). Figure 5.10 (b) shows the DC dissipated power and steady core temperature at failure for different duty cycles. A 3-D thermal model based on the finite-element simulator COMSOL Multiphysics was created to determine how the duty cycle affected the thermal profile using the model in [98]. Based on the measured dissipated power the steady junction temperature was simulated for different duty cycles. When the duty cycle decreases from 100 % to 45 %, the dissipated power increases by 1.1 W. The steady state junction temperature at failure increases from 480 K to 525 K owing to thermal runaway between pulses. Pulsed operation can reduce the junction temperature compared with CW operation (100 % duty cycle) [58]. When the duty cycle decreases from 45 % to 10 %, the dissipated power at failure drops by 1.2 W and the steady state junction temperature at failure drops from 525 K to 420 K. For this range of duty cycles the junction breakdown becomes more significant than thermal failure.

5.4 Summary

In this chapter, an optical generation of high-power pulsed microwave signals using charge-compensated modified uni-traveling-carrier (CC-MUTC) photodiodes has been discussed. These CC-MUTC photodiodes achieved pulses with peak voltage of 33.5 V and FWHM of 50 ps at -35 V bias voltage. The peak power levels for gated modulation at 1 GHz and 10 GHz were 41.5 dBm (14.2 W) and 40 dBm (10 W), respectively.

Chapter 6 Heterogeneously integrated waveguide-coupled photodiodes on SOI

6.1 Introduction

In this chapter integration of the high-power MUTC photodiodes on SOI waveguides using a heterogeneous wafer-bonding technology [27] is described. We show that by optimizing the epitaxial layer structure, a single MUTC photodiode on SOI waveguide with 210 μm^2 area can achieve 48 GHz bandwidth and a 10×35 μm^2 PD can reach 0.95 A/W internal responsivity and output >12 dBm RF power at 40 GHz modulation frequency. Balanced MUTC photodiodes of this type achieved 0.78 A/W internal responsivity, 14 GHz bandwidth, 17.2 dBm RF output power at 10 GHz, and 15.2 dBm RF output power at 20 GHz. These are the highest RF output power levels reported at multi-GHz frequencies for any waveguide photodiode technology including native InP, Ge/Si, and heterogeneous integration [28].

6.2 Device design and fabrication

Figure 6.1 (a) and (b) show the layer structure and a scanning electron microscope (SEM) image of a MUTC photodiode (PD) heterogeneously integrated on SOI waveguide, respectively. Similar to the MUTC photodiodes described in previous chapters, the layer structure is designed to mitigate saturation. For the initial first devices

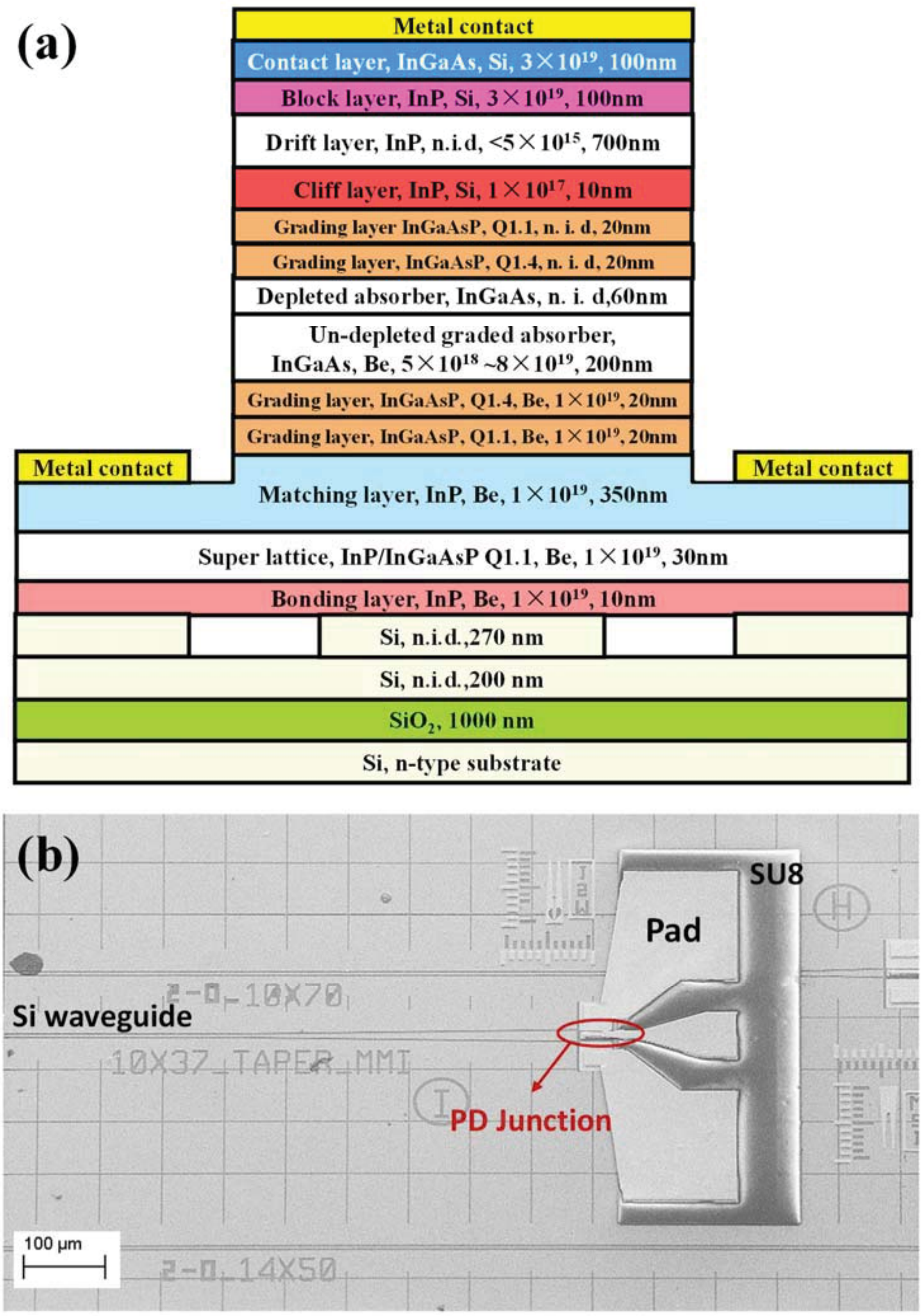

Figure 6.1 (a) Cross-section of MUTC PD on SOI. Doping concentrations in cm^{-3}. (b) SEM picture of fabricated MUTC PD on SOI.

of this type that were studied, a 10-nm n-type doped cliff layer was used to enhance the electric field in the depleted portion of the absorption layer. A graded doping profile was used to create a quasi-electric field in the undepleted absorber. A 700 nm-thick unintentionally doped InP electron drift layer was incorporated to reduce the junction capacitance. A 10 nm thick bonding layer and an InP/InGaAsP super lattice were placed below the p+ contact/matching layer to reduce the propagation of defects into the active region and to facilitate wafer bonding onto Si. The photodiode active region is evanescently coupled to the underlying SOI waveguide. The thickness of the Si rib and buried oxide layer are 0.47 μm and 1 μm, respectively. All light is confined in Si waveguide layer based on Rsoft simulation. Three changes to improve the output power and increase the bandwidth were made to the second version of this photodiode: Thin bandgap-graded InGaAsP layers were added between the InGaAs absorber and the InP matching layer to smooth the abrupt band barrier and prevent carrier pile-up, the undepleted absorber thickness was reduced to shorten electron transit time, and most importantly, the thickness of the InP matching layer was increased from 70 nm to 350 nm to lower the series resistance and to improve uniformity of the optical illumination in the absorber. In this work, the series resistance is < 10 Ω.

The photodiode fabrication process starts with dry etching the SOI waveguides. To match the width of the active PD region (10 μm and 20 μm) the 2-μm wide passive single-mode input Si waveguide was tapered. Then, the III-V photodiode material dies were plasma activated and bonded at room temperature to the Si waveguide layer. The III-V substrate was removed via wet chemical etching, leaving active device layers for

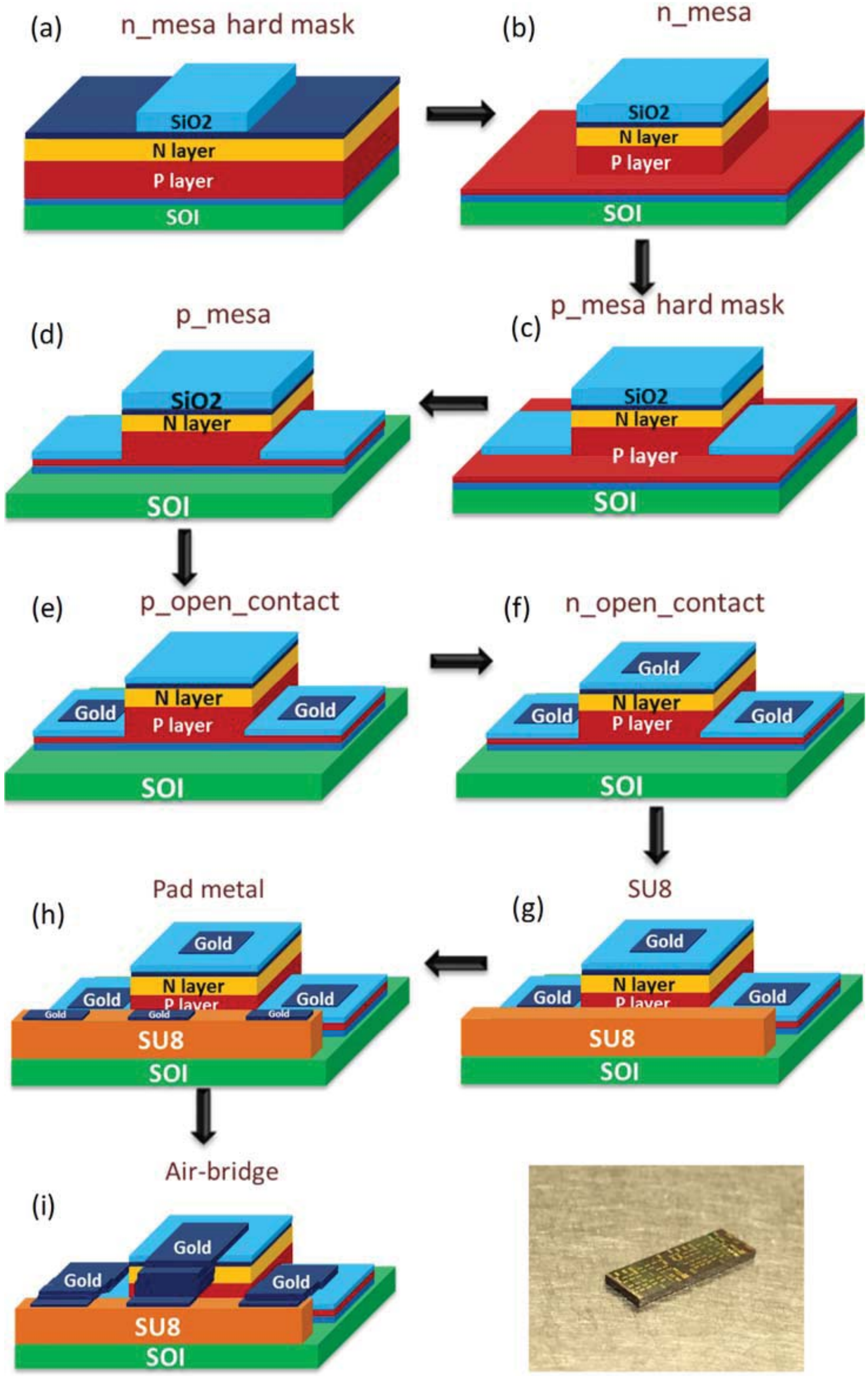

Figure 6.2 Fabrication process flow of MUTC waveguide photodiode on SOI.

fabrication [6]. An Ti (10 nm)/AuGe (40 nm) /Au (40 nm)/Ni (80 nm) blanket metallization was deposited on the InGaAs contact layer in E-beam evaporator. The SiO_2 is deposited on metal directly and then patterned by photoresist which is shown in Figure 6.2 (a). Self-aligned inductively coupled plasma reactive ion etch (ICP-RIE) was used to etch down to p-contact/matching layer to form the n-mesa. This process is illustrated in Figure 6.2 (b). After finishing etching n mesa, the same etch flow is applied to form p mesa shown in Figure 6.2 (c) and (d). It should be mentioned that the SiO_2 layer serves as either hard mask or passivation layer. In order to deposit metal contact layers on the p mesa, the SiO_2 on the p mesa should be etch away first. I used BOE wet etch or a mixture of BOE wet etch and Oxford dry etch depending on the thickness of the SiO_2 layer. After opening the SiO_2 layer, the p-contact layer (Ti (20 nm)/Pt (20 nm) /Au (80 nm)) was evaporated on the p mesa and then the metal on the photoresist was lifted off as shown in Figure 6.2 (e). After forming the p contact, the SiO_2 on the n mesa was etch through to expose the metal layer deposited at the beginning of the fabrication process as shown in Figure 6.2 (f). To reduce the RF loss originating from the low resistivity Si substrate, SU 8 layer was deposited on the Si substrate (Figure 6.2 (g)). The whole fabrication process is finalized by depositing pads on the SU8 and plating to form the air-bridge shown in Figure 6.2 (h) and (i). After fabrication, the wafer was separated into two pieces with a Disco Blade Saw. The final waveguide photodiode wafer is shown in Figure 6.2.

6.3 Experimental results

Waveguide MUTC photodiodes with different active areas were fabricated. Figure 6.3 shows typical measured I-V curves with dark currents below 10 nA at 5 V reverse bias. In order to determine the internal responsivity, the coupling loss from the fiber into the waveguide was measured using the cutback loss technique on a straight passive waveguide. Lensed fibers with a spot diameter of approximately 2.5 μm were used to couple light in and out of the waveguides. The coupling loss of the unpolished SOI waveguide was 12.8 dB/facet and includes reflection loss and waveguide propagation loss. The propagation loss for the SOI waveguide is 0.54 dB/cm [99], which can be

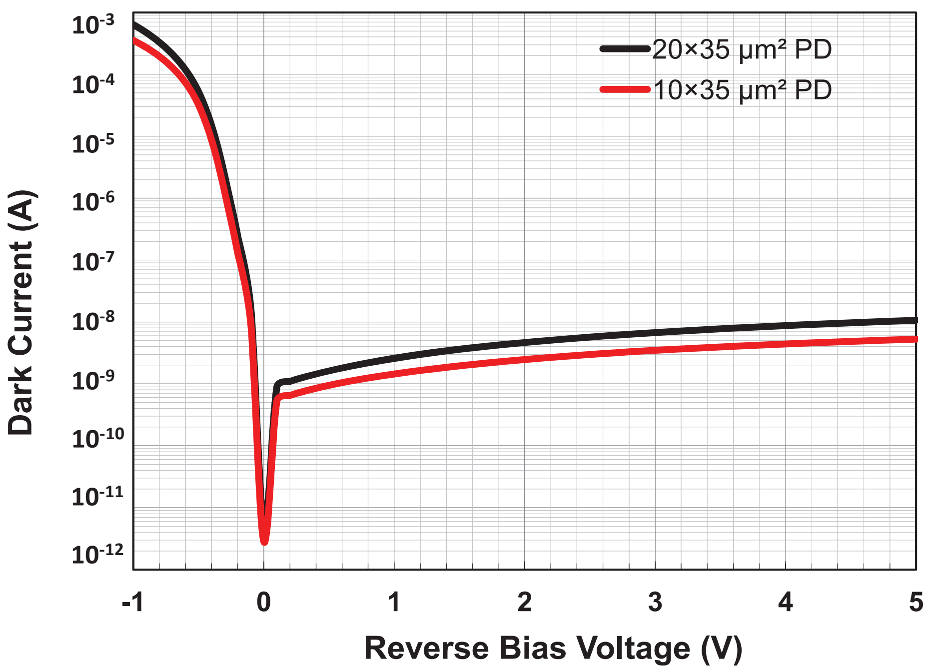

Figure 6.3 Measured dark currents of single MUTC PDs with 10×35 μm^2 and 20×35 μm^2 active area.

ignored for our waveguide. The coupling loss could be reduced by polishing the waveguide facet, depositing a SiO_2 anti-reflection layer on the waveguide facet or using a grating coupler. Based on the coupling loss measurement, we determined the internal responsivity to be as high as 0.64 A/W and 0.95 A/W for 21-μm and 35-μm long photodiodes, respectively. Note that the polarization of the input optical signal was adjusted to maximize the photocurrent since the waveguide has a polarization preference. Figure 6.4 compares the experimental results and a simulation that was obtained using beam propagation software.

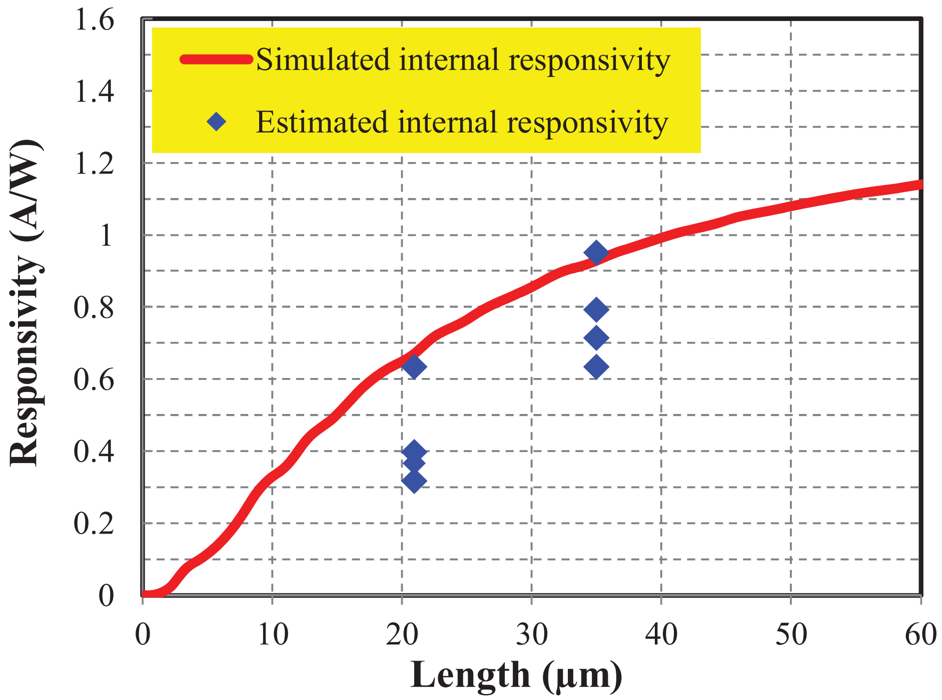

Figure 6.4 Estimated internal responsivity based on coupling loss measurement and simulated internal responsivity.

An optical heterodyne setup with wavelength of ~1550 nm and modulation depth close to 100 % was used to characterize bandwidth, saturation photocurrent, and RF output power. As shown in Figure 6.5, photodiodes with active areas of 10×21 μm^2, 10×35 μm^2 and 20×35 μm^2 exhibited bandwidths of 48 GHz, 31 GHz, and 18 GHz, respectively. Figure 6.6 summarizes the measured bandwidths from all tested devices. The red triangles show the calculated RC-limited bandwidth based on C-V measurements. The junction capacitance per unit area at -5 V is ~ 0.17 fF/μm^2 and the estimated pad capacitance is ~ 20 fF. The blue diamonds are the measured bandwidths of all tested

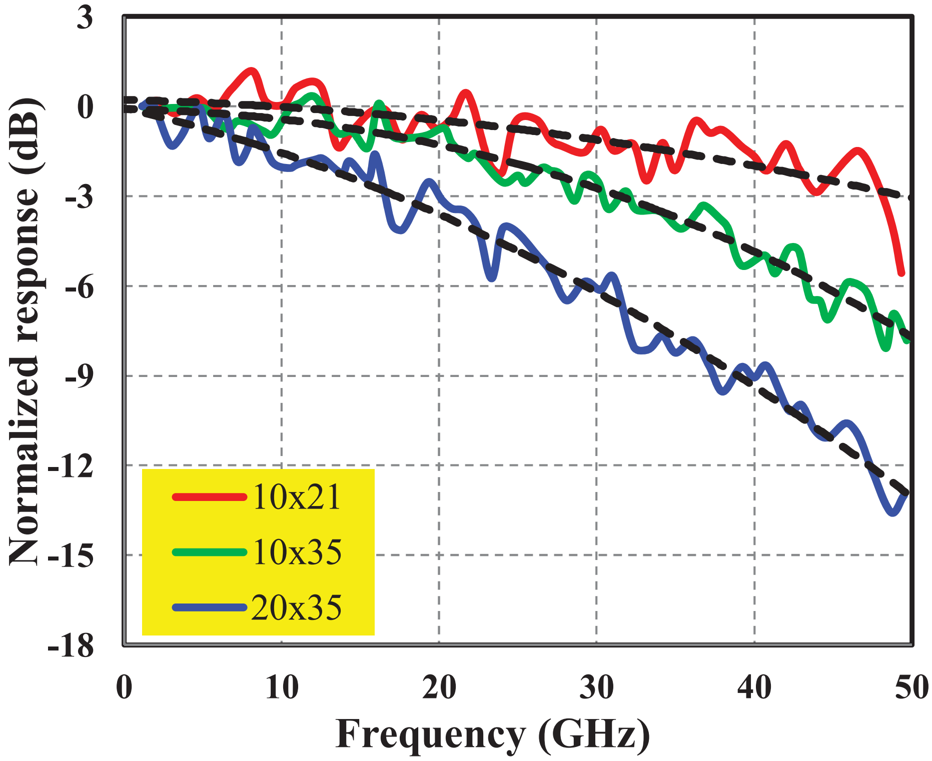

Figure 6.5 Frequency responses of 10×21 μm^2, 10×35 μm^2 and 20×35 μm^2 waveguide MUTC PDs measured at -6 V bias voltage (dashed lines are smoothed data).

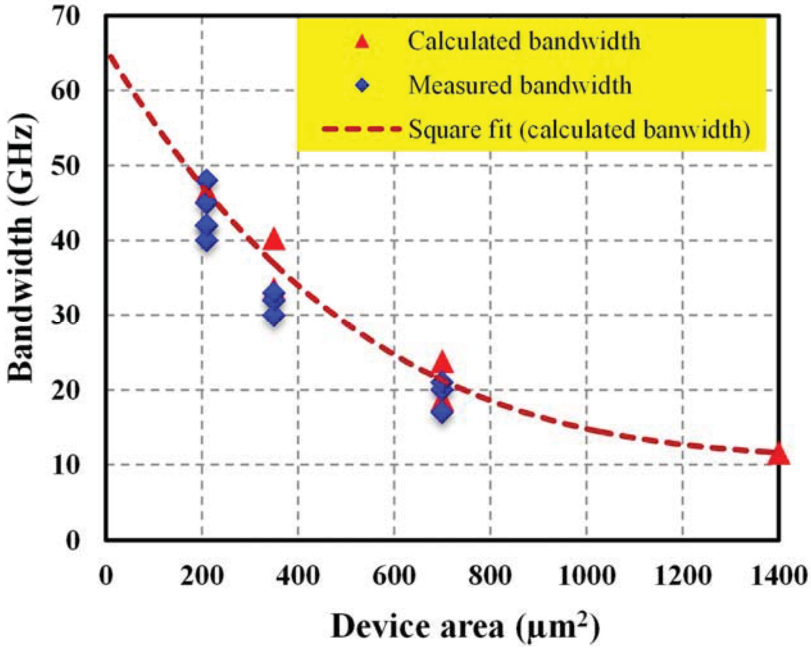

Figure 6.6 Measured bandwidths of different sized photodiodes and calculated RC-bandwidth based on C-V measurement.

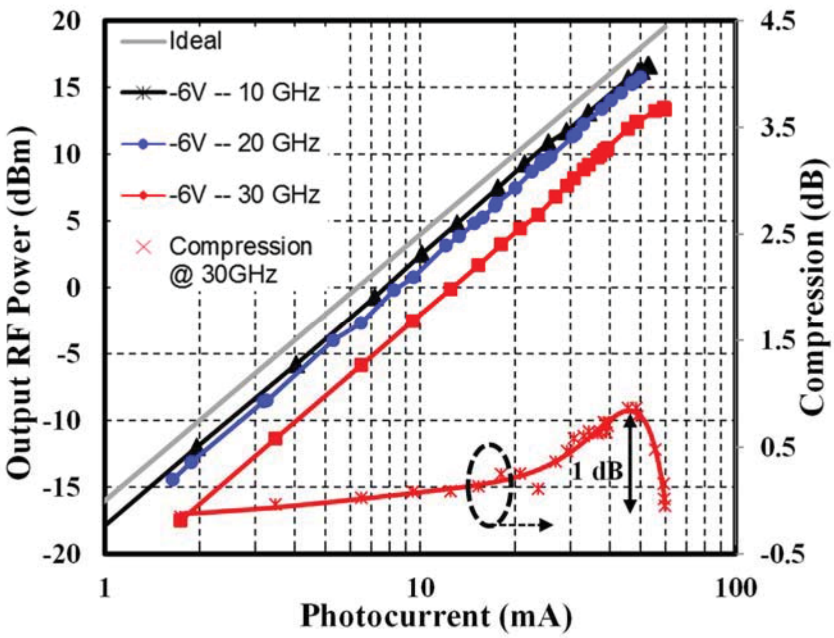

Figure 6.7 Output RF power of 20×35 μm^2 PD at -6 V bias voltage and power compression at 30 GHz vs. average photocurrent.

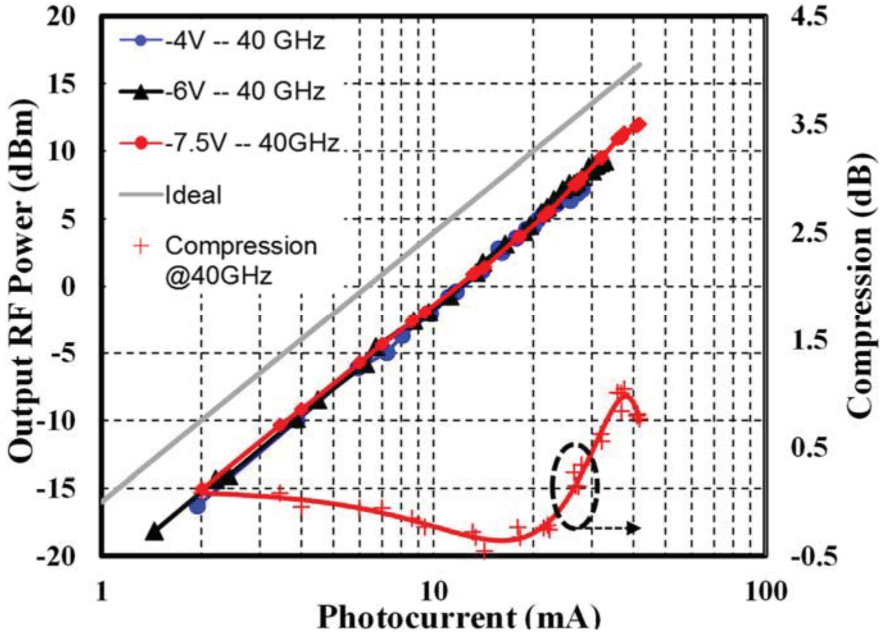

Figure 6.8 Output RF power at different bias voltages and power compression at -7.5 V of 10×35 μm^2 PD at 40 GHz.

devices. The fact that the measured bandwidths approach the calculations indicates that the bandwidth is primarily limited by the RC-time constant. Note that the expected transit time of this device is 5.7 ps, which corresponds to a bandwidth of 97 GHz. For devices with area < 200 μm^2 the bandwidths will be limited by the transit time.

The RF output power and the power compression versus average photocurrent measured at room temperature (no temperature control) for different modulation frequencies and bias voltages are shown in Figure 6.7 and Figure 6.8. The maximum measured RF output powers of a 20×35 μm^2 photodiode with the external 50 Ω load were 16.6 dBm, 15.8 dBm and 13.5 dBm at 10 GHz, 20 GHz and 30 GHz, respectively (Figure 6.7). It should be noted that the measured RF power approaches the ideal power-current line as the photocurrent increases. This is due to the previously described current-induced

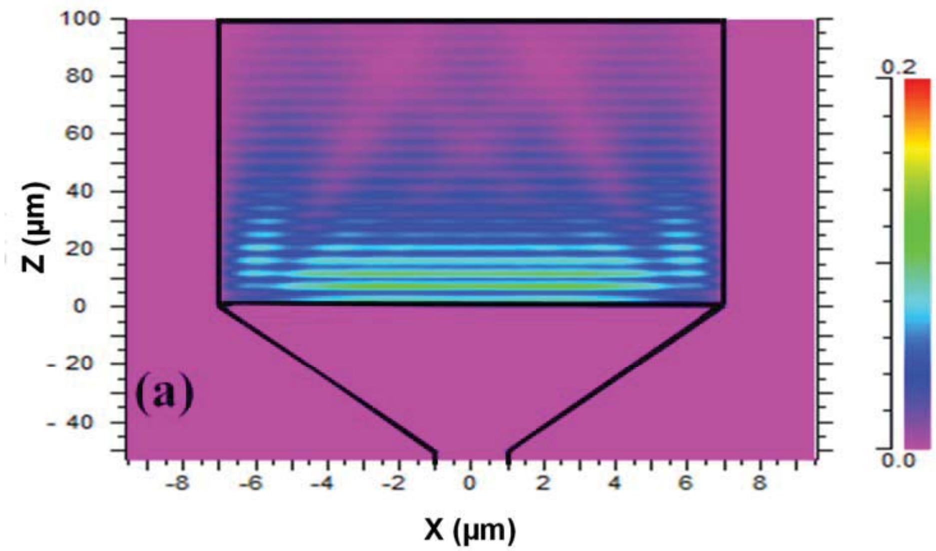

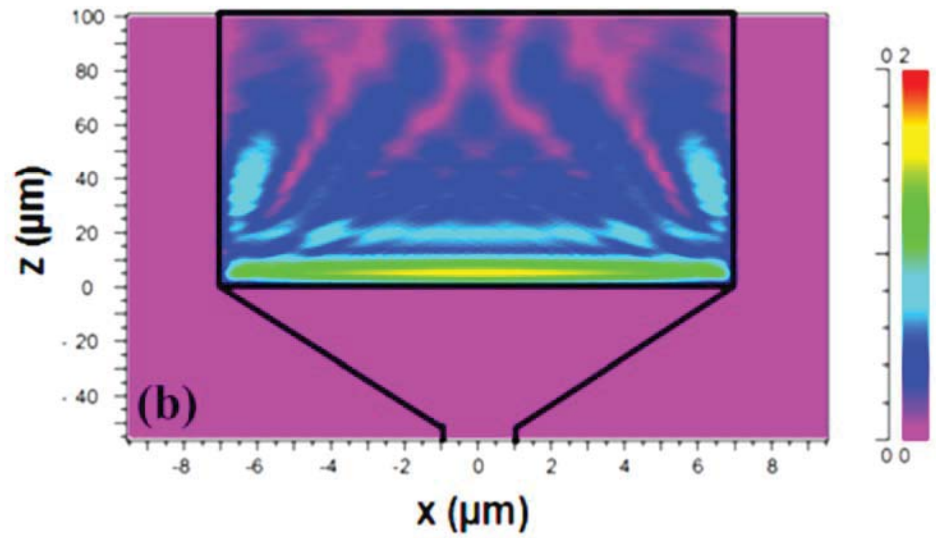

Figure 6.9 Simulated relative optical intensity profile in the plane of the absorber layer of (a) the optimized structure with a 350 nm-thick matching layer and (b) the structure in ref. [27]. The tapered silicon waveguide extends from z=-50 to 0 µm. The active PD area extends from x=-7 to 7 µm and z = 0 to 100 µm.

bandwidth enhancement effect that is caused by the self-induced electric field in the un-depleted absorber. The photodiode exhibited a 1-dB saturation current of 60 mA at 30 GHz. The maximum output RF power of the 10×35 μm^2 photodiode at 40 GHz was 12 dBm at -

7.5 V as shown in Figure 6.8. A 10×35 μm^2 photodiode exhibited 1260 mA·GHz saturation current-bandwidth product, which is the highest saturation current-bandwidth product we obtained. It is worth mentioning that the maximum RF output power levels were limited by the maximum available photocurrent for the 10×35 μm^2 device (the maximum input optical power is > 30 dBm) and thermal failure under high current operation for the 20×35 μm^2 device. These results are the highest output power levels measured for any high-speed waveguide photodiode technology including photodiode arrays.

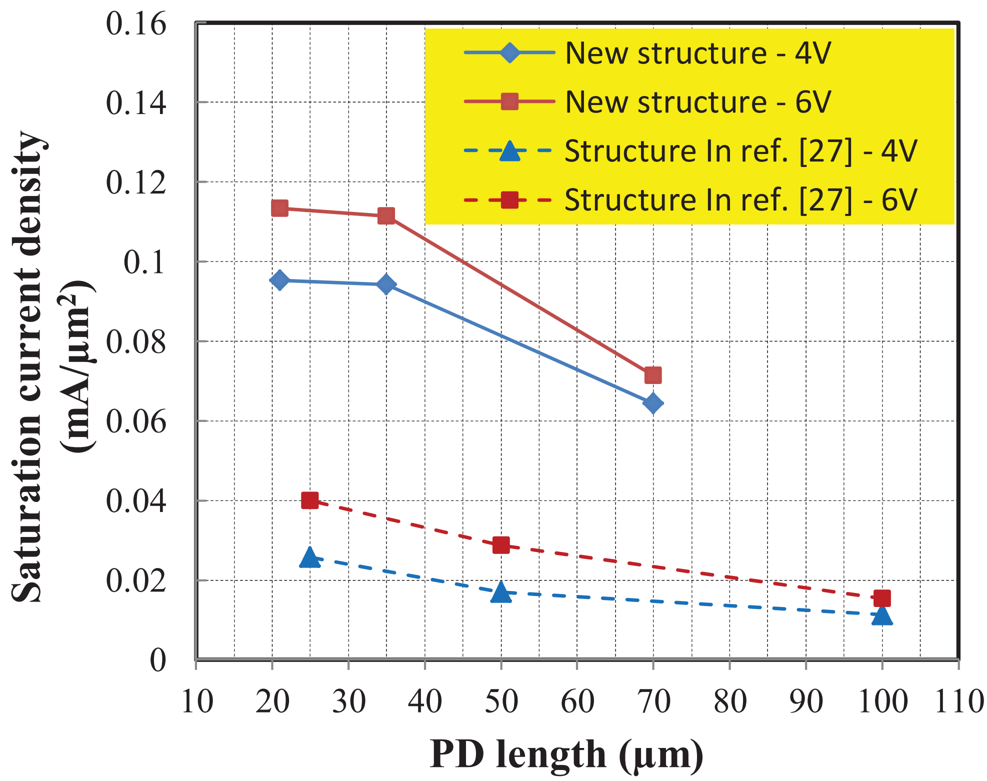

Figure 6.10 Saturation current measured at the 3 dB bandwidth normalized to PD active area as a function of PD length.

It is well known that the high-power performance of waveguide photodiodes is typically determined by the fact that the strongest absorption occurs at the input side of the photodiode, which can result in strong saturation in this region [27]. An advantage of

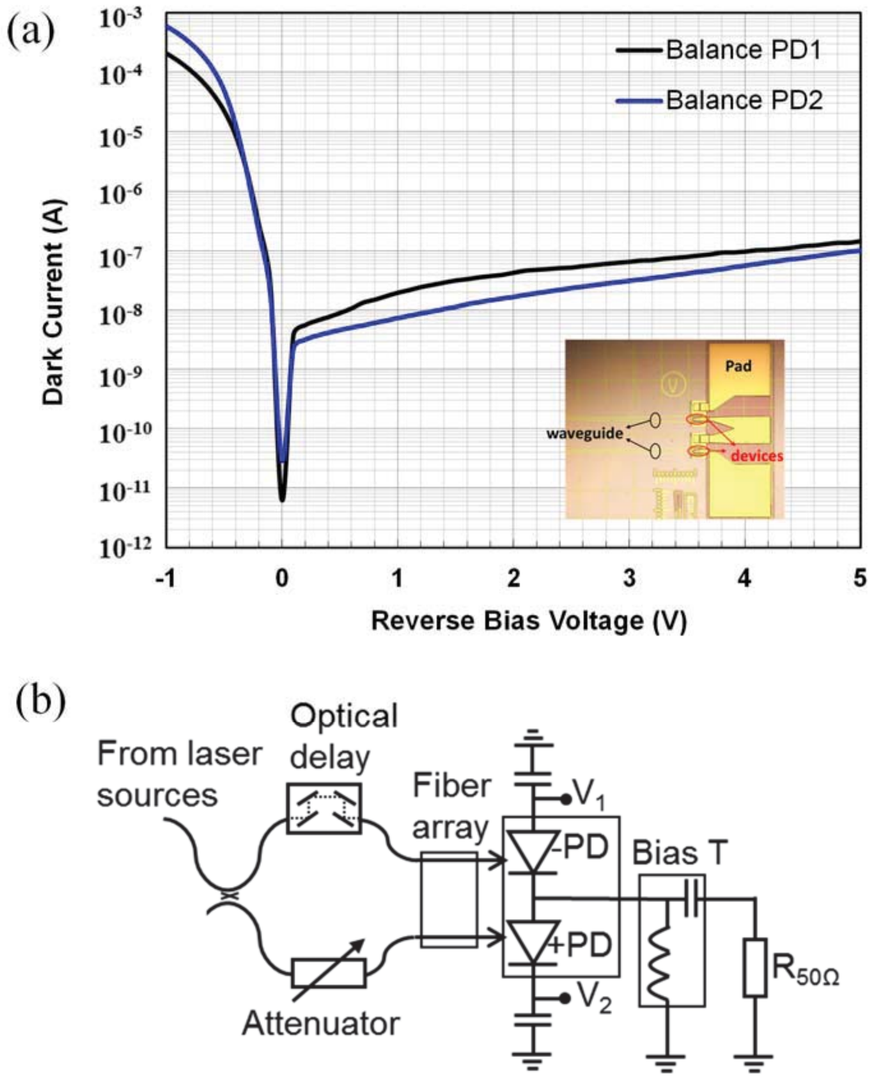

Figure 6.11 (a) Measured dark currents of 14×25 μm^2 balanced waveguide PDs. Inset: Micrograph of fabricated balanced waveguide PDs. (b) The experimental setup to characterize balanced photodiodes.

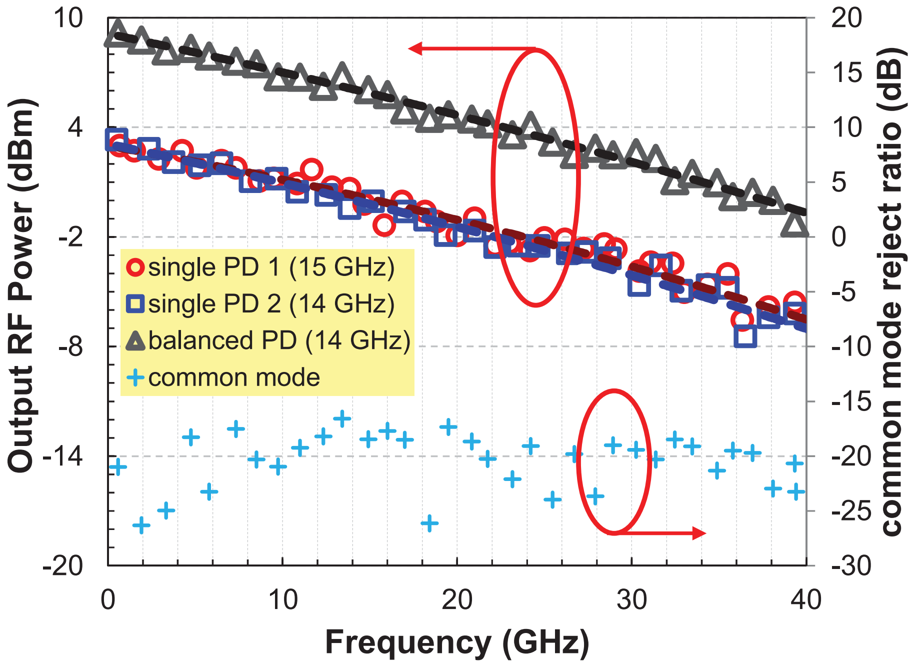

Figure 6.12. Frequency responses measured at +/-5 bias voltage and 10 mA photocurrent per PD. These frequencies in the legend are the bandwidth of PD 1, PD2 and balanced PD, respectively.

our heterogeneous process is the ability to independently change the widths of the Si waveguide and III-V mesa width to flatten the absorption profile. This capability, together with optimizing the thickness of the InP matching layer by simulating the optical intensity distribution in the plane of the absorption layer (Figure 6.9) is critical to achieve high saturation current. As shown in the Figure 6.9 (a) the optical intensity is relatively uniform within the first 35 µm and no intensity peaking is observed. Compared to the intensity profile of our previous structure (ref. [27]) shown in Figure 6.9 (b), the optimized structure exhibits a uniform optical intensity profile, which helps mitigate the localized saturation at high optical input powers. The same conclusion can be drawn from Figure 6.4, which indicates a linear increase in responsivity for short photodiode lengths and Figure 6.10

shows the measured saturation current density of the new structure and the structure in ref. [27]. The saturation current density of the new structure remains flat up to photodiode lengths of 35 μm. Compared with the previous structure in ref. [27], the new structure exhibits higher saturation current density.

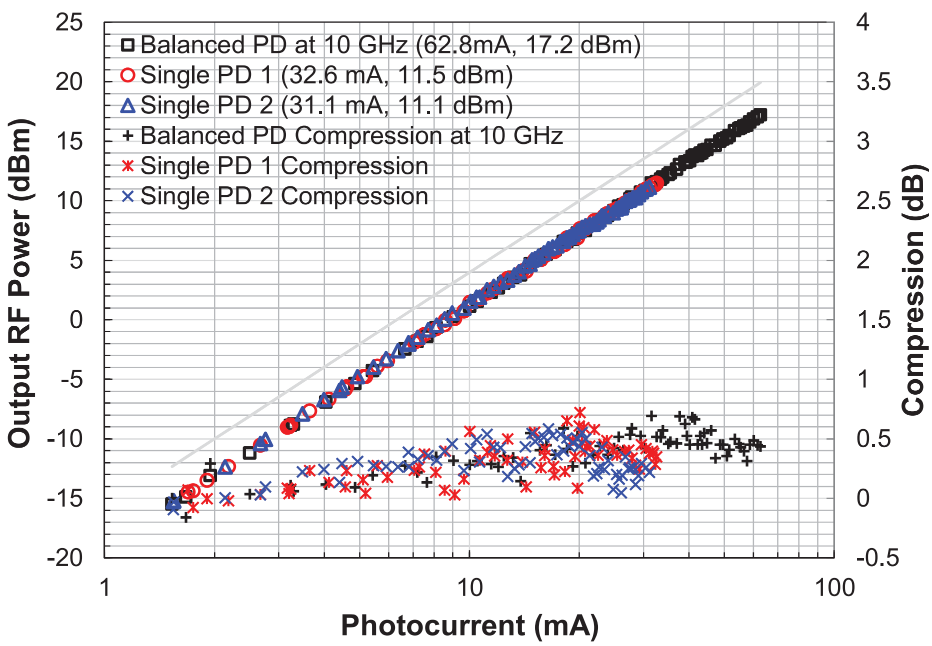

Figure 6.13 Output RF power of 14×25 μm^2 PD at +/-6 V bias voltage and power compression at 10 GHz vs. average photocurrent.

Using the same integration technology we have also designed and characterized balanced waveguide photodiodes. High-power balanced photodiodes are critical components for analog photonic links that employ heterodyne detection owing to their capability to suppress laser relative intensity noise and amplified spontaneous emission noise from erbium-doped fiber amplifiers. The balanced photodetector comprises a pair of

PDs as shown in inset of Figure 6.11 (a). The active area of each photodiode is 14×25 μm^2. The PDs were independently biased through a custom designed microwave probe that allowed the currents to be monitored separately (Figure 6.11 (b)). A lensed fiber array with approximately 2-μm-diameter spot size and 250-μm pitch was used to couple light into the two input waveguides. Taking the fiber-chip coupling loss of 12.8 dB into account, we estimated the internal responsivity to be 0.78 A/W at 1550 nm wavelength for a 25 μm long device. Both photodiodes in the balanced detector had < 200 nA dark current at 5 V reverse bias, which is shown in Figure 6.11 (a).

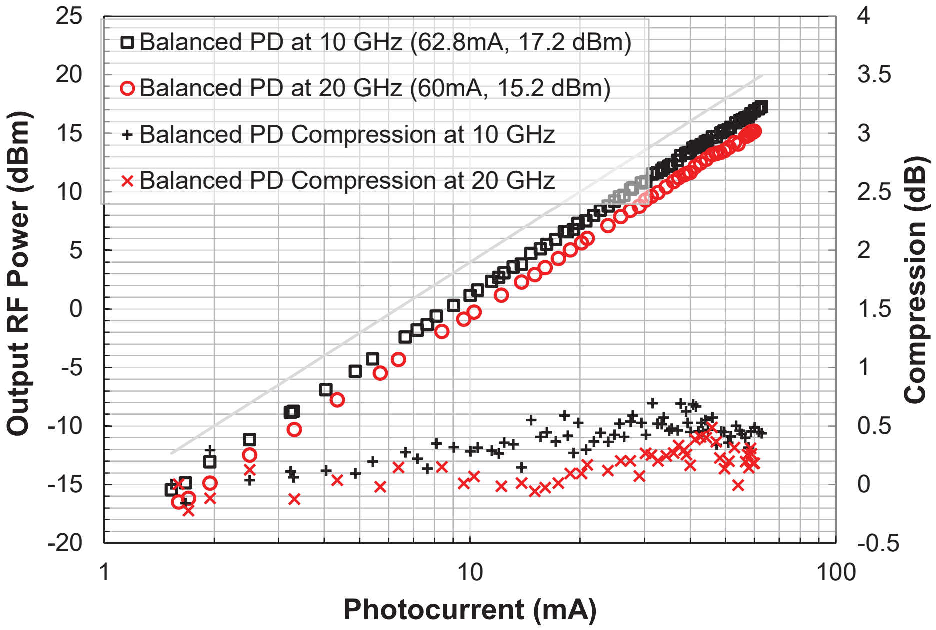

Figure 6.14 Output RF power of 14×25 μm^2 PD at +/-6 V bias voltage and power compression at 10 GHz and 20 GHz vs. average photocurrent.

To characterize the bandwidth and saturation current the optical heterodyne signal was split into two branches. A variable free-space delay line in one of the branches was used to control the modulation phase difference of the optical signal into both photodiodes and switch between common mode (i.e. zero phase difference) and differential mode (i.e. $(2n+1)\pi$ phase difference). A variable attenuator was adjusted to compensate the power imbalance that arises from the loss difference in the two optical branches (Figure 6.11 (b)). As shown in Figure 6.12, individual photodiodes with active area of $14 \times 25\ \mu m^2$ exhibited bandwidths of 15 GHz (circle) and 14 GHz (square) at +/-5 V bias under single element illumination. Note that these bandwidths are approximately half the bandwidths that would be expected for discrete photodiodes. The balanced photodetector demonstrated a bandwidth of 14 GHz in differential mode.

The capacitance of the balanced photodiode pair is twice that of the individual photodiodes. Since the bandwidth of the devices is RC-limited, the bandwidth of 350 μm^2 balanced photodiode pair is half of bandwidth of single devices with 350 μm^2 area. As a result of the symmetry provided by monolithic integration, a high common mode reject ratio (CMRRs) of ~ 30 dB at low frequency and > 20 dB at the 3 dB cut-off frequency were observed.

As expected, for the balanced detector operating in differential mode, the combined photocurrents of the two photodiodes exhibited ~ 6 dB higher output RF power than the output RF power from a single photodiode with the same per-diode-photocurrent. Figure 6.13 shows the RF output power at 10 GHz versus average photocurrent at room temperature and +/-6V bias voltage measured at 50 Ω external load. The maximum RF output power levels of the individual photodiodes were 11.5 dBm at 32.6 mA photocurrent and 11.1 dBm at 31.1 mA photocurrent. In differential mode the balanced detector exhibited 62.8 mA total photocurrent and 17.2 dBm output RF power. At 20 GHz, the maximum RF power was 15.2 dBm (Figure 6.14). It should be noted the maximum output power was eventually limited by the available input optical power of our experimental setup rather than photodiode saturation or thermal failure (the maximum input optical power is > 30 dBm). Figure 6.15 compares our results to waveguide photodiode RF output power levels that have been reported in the literatures [27, 100-108].

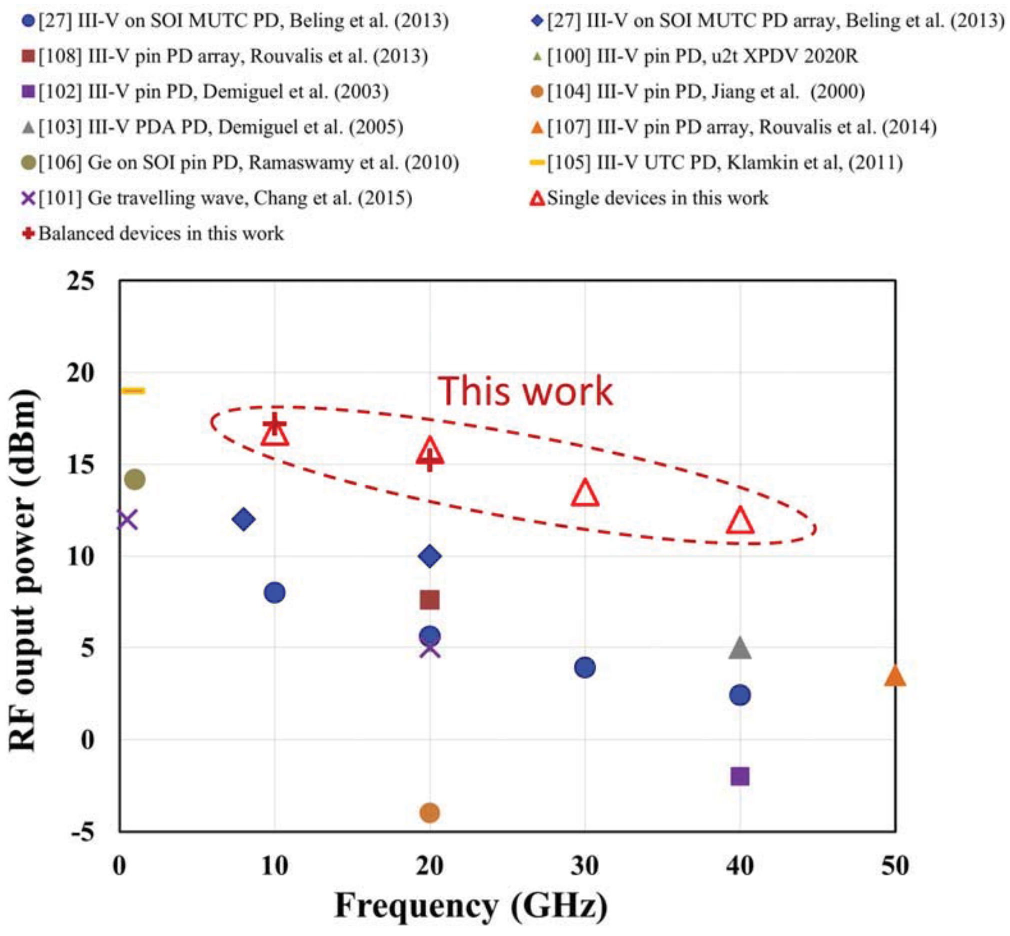

Figure 6.15 Output RF power of waveguide photodiodes versus modulation frequency at 1.55 μm wavelength that have been reported in the literatures.

6.4 Summary

In this chapter, modified uni-traveling carrier single and balanced photodiodes heterogeneously integrated on SOI waveguides were designed, fabricated and characterized. The internal responsivity was 0.64 A/W, 0.78 A/W and 0.95 A/W for 21 μm-, 25 μm- and 35 μm-long photodiodes, respectively. Single photodiodes reach up to 48 GHz bandwidth. The maximum output power levels were 16.6 dBm, 15.8 dBm, and 12 dBm at 10 GHz, 20 GHz and 40 GHz, respectively. Single photodiodes exceed a saturation current-bandwidth product of 1260 mA·GHz. Balanced photodiodes exhibit 14 GHz bandwidth and >20 dB common-mode rejection ratio. The unsaturated RF output power reaches 17.2 dBm at 10 GHz and 15.2 dBm at 20 GHz. These are the highest output power levels reported to date for any high-speed waveguide photodiode technology including photodiode arrays.

Chapter 7 Conclusions and Future Work

7.1 Conclusion

The main focus of my work has been to improve the RF power performance of the CC-MUTC photodiodes and to demonstrate their capabilities, e.g., the analog link that I developed and the study of high-power pulsed RF signals. As stated in previous chapters for high-power photodiodes, there are three major factors that limit the output power: the space charge effect, thermal failure and nonuniform absorption profile. The structure that first showed improved performance compared to PIN photodiodes is the UTC [30, 95, 105]. Colleagues in my group made modifications to the UTC structure that have reduced the space charge effect to the extent that thermal considerations are now the primary limiting factor [35, 78]. To reduce heating, a flip-chip bonding technique has been demonstrated [1, 38, 41, 55-57]. Initially, Si and then AlN were used as high-thermal-conductivity submounts. In this work, I have extended that approach using chemical-vapor-deposition (CVD) diamond [39]. The flip-chip bonded CC-MUTC photodiodes on diamond submounts exhibited record high output RF power of 1.8 W at 10 GHz and saturation photocurrent of 300 mA. Compared with previously reported “champion” results, the devices on diamond submounts achieve >80% higher RF output power. I have also used these photodiodes to demonstrate record power conversion efficiency of 50.7% to 60% at 6 to 10 GHz with ~ 27.8 dBm RF output power. The previous best efficiencies were <40 % in the same frequency band.

These high-power photodiodes were also used to demonstrate a high-gain, low-noise-figure, and high-linearity analog photonic link. The link combined a high-power and low-noise fiber laser, a Mach-Zehnder modulator, a high-gain erbium-doped fiber amplifier (EDFA), and a high-performance charge-compensated modified uni-traveling-carrier (CC-MUTC) photodiode. In the link, low biasing was utilized to reduce the noise and maximize the signal-to-noise ratio and an EDFA was used to provide sufficient optical input to the MUTC photodiode to ensure that high gain and high output RF power were achieved.

Optical generation of high-power pulsed microwave signals was demonstrated. The impulse response without RF modulation achieved unsaturated peak voltage of 33.5 V and full width at half maximum (FWHM) of 50 ps. The peak power levels for gated modulation at 1 GHz and 10 GHz were 41.5 dBm (14.2 W) and 40 dBm (10 W), respectively.

InP-based high-power and high-speed modified uni-traveling carrier photodiodes heterogeneously integrated on silicon-on-insulator (SOI) waveguides have also been demonstrated. Single devices can exhibit either an internal responsivity up to 0.95 A/W or a bandwidth up to 48 GHz. The maximum RF output power of a 20×35 μm^2 photodiode was 16.6 dBm, 15.8 dBm and 13.5 dBm at 10 GHz, 20 GHz and 30 GHz, respectively. The maximum output RF power of a 10×35 μm^2 photodiode was 12 dBm at 40 GHz. Using the same integration technology we show that balanced waveguide photodiodes reach 0.78 A/W internal responsivity, 14 GHz bandwidth, and >20 dB common-mode rejection ratio (CMRR). In differential mode the unsaturated RF output power was 17.2 dBm at 10 GHz and 15.2 dBm at 20 GHz.

7.2 Future Work

7.2.1 Heterogeneously integrated waveguide photodiodes on SOD

7.2.1.1 Introduction

In Chapter 6, I have discussed evanescently-coupled waveguide photodiodes heterogeneously integrated on silicon-on-insulator (SOI). By optimizing the photodiode structure, the space charge effect and nonuniform absorption have been reduced. The output power is limited by thermal failure due to the poor thermal conductivity of SiO_2. For silicon photonic devices, 1 μm-thick or thicker BOX layer is required to reduce the optical leakage loss to the silicon substrate. However, the thicker BOX layer prevents heat generated in or on top of SOI waveguide from being extracted by the substrate cooling in device such as hybrid silicon lasers and amplifier [109-111]. Recently, diamond has been considered as a promising material for both electronic and photonic devices primarily due to its electrical insulation and mechanic hardness. As mentioned in Chapter 3, diamond has maximum thermal conductivity of 1000 ~ 1800 W/mK, the highest value in natural materials [39]. Figure 7.1 (a) shows a silicon-on-diamond (SOD) substrate consisting of a 700 nm-thick silicon device layer and 2 μm-thick buried CVD diamond layer [99]. The propagation losses for SOD and SOI waveguides are 0.74 dB/cm. The coupling loss of SOD waveguides is 10.6 dB/facet [99].

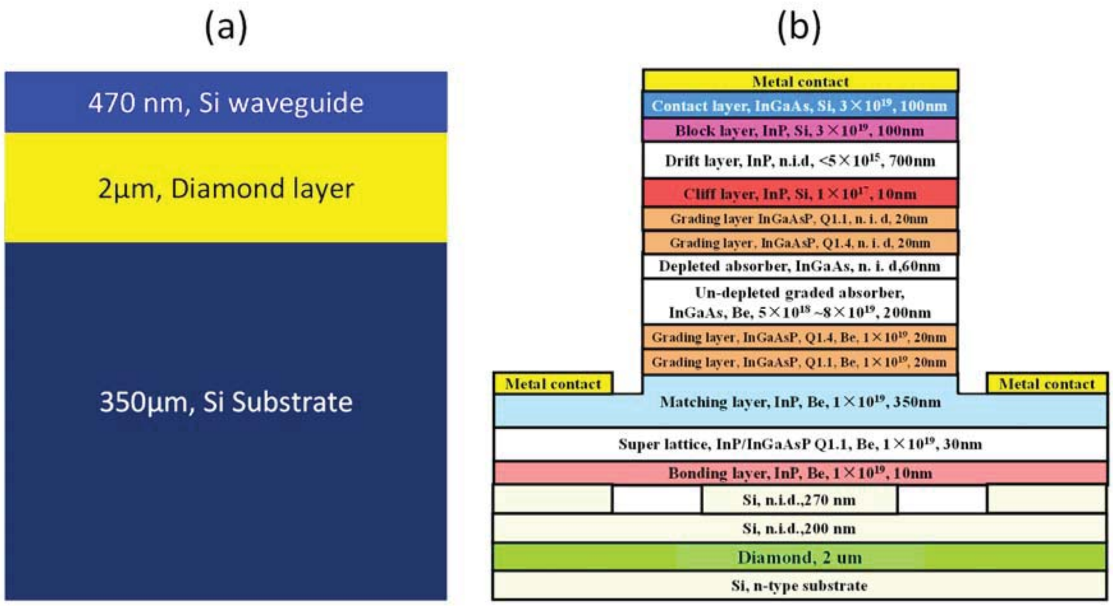

Figure 7.1 (a) Cross-section of SOD waveguide wafer. (b) cross-section of waveguide photodiode on SOD wafer.

In this work, the III-V photodiode material dies were plasma activated and bonded at room temperature to the Si waveguide layer by Aurrion Inc. A schematic cross-section of the waveguide photodiode on SOD wafer is shown in Figure 7.1 (b). The photodiode fabrication process has been described in Chapter 6 and described in Figure 6.2.

7.2.1.2 Dry Etch SOD Wafer

After finishing the waveguide/photodiode on SOD fabrication, I measured the dark current of devices that will be shown in the following. In this section, I will discuss how to dice the SOD wafer. Since there is not any grating coupler design on the SOD wafers, the SOD wafers have to be diced to enable light coupling from the dicing facet. However, as we know, diamond is one of the hardest materials, which leads to another problem: how to dice the SOD wafer. First I tried to dice a SOD dummy wafer by using conventional Disco blades. Figure 7.2 (a) and (b) shows the dicing results using ZH05 serial blade and R07 serial blade, respectively. It can be observed that the ZH05 serial blade causes the Si waveguide layer to peel off the diamond layer. For the R07 blade, the facet is rough. Therefore I developed a process to dice the SOD wafer with a smooth facet. The process involves two steps: the first step is to etch through the 2-μm diamond layer using a dry etch; the second step is to dice the underlying Si substrate. The complete process flow is shown in Figure 7.3.

In order to etch the 2-μm thick diamond layer, a strong dry etch recipe has to be applied. First a 1.5-μm thick Al is deposited on the wafer as hard mask for diamond dry etching. A poly layer (FUJI Durimide 20-1.2 μm: 0.4 μm) is used to insulate the Al hard mask and the Au pads on wafer shown in Figure 7.3 (a). AZ5214 photoresist is patterned by conventional lithography and then the pattern is transferred from the photoresist to the

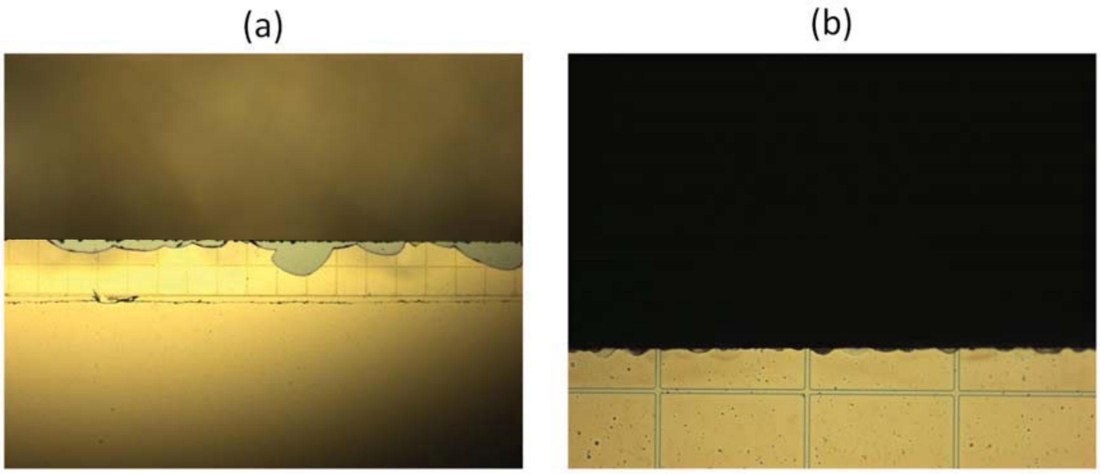

Figure 7.2 Dicing facet by using ZH05 serial blade (a) and R07 serial blade (b).

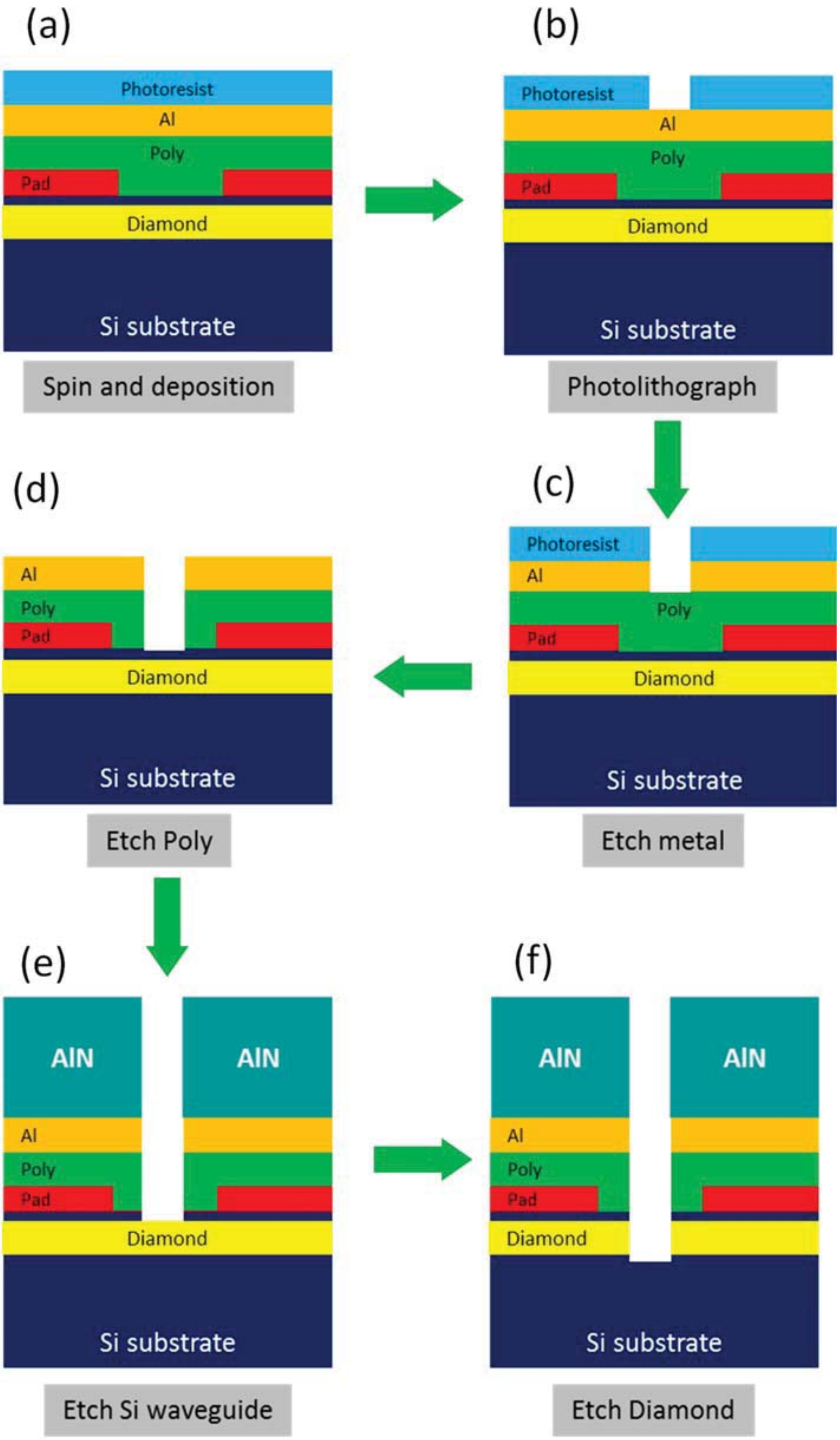
(a)
Photoresist
Al
Poly
Pad
Diamond
Si substrate
Spin and deposition
(b)
Photoresist
Al
Poly
Pad
Diamond
Si substrate
Photolithograph
(c)
Photoresist
Al
Poly
Pad
Diamond
Si substrate
Etch metal
(d)
Al
Poly
Pad
Diamond
Si substrate
Etch Poly
(e)
AlN
AlN
Al
Poly
Pad
Diamond
Si substrate
Etch Si waveguide
(f)
AlN
AlN
Al
Poly
Pad
Diamond
Si substrate
Etch Diamond

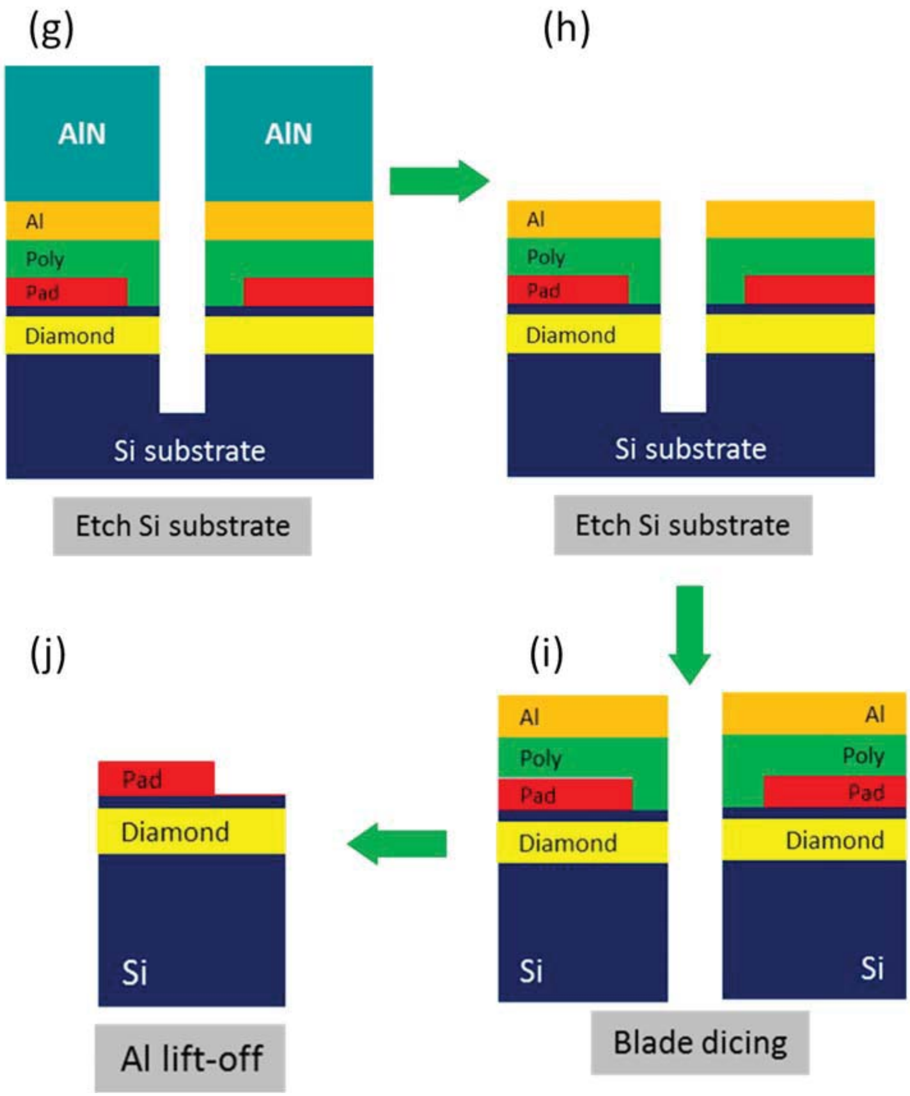

Figure 7.3 Process flow of dry etch and blade dice SOD wafer.

Al hard mask by Al dry etching in the Oxford. This is illustrated in Figure 7.3 (a) – (c). The recipe for Al dry etching is Cl_2 (5 sccm):BCl_3 (40 sccm) gas mixture at 20 °C and 50 mTorr pressure. The forward power is set to 100 W. The Al etch rate is 200 nm/min. Following the Al dry etch, the poly layer is etched using an oxygen plasma as shown in Figure 7.3 (d). However, it was found that after poly etching, the edge of the pads and the

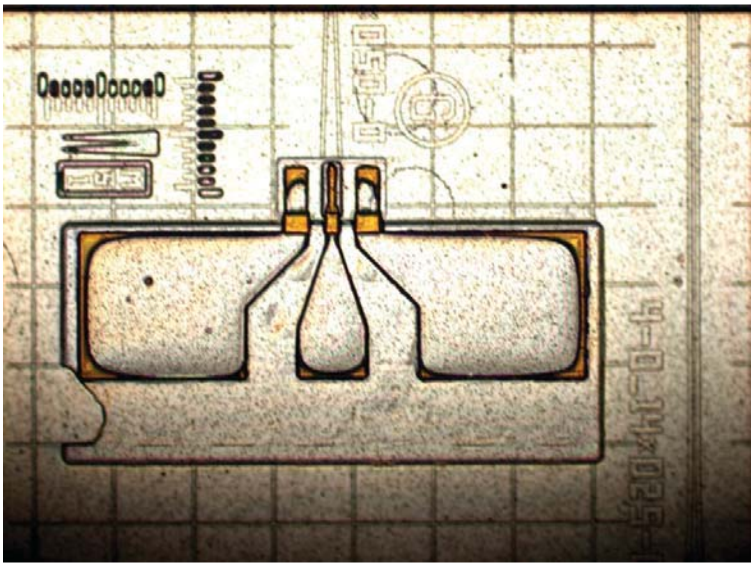

Figure 7.4 Microscope photo after poly etch.

air bridge are exposed since the thin poly layer is thin at the edge of pads and the air bridge. This is shown in Figure 7.4.

In order to prevent the pad and air bridge from etching away, I propose to use an AlN submount to cover the active photodiode and RF pad. The AlN submount will be flip-chip bonded on the wafer using black wax as shown in Figure 7.5. Owing to the "strong hard mask" of the AlN submount, the active photodiode and RF pads can be protected during the following Si dry etch and the diamond dry etch. The process flow for Si dry etching and diamond dry etching is shown in Figure 7.3 (e), (f) and (g). After removing the AlN submount, the etched wafer will be diced using a conventional blade (ZH05 serial blade). The whole process will be finalized by doing an Al lift-off. The diced wafer will be immersed in NMP solution on a 120 °C hot plate to soften the poly layer and then the Al layer can be removed.

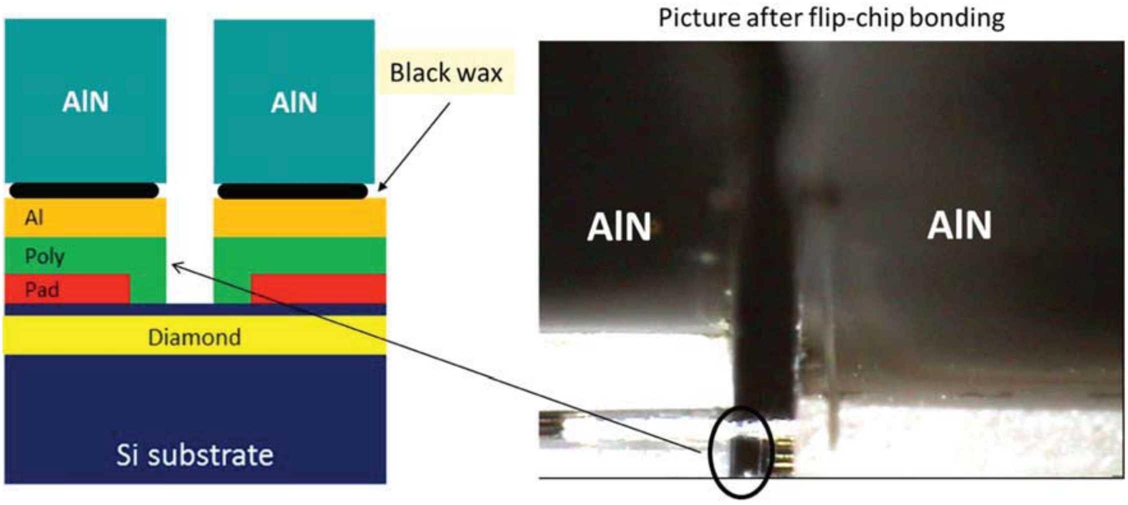

Figure 7.5 Schematic cross-section (left) and microscope photo after flip-chip bonding (right).

7.2.1.3 Experimental results

Figure 7.6 (a) shows typical measured current-voltage curves. The dark currents is ~ 10 nA at 5 V reverse bias. The optical heterodyne setup was used to measure the bandwidth. As shown in Figure 7.6 (b), photodiodes with active areas of 14×150 μm^2, 14×100 μm^2, 14×50 μm^2 and 14×25 μm^2 exhibited bandwidths of 7 GHz, 11 GHz, 17 GHz and 25 GHz, respectively. Figure 7.7 summarizes the measured bandwidths from all tested devices. The blue line is the measured capacitance of all tested devices. The red line shows the calculated RC-limited bandwidth of single devices on SOI based on C-V measurements. The purple diamond points represent the bandwidths of measured devices on SOI. The fact that the measured bandwidths approach the calculations indicates that

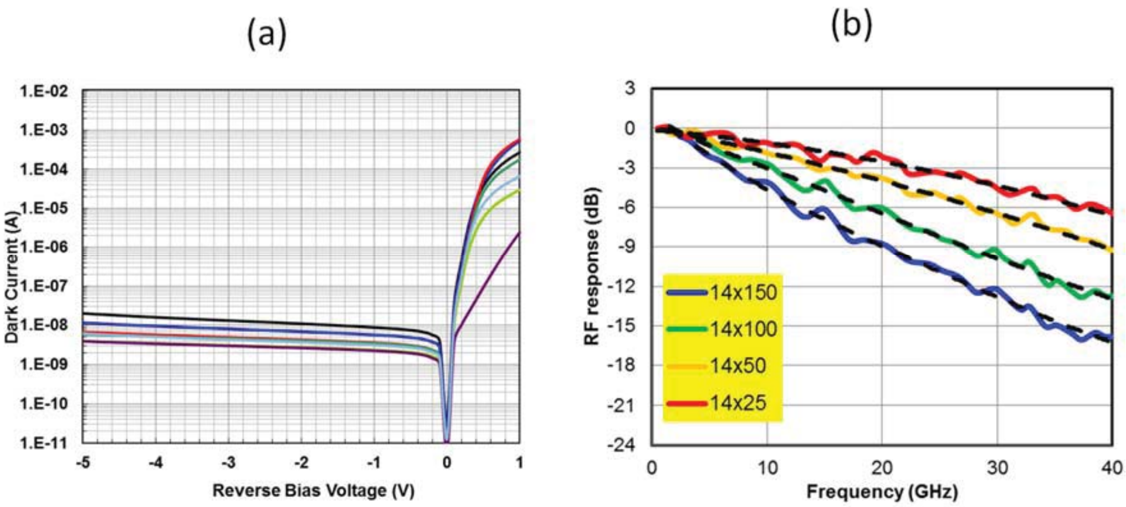

Figure 7.6 (a) Measured dark currents of single MUTC PDs on SOD, (b) frequency responses of 14×150 μm², 14×100 μm², 14×50 μm² and 14×25 μm² waveguide MUTC PDs measured at -8 V bias voltage (dashed lines are smoothed data).

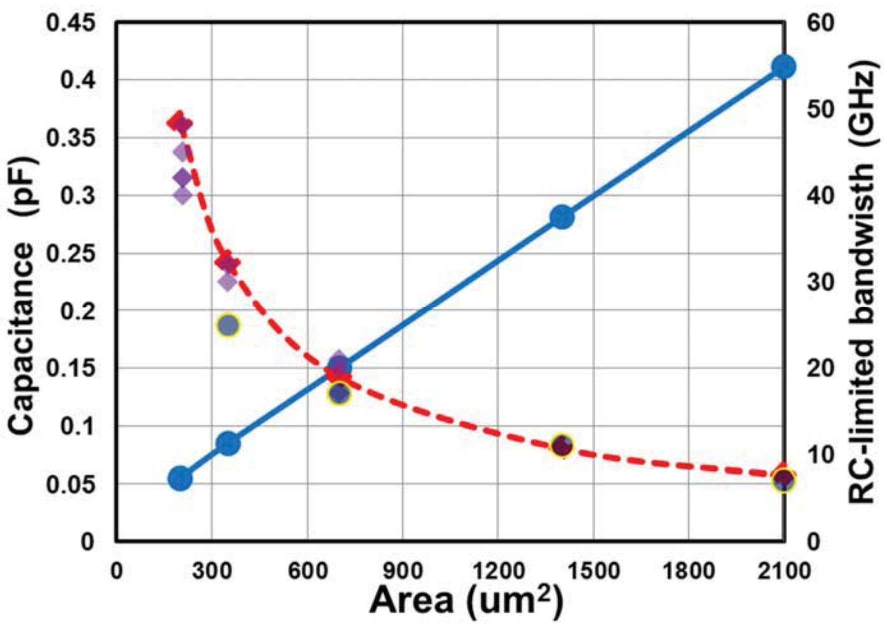

Figure 7.7 Measured bandwidths of different sized photodiodes and calculated RC-bandwidth based on C-V measurement.

the bandwidth is primarily limited by the RC-time constant. The light black circle dots are the bandwidths of single devices on SOD. The bandwidth of devices on SOD fits the RC-limited bandwidth well for the devices with large area while the bandwidth of the devices with small area deviates from the estimated RC-limited bandwidth of devices on SOI. This agrees with the measured I-V curve shown in Figure 7.6 (a). The resistance of devices with small area is relatively large compared with those of the large devices. Therefore the bandwidth of small devices is limited by large resistance.

7.2.1.4 Summary

In this section, MUTC photodiodes heterogeneously integrated on SOD waveguides were designed, fabricated and characterized. The typical dark current of single devices is ~10 nA at -5 V bias voltage. Single photodiodes reach up to 25 GHz bandwidth. However, the devices are still limited by coupling loss due to rough waveguide input facet. The next step is to polish the input facet by using a focused ion beam.

7.2.2 Heterogeneously integrated taper-waveguide-coupled photodiodes

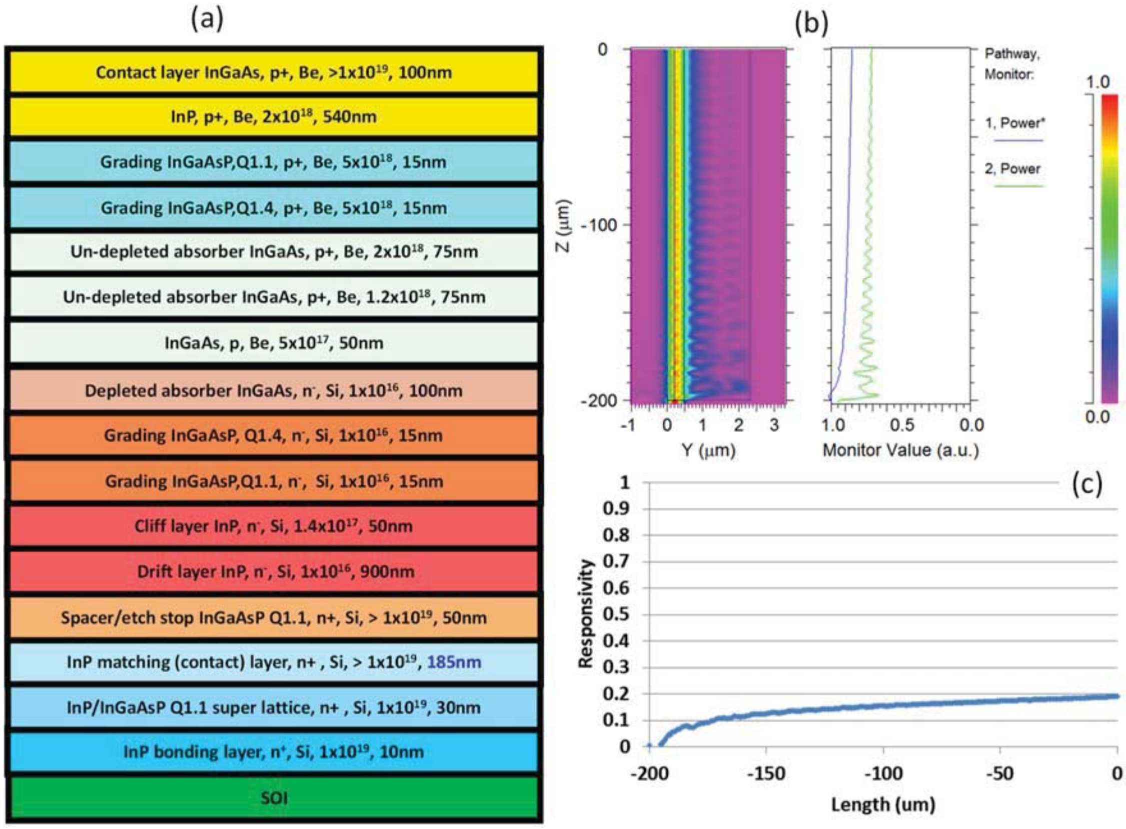

Figure 7.8 (a) Cross-section of MUTC PD on SOI. Doping concentrations in cm^{-3}, (b) simulated optical power distribution, and (c) responsivity versus length of photodiode.

For my current work on heterogeneously integrated waveguide photodiodes, the absorption layer is close to waveguide layer as shown in Figure 6.1 (a) and Figure 7.1 (b). In order to be compatible with the process flow of Aurrion Inc., with whom we collaborate, we changed our structure to that shown in Figure 7.8 (a). In this structure, the light passes across the 900 nm drift layer before reaching the absorption layer. This reduces the responsivity in a conventional waveguide structure. Figure 7.8 (b) and (c)

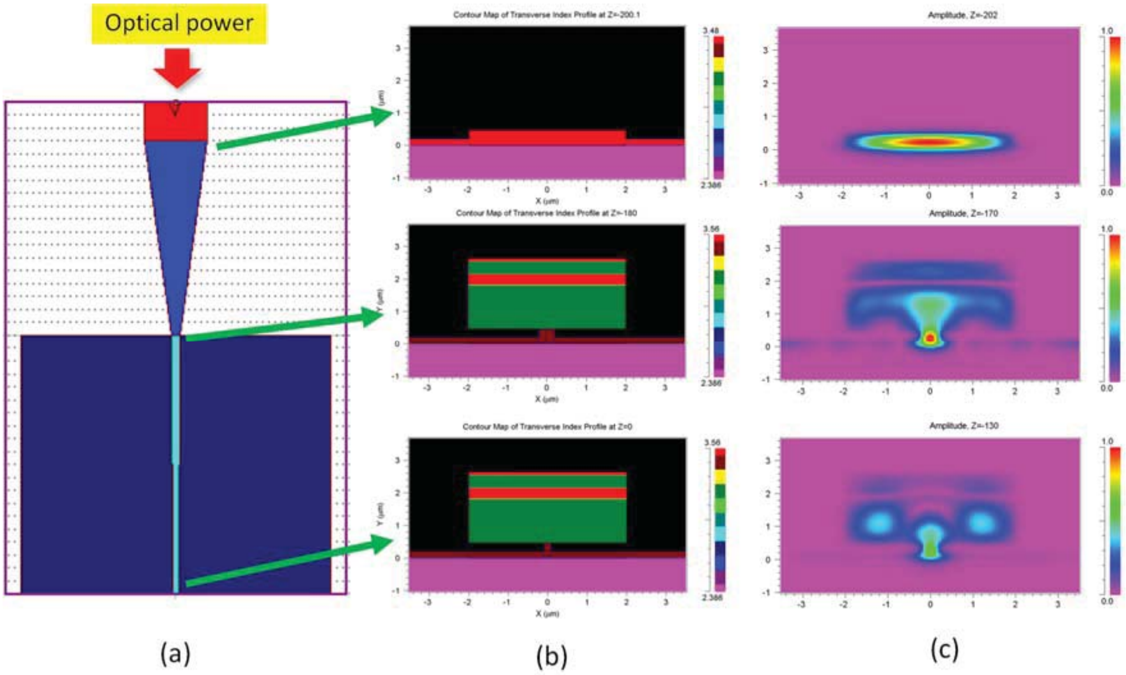

Figure 7.9 (a) Top view of waveguide photodiode on SOI. Red part, light blue part, cyan part and dark blue part represent input waveguide with 2 μm width, tapered waveguide from 2 μm width to 0.2 μm width, waveguide underneath III-V layers and III-V layers, respectively. (b) Cross-section plot of three different positions along waveguide and (c) the corresponding optical power file on the cross-section planes.

shows the optical power distribution and responsivity of the new structure with a conventional waveguide. Most of optical power is still in the waveguide and not absorbed by absorption layer. The responsivity is ~ 0.2 A/W for 200-μm-long devices. In order to improve the responsivity, a tapered waveguide can be to couple the optical power up to the absorption layer as shown in Figure 7.9. As a result, the responsivity can be improved from 0.2 A/W to 1.2 A/W for 200-μm long devices.

One concern about the taper-coupled waveguide is that the optical power is concentrated at the center of the cross-section (Figure 7.10 (a)). This will lead to local saturation, which limits the output RF power. In order to get a uniform optical absorption profile, I propose to introduce a tapered waveguide array similar to that shown in Figure 7.10 (b). The optical distribution of the tapered waveguide array is much more uniform compared with a single tapered waveguide.

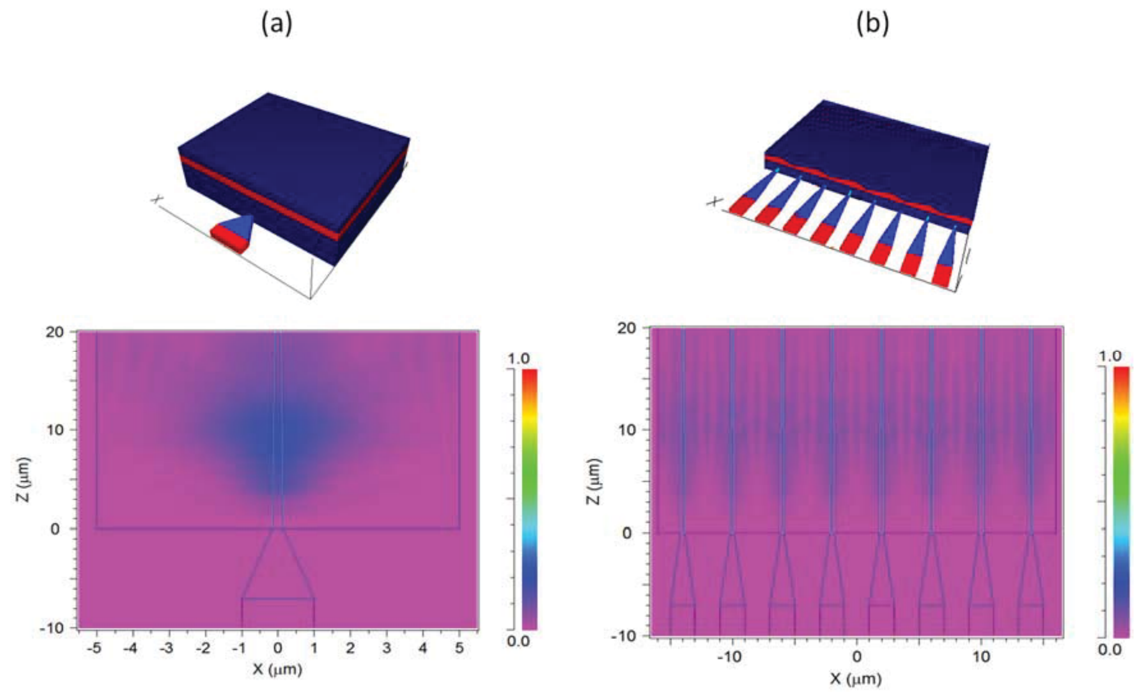

Figure 7.10 Optical power distributions in the absorption layer of the devices with (a) a single taper and (b) a taper array.

7.2.3 AM-PM conversion schematic of MUTC photodiodes

For high power photodiodes, one of the most important applications is to generate ultra-low phase noise RF signals for antenna synchronization of radio-astronomy, optical clock comparison in metrology, and photonic analog-to-digital conversion. Photodetectors are critical parts of the chain in all these applications. At present, the phase noise of a mode locked laser can be maintained as a low level but the amplitude noise of laser can be transformed to phase noise on the electrical signal by photo-detection [112]. Our high-power photodiodes exhibit low AM to PM conversion. Figure 11 summarized the AM to PM characteristics. In the figure, the most interesting feature is

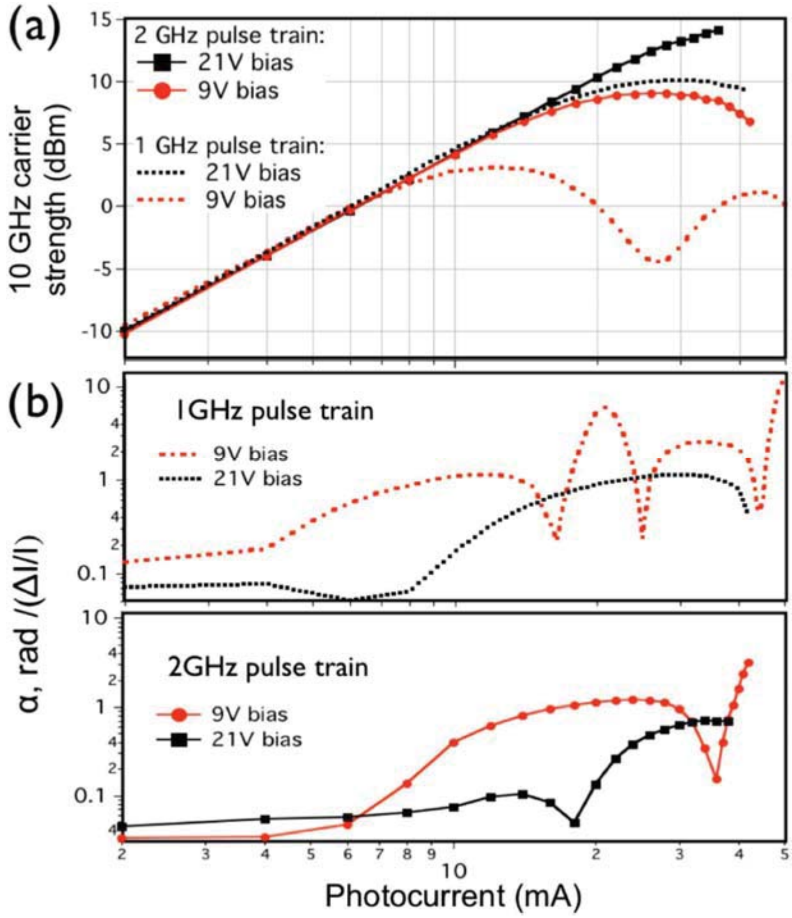

Figure 7.11 Saturation and AM–PM measured for a 10 GHz carrier obtained from MUTC PD with 1 ps pulses at 980 nm from a mode-locked laser. α is the rms 10 GHz phase variation per fractional change in the photocurrent (ΔI/I) [10].

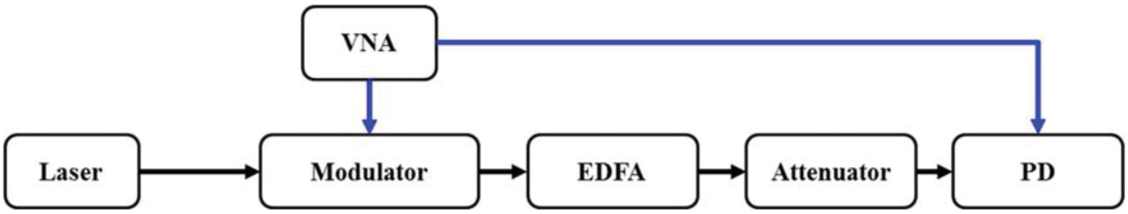

Figure 7.12 Experimental setup of AM-PM analysis.

the presence of multiple nulls in the measured AM to PM. This could indicate that there are competing power-dependent processes cancel at specific photocurrents.

The phase distortion in an MUTC photodiode can be characterized in the CW mode. A one-tone AM-PM analysis similar to the one used for amplifiers [113] can be implemented using the Keysight analyzer. Figure 7.12 shows the experimental setup of the AM-PM measurement apparatus. Figure 7.13 shows power and phase of the fundamental signal and the 3rd harmonic signal versus average photocurrent. The frequency of the fundamental signal is 1 GHz and bias voltage applied to the photodiode is 0 V. The power and phase of the fundamental signal and the third harmonic signal are different within different photocurrent ranges. I have divided the plot to the four ranges shown in Figure 7.13. In the first region the phase of the fundamental signal drops from 0 to -5° due to the phase drop of the third harmonic from 0 to 180° as shown in Figure 7.13 (b). In the second region the phase drop of fundamental signal slows down and then the phase of the fundamental signal starts to increase since the sign of the phase of the third harmonic changes and the power of third harmonic increases (the first NULL AM-PM point). In the third region the phase of the third harmonic changes from -180° to -360 ° and the phase of the fundamental signal increases and peaks between regions 3 and 4. In the fourth region the sign of the phase of the third harmonic changes (the second NULL AM-PM point). Further study is planned in order to shed light on these relationships.

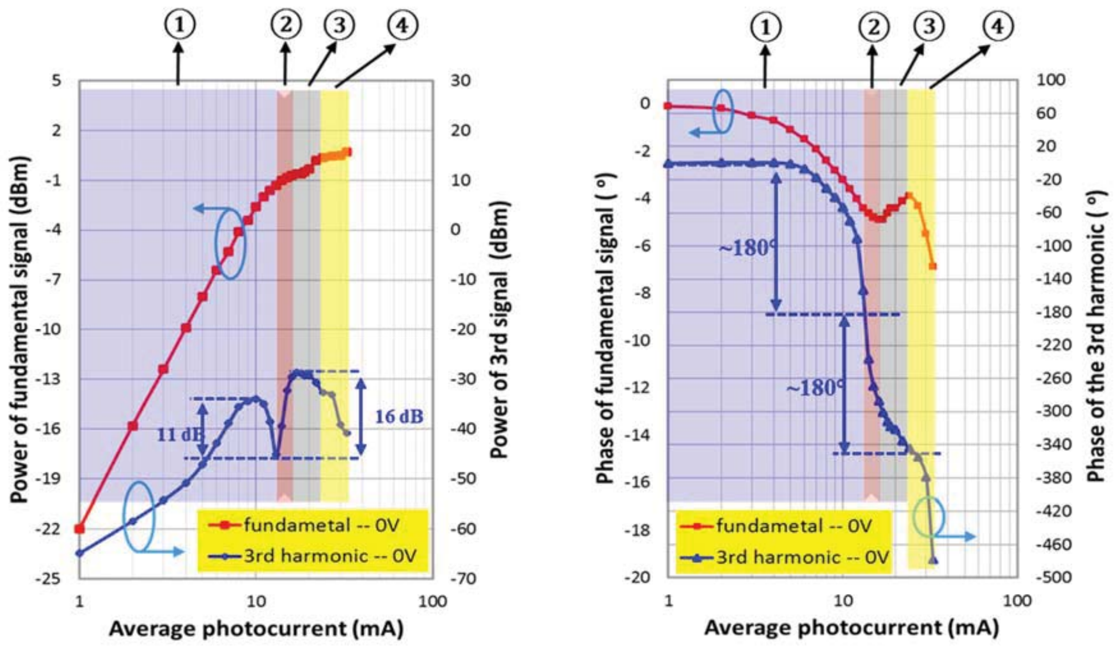

Figure 7.13 (left) Power and (right) phase of fundamental signal and 3rd harmonic signal vs average photocurrent.

7.2.4 100 GHz high-power heterogeneously integrated photodiodes on SOI

An ultrafast and high-output photodetector that operates at long wavelengths is required for various applications, such as high bit rate fiber optic communications and ultrafast measurements. Figure 7.14 shows the structure of a 100 GHz high-power heterogeneously integrated photodiode. In order to achieve 100 GHz bandwidth, the thickness of the drift layer is set to 300 nm to reduce the transit time. A 20-nm cliff layer is used to increase the electric field in the un-depleted drift layer to mitigate space charge effect. Figure 7.15 shows the simulated responsivity for absorption layer and InP contact layer with different thickness. When the absorption layer is 200 μm thick, the responsivity is 0.9 A/W and 1.2 A/W for 10-μm long and 20-μm long photodiodes. Future work will need to address mask design and inductive peaking design.

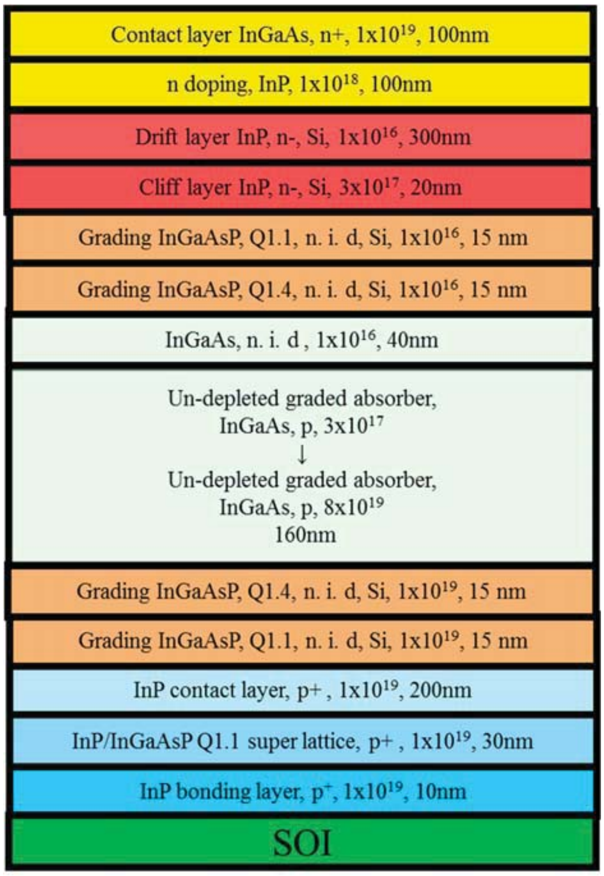

Figure 7.14 Structure of 100 GHz photodiode.

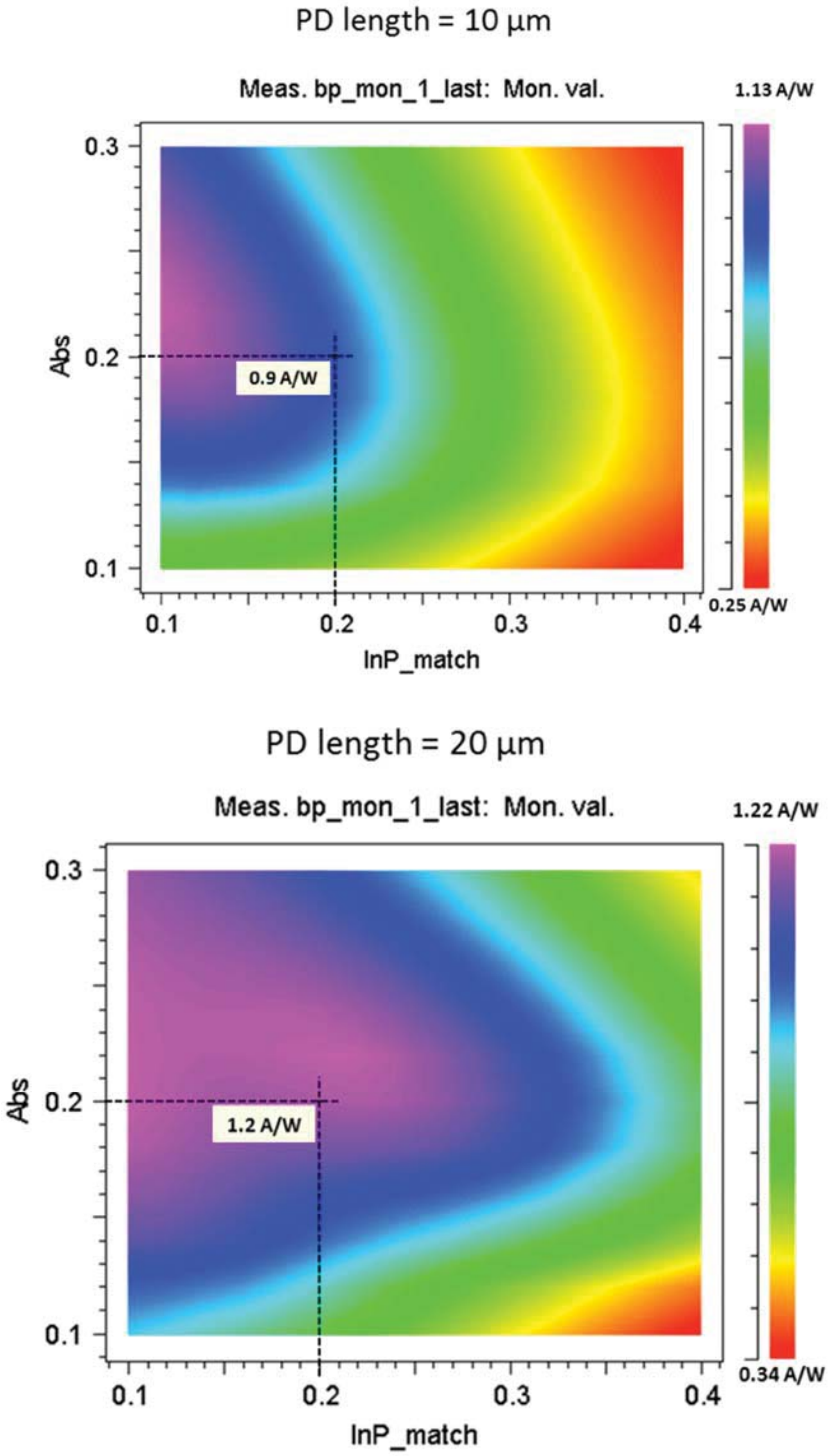

Figure 7.15 Responsivity simulations of 10-um-long and 20-um-long devices.

Bibliography

1. Zhou, Q., et al. *Development of narrowband modified uni-travelling-carrier photodiodes with high power efficiency*. in *Avionics, Fiber-Optics and Photonics Conference (AVFOP), 2013 IEEE*. 2013. IEEE.
2. Gasulla, I., et al., *Recent Breakthroughs in Microwave Photonics.* IEEE Photonics Journal, 2011. **3**(2): p. 311-315.
3. Capmany, J., I. Gasulla, and S. Sales, *Microwave photonics: Harnessing slow light.* Nature Photonics, 2011. **5**(12): p. 731-733.
4. Kao, K. and G.A. Hockham. *Dielectric-fibre surface waveguides for optical frequencies*. in *Proceedings of the Institution of Electrical Engineers*. 1966. IET.
5. Gambling, W.A., *The rise and rise of optical fibers.* IEEE Journal of Selected Topics in Quantum Electronics, 2000. **6**(6): p. 1084-1093.
6. Zhou, X., L.E. Nelson, and P. Magill, *Rate-Adaptable Optics for Next Generation Long-Haul Transport Networks.* IEEE Communications Magazine, 2013. **51**(3): p. 41-49.
7. Breuer, D., et al., *Opportunities for Next-Generation Optical Access.* IEEE Communications Magazine, 2011. **49**(2): p. S16-S24.
8. Yao, J.P., *Microwave Photonics.* Journal of Lightwave Technology, 2009. **27**(1-4): p. 314-335.

9. Urick, V.J., et al., *Long-Haul Analog Photonics.* Journal of Lightwave Technology, 2011. **29**(8): p. 1182-1205.

10. Fortier, T.M., et al., *Photonic microwave generation with high-power photodiodes.* Opt Lett, 2013. **38**(10): p. 1712-4.

11. Jacobs, E., et al. *Considerations for application of RF-over-fiber to navy systems*. in *Avionics, Fiber-Optics and Photonics Technology Conference, 2007 IEEE*. 2007. IEEE.

12. Pappert, S.A., et al. *Photonic link technology for shipboard RF signal distribution*. in *SPIE's International Symposium on Optical Science, Engineering, and Instrumentation*. 1998. International Society for Optics and Photonics.

13. Ghelfi, P., et al., *A fully photonics-based coherent radar system.* Nature, 2014. **507**(7492): p. 341-5.

14. Walden, R.H., *Analog-to-Digital Conversion in the Early Twenty-First Century.* Wiley Encyclopedia of Computer Science and Engineering, 2008.

15. Serafino, G., et al. *Stable optically generated RF signals from a fibre mode-locked laser*. in *2010 IEEE Photinic Society's 23rd Annual Meeting*. 2010.

16. Juodawlkis, P.W., et al., *Optically sampled analog-to-digital converters.* IEEE Transactions on Microwave Theory and Techniques, 2001. **49**(10): p. 1840-1853.

17. Wootten, A. and A.R. Thompson, *The Atacama Large Millimeter/Submillimeter Array.* Proceedings of the IEEE, 2009. **97**(8): p. 1463-1471.

18. Marpaung, D., et al., *Integrated microwave photonics.* Laser & Photonics Reviews, 2013. **7**(4): p. 506-538.

19. Roelkens, G., et al. *III-V/silicon photonic integrated circuits for communication applications*. in *Opto-Electronics and Communications Conference (OECC), 2011 16th*. 2011. IEEE.

20. Liang, D., et al., *Hybrid Integrated Platforms for Silicon Photonics.* Materials, 2010. **3**(3): p. 1782-1802.

21. Beling, A. and J.C. Campbell, *InP-Based High-Speed Photodetectors.* Journal of Lightwave Technology, 2009. **27**(1-4): p. 343-355.

22. Kato, K., *Ultrawide-band/high-frequency photodetectors.* IEEE Transactions on Microwave Theory and Techniques, 1999. **47**(7): p. 1265-1281.

23. Bowers, J.E. and C. Burrus, *High-speed zero-bias waveguide photodetectors.* Electronics letters, 1986. **22**(17): p. 905-906.

24. Li, X.W., et al., *High-saturation-current InP-InGaAs photodiode with partially depleted absorber.* IEEE Photonics Technology Letters, 2003. **15**(9): p. 1276-1278.

25. Williams, K.J. and R.D. Esman, *Design considerations for high-current photodetectors.* Journal of Lightwave Technology, 1999. **17**(8): p. 1443-1454.

26. Unterborsch, G., et al. *High-power performance of a high-speed photodetector*. in *Optical Communication, 1998. 24th European Conference on*. 1998. IEEE.

27. Beling, A., et al., *InP-based waveguide photodiodes heterogeneously integrated on silicon-on-insulator for photonic microwave generation.* Opt Express, 2013. **21**(22): p. 25901-6.

28. Xie, X., et al. *Heterogeneously Integrated Waveguide-Coupled Photodiodes on SOI with 12 dBm Output Power at 40 GHz*. in *Optical Fiber Communication Conference*. 2015. Optical Society of America.

29. Effenberger, F.J. and A.M. Joshi, *Ultrafast, dual-depletion region, InGaAs/InP pin detector.* Lightwave Technology, Journal of, 1996. **14**(8): p. 1859-1864.

30. Ishibashi, T., et al., *High-speed response of uni-traveling-carrier photodiodes.* Japanese Journal of Applied Physics Part 1-Regular Papers Brief Communications & Review Papers, 1997. **36**(10): p. 6263-6268.

31. Nagatsuma, T., H. Ito, and T. Ishibashi, *High-power RF photodiodes and their applications.* Laser & Photonics Reviews, 2009. **3**(1-2): p. 123-137.

32. Cheng, Y.-h., *High-Speed, High-Efficiency, and Large-Area pin Photodiode for the Applications of Optical Interconnect from 0.85 to 1.55 um Wavelengths.* 2013.

33. Shi, J.-W., F.-M. Kuo, and J.E. Bowers, *Design and Analysis of Ultra-High-Speed Near-Ballistic Uni-Traveling-Carrier Photodiodes Under a 50-Load for High-Power Performance.* Photonics Technology Letters, IEEE, 2012. **24**(7): p. 533-535.

34. Li, N., et al., *High-saturation-current charge-compensated InGaAs-InP uni-traveling-carrier photodiode.* IEEE Photonics Technology Letters, 2004. **16**(3): p. 864-866.

35. Li, Z., et al., *High-Saturation-Current Modified Uni-Traveling-Carrier Photodiode With Cliff Layer.* IEEE Journal of Quantum Electronics, 2010. **46**(5): p. 626-632.

36. Wang, X., et al., *InGaAs–InP photodiodes with high responsivity and high saturation power.* Photonics Technology Letters, IEEE, 2007. **19**(16): p. 1272-1274.

37. Li, Z., *High-power Photodiodes*, in *Electrical and Computer Engineering*. 2011, University of Virginia. p. 86.

38. Li, Z., et al., *High-power high-linearity flip-chip bonded modified uni-traveling carrier photodiode.* Opt Express, 2011. **19**(26): p. B385-90.

39. Coe, S.E. and R.S. Sussmann, *Optical, thermal and mechanical properties of CVD diamond.* Diamond and Related Materials, 2000. **9**(9-10): p. 1726-1729.

40. Duan, N., et al., *Thermal analysis of high-power InGaAs-InP photodiodes.* IEEE Journal of Quantum Electronics, 2006. **42**(11-12): p. 1255-1258.

41. Beling, A., et al. *High-power flip-chip balanced photodetector with> 40 GHz bandwidth*. in *Photonics Conference (IEEE, 2013)*. 2013.

42. Chtioui, M., et al., *High-power high-linearity uni-traveling-carrier photodiodes for analog photonic links.* IEEE Photonics Technology Letters, 2008. **20**(1-4): p. 202-204.

43. Chtioui, M., et al. *High power UTC photodiodes design and application for analog fiber optic links*. in *Microwave Photonics, 2009. MWP'09. International Topical Meeting on*. 2009. IEEE.

44. Cross, A.S., et al., *High-power flip-chip mounted photodiode array.* Opt Express, 2013. **21**(8): p. 9967-73.

45. Gliese, U., et al. *53.5% photodiode RF power conversion efficiency*. in *National Fiber Optic Engineers Conference*. 2010. Optical Society of America.

46. Itakura, S., et al., *High-Current Backside-Illuminated Photodiode Array Module for Optical Analog Links.* Journal of Lightwave Technology, 2010. **28**(6): p. 965-971.

47. Li, X., et al., *Backside illuminated high saturation current partially depleted absorber photodetecters.* Electronics Letters, 2003. **39**(20): p. 1466-1467.

48. Nagatsuka, T., et al. *High-power microwave photodiode array for radio over fiber applications*. in *OECC/ACOFT 2008-Joint Conference of the Opto-Electronics and Communications Conference and the Australian Conference on Optical Fibre Technology*. 2008.

49. Nagatsuma, T., et al. *All optoelectronic generation and detection of millimeter-wave signals*. in *Microwave Photonics, 1998. MWP'98. International Topical Meeting on*. 1998. IEEE.

50. Rouvalis, E., et al., *High-Power and High-Linearity Photodetector Modules for Microwave Photonic Applications.* Journal of Lightwave Technology, 2014. **32**(20): p. 3810-3816.

51. Sakai, K., et al., *High-current back-illuminated partially depleted-absorber pin photodiode with depleted nonabsorbing region.* Microwave Theory and Techniques, IEEE Transactions on, 2010. **58**(11): p. 3154-3160.

52. Shimizu, N., et al., *RF saturation mechanism of InP/InGaAs uni-travelling-carrier photodiode.* Electronics Letters, 2000. **36**(8): p. 750-751.

53. Tulchinsky, D.A., et al., *High-current photodetectors as efficient, linear, and high-power RF output stages.* Journal of Lightwave Technology, 2008. **26**(1-4): p. 408-416.

54. Tulchinsky, D.A., et al., *High-saturation current wide-bandwidth photodetectors.* IEEE Journal of Selected Topics in Quantum Electronics, 2004. **10**(4): p. 702-708.

55. Zhou, Q., et al. *High-power high-bandwidth flip-chip bonded modified uni-traveling carrier photodiodes*. in *IEEE Photonics Conference 2012*. 2012.

56. Zhou, Q.G., et al., *High-Power V-Band InGaAs/InP Photodiodes.* IEEE Photonics Technology Letters, 2013. **25**(10): p. 907-909.

57. Zhou, Q.G., et al., *Balanced InP/InGaAs Photodiodes With 1.5-W Output Power.* IEEE Photonics Journal, 2013. **5**(3): p. 6800307-6800307.

58. Bahl, I., *Fundamentals of RF and microwave transistor amplifiers*. 2009: John Wiley & Sons.

59. Ackerman, E.I., et al., *Input impedance conditions for minimizing the noise figure of an analog optical link.* IEEE Transactions on Microwave Theory and Techniques, 1998. **46**(12): p. 2025-2031.

60. Ackerman, E., et al. *Signal-to-noise performance of two analog photonic links using different noise reduction techniques*. in *Microwave Symposium, 2007. IEEE/MTT-S International*. 2007. IEEE.

61. Farwell, M.L., W.S.C. Chang, and D.R. Huber, *Increased Linear Dynamic-Range by Low Biasing the Mach-Zehnder Modulator.* IEEE Photonics Technology Letters, 1993. **5**(7): p. 779-782.

62. Karim, A. and J. Devenport, *Noise figure reduction in externally modulated analog fiber-optic links.* IEEE Photonics Technology Letters, 2007. **5**(19): p. 312-314.

63. Ackerman, E., et al. *Balanced receiver external modulation fiber-optic link architecture with reduced noise figure*. in *IEEE MTT S INTERNATIONAL MICROWAVE SYMPOSIUM DIGEST*. 1993. INSTITUTE OF ELECTRICAL ENGINEERS INC (IEEE).

64. McKinney, J.D., et al., *Sub-10-dB noise figure in a multiple-GHz analog optical link.* IEEE Photonics Technology Letters, 2007. **19**(5-8): p. 465-467.

65. Williams, K., L. Nichols, and R. Esman, *Externally-modulated 3 GHz fibre optic link utilising high current and balanced detection.* Electronics Letters, 1997. **33**(15): p. 1327-1328.

66. Chiu, Y., et al., *Broad-band electronic linearizer for externally modulated analog fiber-optic links.* IEEE Photonics Technology Letters, 1999. **11**(1): p. 48-50.

67. Huang, M., J. Fu, and S. Pan, *Linearized analog photonic links based on a dual-parallel polarization modulator.* Opt Lett, 2012. **37**(11): p. 1823-5.

68. Niu, J., et al., *Using bidirectional modulation of 2-Ch phase modulator as basis for nonlinear distortion compensation in analog photonic links.* Chinese Optics Letters, 2013. **11**(8): p. 080603.

69. Clark, T.R. and M.L. Dennis, *Coherent optical phase-modulation link.* IEEE Photonics Technology Letters, 2007. **19**(13-16): p. 1206-1208.

70. Xie, X., et al., *Digital joint compensation of IMD3 and XMD in broadband channelized RF photonic link.* Opt Express, 2012. **20**(23): p. 25636-43.

71. Cox III, C., et al. *Broadband, directly modulated analog fiber link with positive intrinsic gain and reduced noise figure*. in *Microwave Photonics, 1998. MWP'98. International Topical Meeting on*. 1998. IEEE.

72. Faugeron, M., et al., *High Optical Power, High Gain and High Dynamic Range Directly Modulated Optical Link.* Journal of Lightwave Technology, 2013. **31**(8): p. 1227-1233.

73. Betts, G.E. and F.J. ODonnell, *Microwave analog optical links using suboctave linearized modulators.* IEEE Photonics Technology Letters, 1996. **8**(9): p. 1273-1275.

74. Dingel, B.B. *Ultra-linear, broadband optical modulator for high performance analog fiber link system*. in *Microwave Photonics, 2004. MWP'04. 2004 IEEE International Topical Meeting on*. 2004. IEEE.

75. Urick, V., et al., *Wideband (0.045–6.25 GHz) 40 km analogue fibre-optic link with ultra-high (> 40 dB) all-photonic gain.* Electronics Letters, 2006. **42**(9): p. 552-553.

76. Cox III, C.H., et al., *Limits on the performance of RF-over-fiber links and their impact on device design.* Microwave Theory and Techniques, IEEE Transactions on, 2006. **54**(2): p. 906-920.

77. Xie, X., et al. *1.8 Watt RF Power and 60% Power Conversion Efficiency Based on Photodiode Flip-chip-bonded on Diamond*. in *CLEO: QELS_Fundamental Science*. 2014. Optical Society of America.

78. Pan, H.P., et al., *Characterization of High-Linearity Modified Uni-Traveling Carrier Photodiodes Using Three-Tone and Bias Modulation Techniques.* Journal of Lightwave Technology, 2010. **28**(9): p. 1316-1322.

79. Beling, A., et al., *Measurement and modeling of a high-linearity modified uni-traveling carrier photodiode.* IEEE Photonics Technology Letters, 2008. **20**(13-16): p. 1219-1221.

80. Agilent, *Agilent fundamentals of RF and microwave noise figure measurements: Application Note 57-1*. 2010, Santa Clara, CA.

81. Beling, A., et al., *Linearity of Modified Uni-Traveling Carrier Photodiodes.* Journal of Lightwave Technology, 2008. **26**(13-16): p. 2373-2378.

82. Seeds, A.J., *Microwave photonics.* IEEE Transactions on Microwave Theory and Techniques, 2002. **50**(3): p. 877-887.

83. Chen, X.F., Z.C. Deng, and J.P. Yao, *Photonic generation of microwave signal using a dual-wavelength single-longitudinal-mode fiber ring laser.* IEEE Transactions on Microwave Theory and Techniques, 2006. **54**(2): p. 804-809.

84. Genest, J., et al., *Microwave signals generated by optical heterodyne between injection-locked semiconductor lasers.* IEEE Journal of Quantum Electronics, 1997. **33**(6): p. 989-998.

85. Goldberg, L., et al., *Microwave Signal Generation with Injection-Locked Laser-Diodes.* Electronics Letters, 1983. **19**(13): p. 491-493.

86. Hyodo, M., et al., *Generation of millimetre-wave radiation using a dual-longitudinal-mode microchip laser.* Electronics Letters, 1996. **32**(17): p. 1589-1591.

87. Simonis, G.J. and K.G. Purchase, *Optical-Generation, Distribution, and Control of Microwaves Using Laser Heterodyne.* IEEE Transactions on Microwave Theory and Techniques, 1990. **38**(5): p. 667-669.

88. O'reilly, J., et al., *Optical generation of very narrow linewidth millimetre wave signals.* Electronics Letters, 1992. **28**(25): p. 2309-2311.

89. Qi, G.H., et al., *Optical generation and distribution of continuously tunable millimeter-wave signals using an optical phase modulator.* Journal of Lightwave Technology, 2005. **23**(9): p. 2687-2695.

90. Dai, Y. and J. Yao, *Microwave pulse phase encoding using a photonic microwave delay-line filter.* Optics Letters, 2007. **32**(24): p. 3486-3488.

91. Chi, H. and J.P. Yao, *An approach to photonic generation of high-frequency phase-coded RF pulses.* IEEE Photonics Technology Letters, 2007. **19**(9-12): p. 768-770.

92. Zhang, Y.M. and S.L. Pan, *Generation of phase-coded microwave signals using a polarization-modulator-based photonic microwave phase shifter.* Optics Letters, 2013. **38**(5): p. 766-768.

93. Ghelfi, P., et al., *Phase Coding of RF Pulses in Photonics-Aided Frequency-Agile Coherent Radar Systems.* IEEE Journal of Quantum Electronics, 2012. **48**(9): p. 1151-1157.

94. Taylor, J., et al., *Characterization of power-to-phase conversion in high-speed PIN photodiodes.* Photonics Journal, IEEE, 2011. **3**(1): p. 140-151.

95. Ito, H., et al., *High-speed and high-output InP-InGaAs unitraveling-carrier photodiodes.* IEEE Journal of Selected Topics in Quantum Electronics, 2004. **10**(4): p. 709-727.

96. Agilent, *Application Note 150-2*. 2012, Santa Clara, CA.

97. Sasahira, K., K. Kuroda, and Y. Yoshikuni, *Pulse amplification characteristics of a CW pumped erbium-doped fiber amplifier*, in *OECC 2010 Technical Digest*. 2010.

98. Xie, X.J., et al., *Improved power conversion efficiency in high-performance photodiodes by flip-chip bonding on diamond.* Optica, 2014. **1**(6): p. 429-435.

99. Liang, D., et al., *Fabrication of Silicon-on-Diamond Substrate and Low-Loss Optical Waveguides.* IEEE Photonics Technology Letters, 2011. **23**(10): p. 657-659.

100. *Data sheet XPDV21s20*. 2012.

101. Chang, C.-M., et al. *Dual-illuminated Parallel-fed Traveling Wave Germanium Photodetectors*. in *Optical Fiber Communication Conference*. 2015. Optical Society of America.

102. Demiguel, S., et al., *Very high-responsivity evanescently coupled photodiodes integrating a short planar multimode waveguide for high-speed applications.* IEEE Photonics Technology Letters, 2003. **15**(12): p. 1761-1763.

103. Demiguel, S., et al., *Analysis of partially depleted absorber waveguide photodiodes.* Journal of Lightwave Technology, 2005. **23**(8): p. 2505-2512.

104. Jiang, H., et al., *The frequency behavior of the third-order intercept point in a waveguide photodiode.* IEEE Photonics Technology Letters, 2000. **12**(5): p. 540-542.

105. Klamkin, J., et al., *Uni-traveling-carrier variable confinement waveguide photodiodes.* Opt Express, 2011. **19**(11): p. 10199-205.

106. Ramaswamy, A., et al., *High Power Silicon-Germanium Photodiodes for Microwave Photonic Applications.* IEEE Transactions on Microwave Theory and Techniques, 2010. **58**(11): p. 3336-3343.

107. Rouvalis, E., et al. *A high-power and high-linearity 50 GHz waveguide photodiode module*. in *Optical Fiber Communications Conference and Exhibition (OFC), 2014*. 2014. IEEE.

108. Rouvalis, E., et al. *A 1× 4 MMI-integrated high-power waveguide photodetector*. in *Indium Phosphide and Related Materials (IPRM), 2013 International Conference on*. 2013. IEEE.

109. Liang, D., et al. *Compact low-threshold hybrid silicon microring resonator lasers*. in *2010 IEEE Photonics Society Winter Topicals Meeting Series (WTM)*. 2010.

110. Sysak, M.N., et al., *Experimental and theoretical thermal analysis of a hybrid silicon evanescent laser.* Optics Express, 2007. **15**(23): p. 15041-15046.

111. Van Campenhout, J., et al., *Electrically pumped InP-based microdisk lasers integrated with a nanophotonic silicon-on-insulator waveguide circuit.* Optics Express, 2007. **15**(11): p. 6744-6749.

112. Jiang, H.F., et al., *Noise Floor Reduction of an Er:Fiber Laser-Based Photonic Microwave Generator.* IEEE Photonics Journal, 2011. **3**(6): p. 1004-1012.

113. *Agilent Technologies Network Analyzer Measurements: Filter and Amplifier Examples.* 1997.

Curriculum Vitae

Xiaojun Xie

Personal

June 24, 1987 Born in Santai, Sichuan Province, Chin

Education

2015 Doctor of Philosophy in Electrical and Computer Engineering, University of Virginia

2013 Master of Science in Electromagnetic Field and Microwave Technology, Beijing University of Posts and Telecommunications

2010 Bachelor of Science in Optical Information Science and Technology, University of Electronic Science and Technology of China

Publications

Conference paper

1. X. Xie, Q. Zhou, E. Norberg, M. Jacob-Mitos, Y. Chen, Z. Yang, A. Ramaswamy,

G. Fish, J. E. Bowers, J. C. Campbell, and A. Beling, " High-power Heterogeneously Integrated Balanced Waveguide-Coupled Photodiodes on Silicon-on-Insulator," IEEE Photonics Conference, paper WA 3.2, 2015.

2. X. Xie, Q. Zhou, E. Norberg, M. Jacob-Mitos, Y. Chen, A. Ramaswamy, G. Fish, J. E Bowers, J. C. Campbell, A. Beling, "Heterogeneously Integrated Silicon Waveguide Coupled Photodiodes with 12 dBm RF Output Power at 40 GHz," Optical Fiber Communication Conference (OFC), Th5B. 7, 2015 (Postdeadline paper).

3. X. Xie, Q. Zhou, K. Li, A. Beling, and J. C. Campbell, "Photonic Generation of High-Power Pulsed Microwave Signals with Peak Powers up to 7.2 Watt, " Optical Fiber Communication Conference (OFC), Tu3F. 2, 2015. (2015 OFC Top Scoring Paper)

4. X. Xie, Q. Zhou, K. Li, A. Beling and J. C. Campbell, "1.8 Watt RF Power and 60% Power Conversion Efficiency Based on Photodiode Flip-chip-bonded on Diamond," in Conference Lasers Electro-Optics (CLEO), paper JTh5B.9.6, 2014. (Postdeadline Paper)

5. X. Xie, K. Li, Qinglong Li, A. Beling, and J. C. Campbell, "Photonic Generation of High-Power Pulsed Microwave Signals with Peak Powers up to 14.2 Watt, " Conference Lasers Electro-Optics (CLEO), STh3F.5, 2015

6. X. Xie, K. Li, Q. Zhou, A. Beling and J. C. Campbell, "High Performance Analog Photonic Link Based on Modified Uni-traveling-carrier Photodiode," in Conference

Lasers Electro-Optics (CLEO), paper STu2G. 6, 2014.

7. X. Xie, R. Wang, Y. Dai, K. Xu, J. Wu, Y. Li and J. Lin, "Coherent photonic RF channelizer by optical frequency combs and I/Q demodulation" in Optical Fiber Communication Conference (OFC), paper OW3I, 2012.

8. X. Xie, Y. Dai, K. Xu, J. Niu, L. Yan, R. Wang, Y. Ji, and J. Lin, "Digital nonlinearities compensation based on forward distortion information acquisition in channelized RF photonic links" in Topical Meeting on Microwave Photonics (MWP), paper 88-91, 2012.

9. Z. Yang, X. Xie, Q. Li, A. Beling and J. C. Campbell, "20 GHz Analog Photonic Link with 16 dB Gain Based on a High-Power Balanced Photodiode," IEEE Photonics Conference, paper WC 3.2, 2015.

10. K. Li, X. Xie, E. Rouvalis, S. Fedderwitz, A. G Steffan, Q. Li, Z. Yang, A. Beling, J. C Campbell, "High-power photodetector modules for microwave photonic applications," SPIE OPTO, 2015.

11. K. Li, X. Xie, Q. Zhou, A. Beling and J. C. Campbell, "High Power 20GHz Photodiodes with Microwave Tuning Circuits," in Conference Lasers Electro-Optics (CLEO), paper STh4I. 6, 2014.

12. Q. Li, K. Li, X. Xie, Z. Yang, A. Beling and J. C. Campbell, "High-power flip-chip bonded photodiodes with 110 GHz bandwidth," IEEE Photonics Conference, paper WA 1.1, 2015.

13. Q. Li, K. Li, X. Xie, Y. Fu, Z. Yang, Y. Shen, Y. Wang, A. Beling and J. C. Campbell, "Development of high-power photodiodes for W-band applications," IEEE Avionics and Vehicle Fiber-Optics and Photonics Conference, paper TuC3, 2015.

14. Joe C. Campbell, A. Beling, X. Xie, Q. Zhou and K. Li, "High-power, high-linearity photodiodes," in Indium Phosphide and Related Materials (IPRM), page 1-2, 2014.

15. A. Beling, J. C. Campbell, K. Li, Q. Li, M. Woodson, X. Xie, and Z. Yang, "High-power photodiodes for analog applications" in Topical Meeting on Microwave Photonics (MWP), paper 88-91, 2014.

Journal paper

16. X. Xie, Q. Zhou, E. Norberg, M. Jacob-Mitos, Y. Chen, Z. Yang, A. Ramaswamy, G. Fish, J. E. Bowers, J. C. Campbell, and A. Beling, " High-power and High-speed Heterogeneously Integrated Waveguide-Coupled Photodiodes on Silicon-on-Insulator," Journal of Lightwave Technology, 2015. (Invited paper)

17. X. Xie, K. Li, Y. Shen, Q. Li, J. Zang, A. Beling, J. C. Campbell, "Photonic Generation of High-Power Pulsed Microwave Signals," Journal of Lightwave Technology, 33(18), 2015. (Invited paper)

18. X. Xie, Q. Zhou, K. Li, Y. Shen, Q. Li, Z. Yang, A. Beling and J. C. Campbell, "High-power high-power-conversion-efficiency modified uni-travelling carrier photodiode flip-chip bonded on diamond submount," Optica, 1(16) 2014.

19. X. Xie, K.. Li, Q. Zhou, A. Beling and J. C. Campbell, "High-Gain, Low-Noise-

Figure and High-Linearity Analog Photonic Link Based on a High-Performance Photodetector," Journal of Lightwave Technology, 32(21), 2014.

20. X. Xie, Y. Dai, K. Xu, J. Niu, L. Yan, R. Wang, Y. Ji, and J. Lin, "Digital joint compensation of IMD3 and XMD in broadband channelized RF photonic link," Optics Express, 20(23), 2012.

21. X. Xie, Y. Dai, K. Xu, J. Niu, R. Wang, L. Yan, and J. Lin, "Broadband photonic RF channelization based on coherent optical frequency combs and I/Q demodulators" Photonics Journal, 4(4), 2012.

22. X. Xie, Y. Dai, Y. Ji, K. Xu, Y. Li, J. Wu, and J. Lin, "Broadband photonic radio-frequency channelization based on a 39-GHz optical frequency comb," Photonic Technology Letter, 24(8), 2012.

23. K. Li, X. Xie, Q. Li, Y. Shen, M. Woodson, Z. Yang, A. Beling and J. C. Campbell, "High-Power Photodiode Integrated with Coplanar Patch Antenna," Photonics Technology Letters, 27(6), 2015

24. K. Li, X. Xie, Q. Zhou, A. Beling and J. C. Campbell, "High Power 20 GHz Photodiodes with Resonant Microwave Circuits," Photonics Technology Letters, 26(13), 2014

25. J. Niu, K. Xu, X. Xie, Y. Dai, J. Li and J. Lin, "Using bidirectional modulation of 2-Ch phase modulator as basis for nonlinear distortion compensation in analog photonic links," Chinese Optics Letters, 11(8), 2013.

26. Y. Dai, K. Xu, X. Xie, L. Yan, R. Wang and J. Lin, "Broadband photonic radio frequency (RF) channelization based on coherent optical frequency combs and polarization I/Q demodulation," Science China Technological Sciences, 56(3), 2013

27. E. Rouvalis, F. Baynes, X. Xie, K. Li, Q. Zhou, F. Quinlan, T. M. Fortier, S. A. Diddams, A. G. Steffan, A. Beling and J. C. Campbell, "High-Power and High-Linearity Photodetector Modules for Microwave Photonic Applications," Journal of Lightwave Technology, 32(20), 2014